

Study on the Magnetic Properties of Stable Organic
Radicals Carrying Hydrazyl and Nitroxide-Based
Spin Centers and the Spin-Spin Interactions
Through Non-Conjugated Framework

February 2018

Yusuke Takahashi

A Thesis for the Degree of Ph.D. in Science

Study on the Magnetic Properties of Stable Organic
Radicals Carrying Hydrazyl and Nitroxide-Based
Spin Centers and the Spin-Spin Interactions
Through Non-Conjugated Framework

February 2018

Graduate School of Science and Technology

Keio University

Yusuke Takahashi

Contents

Chapter 1: General Introduction

1.1. Magnetic Properties of Substances	1
1.1.1. Magnetic Behavior	1
1.1.2. Cooperative Magnetic Behavior in Inorganic Substances	8
1.2. Molecule-Based Magnetism	10
1.2.1. Intramolecular Magnetic Interaction	10
1.2.2. Intermolecular Magnetic Interaction	14
1.3. Physicochemical Properties of Stable Organic Radicals	17
1.3.1. Stability of Organic Radicals	17
1.3.2. Electronic Structure of Organic Radicals	19
1.3.3. Magnetic Properties of Organic Radicals	29
1.3.4. Bistability in Organic Radical Solids	30
1.4. Purpose of Study	31
References in Chapter 1	33

Chapter 2: Substituent Effects on Magnetic Properties of Benzotriazinyl Radicals

2.1. Introduction	35
2.2. Synthesis	41
2.3. Crystallographic Analysis	42
2.4. Magnetic Property	51
2.5. Origin of Magnetic Interaction	55
2.5.1. DFT Calculation	55
2.5.2. Magneto-Structural Correlation Based on Computation	57
2.6. ESR Measurement	62
References in Chapter 2	64

Chapter 3: Magneto-Structural Correlation in Nitroxyl-Triazinyl Hetero Biradicals

3.1. Introduction	67
3.2. Synthesis	71
3.3. Crystallographic Analysis	72
3.4. Magnetic Property	77
3.5. Evaluation of Magnetic Interaction Based on Computation	79
3.6. ESR Measurement	82
References in Chapter 3	84

Chapter 4: Magneto-Structural Correlation in Nitroxyl-Verdazyl/Nitronyl Nitroxide Hetero Biradicals

4.1. Introduction	86
4.2. Synthesis	88
4.3. Crystallographic Analysis	89
4.4. Magnetic Property	94
4.5. Evaluation of Magnetic Interaction Based on Computation	96
4.6. ESR Measurement	102
References in Chapter 4	104

Chapter 5: Computational Study of Magnetic Interaction through Non-Conjugated Framework

5.1. Introduction	105
5.2. Correlation between the Spin Density on Vinyllic Moiety and Magnetic Interaction	105
5.3. Distance Dependency on Pyrroline Ring for Magnetic Interaction	108
5.4. Substituent Effect on Methyl Group	110
5.5. Rotation Effect on Methyl Group	111
5.6. Improved Molecular Design for Ground Triplet Biradical Carrying Non-Conjugated Framework	113
References in Chapter 5	117

Chapter 6: Conclusion and Future Scope

6.1. Conclusion	118
6.2. Future Scope	119

Chapter 7: Details of Synthetic Procedures

7.1. General Information	121
7.2. Synthesis in Chapter 2	122
7.3. Synthesis in Chapter 3	126
7.4. Synthesis in Chapter 4	128

Publication List

Acknowledgement

Chapter 1: General Introduction

1.1. Magnetic Properties of Substances

1.1.1. Magnetic Behavior

The magnetism of substances originates from the magnetic moment of an unpaired electron. The unpaired electron has a specific angular momentum depending on the spin freedom and displays the spin magnetic moment μ_B . The magnetic properties of substances are categorized by their magnetic structure (Figure 1-1).

(a) Paramagnetism

In a paramagnetic substance, their magnetic moments are randomly oriented. Paramagnetism is classified by three types.

(a-1) Langevin Paramagnetism

Langevin paramagnetism is observed in ionic crystals and insulators and their magnetization and magnetic susceptibility exhibit an inverse proportion to the temperature, referred to as the Curie-Weiss law (equation 1-1).

$$\chi_p = \frac{C}{T-\theta} \quad (\text{eq. 1-1})$$

The Weiss temperature θ represents the exchange interaction as the temperature and positive/negative values suggest ferromagnetic/antiferromagnetic interactions between spin centers, respectively (Figure 1-2). The Curie-Weiss law is satisfied in the high temperature range and this theory does not apply when the temperature is close to the absolute value of θ at a low temperature.

(a-2) Pauli Paramagnetism

Pauli paramagnetism is observed in the free electron system of metals. In a magnetic field, the spins derived from electrons are polarized and the number of spins aligning parallel to the applied field are increased, resulting in the occurrence of paramagnetism. Pauli paramagnetism rarely depends on

the temperature. The energies of electrons aligned parallel and antiparallel under an applied field H are expressed as $-\mu_B H$ and $\mu_B H$, respectively. The lower limit of the density of state $D(\varepsilon)$ of spins is changed to $-\mu_B H$ and $\mu_B H$, respectively. The Fermi level of the electrons ε_F is the same, thus the number of housed electrons is changed (parallel electrons: $N/2+n$, antiparallel electrons: $N/2-n$), which induced magnetization $M = 2n\mu_B$, is proportional to the applied field H (Figure 1-3). For the condition of $H \neq 0$ and $T \neq 0$, the magnetization $M(T, H)$ is described by equation 1-2.

$$M(T, H) = 2\mu_B^2 D(\varepsilon_F(0)) \left\{ 1 + \frac{\pi^2}{6} (k_B T)^2 \left[\frac{d^2 \ln D}{d\varepsilon^2} \right]_{\varepsilon_F(0)} \right\} H \quad (\text{eq. 1-2})$$

The magnetic susceptibility of a free electron is described by equation 1-3. The magnetic susceptibility at absolute temperature $\chi(0)$ is almost equal to 10^{-6} emu cm³, which is low compared to that of a magnetic substance of an insulator following the Curie-Weiss law.

$$\chi(T) = \chi(0) \left\{ 1 + \frac{\pi^2}{6} (k_B T)^2 \left[\frac{1}{D} \frac{d^2 D}{d\varepsilon^2} - \left(\frac{1}{D} \frac{dD}{d\varepsilon} \right)^2 \right]_{\varepsilon_F(0)} \right\} \quad (\text{eq. 1-3})$$

$$\chi(0) = 2\mu_B^2 D(\varepsilon_F(0))$$

(a-3) Van Vleck Paramagnetism

Due to the polarization effect, magnetization of the ground state with the total angular momentum J is affected by that of excited state J' ($J' = J+1, J-1$) and the contribution of interfusion is expressed by equation 1-4.

$$\chi_C = N\alpha_J \quad (\text{eq. 1-4})$$

$$\alpha_J = \frac{\mu_B^2}{6(2J+1)} \left[\frac{F(J+1)}{E_{J+1}-E_J} + \frac{F(J)}{E_{J-1}-E_J} \right]$$

$$F(J) = \frac{[(L+S+1)^2 - J^2][J^2 - (S-L)^2]}{J}$$

The magnetic susceptibility χ_C does not depend on the temperature, referred to as the Van Vleck paramagnetism. This paramagnetism appears in the case of $E_{J'} - E_J \sim k_B T$ and is important for the evaluation of rare earth elements as well as actinoids.

(b) Antiferromagnetism

The magnetization of antiferromagnetic substances behaves like paramagnetic substances, however, their magnetic susceptibility has a peak at a given temperature, called the Néel temperature T_N . Below the T_N , the magnetic moments are aligned antiparallel in the substance. Above the T_N , the magnetic susceptibility exhibits the Curie-Weiss type behavior and the Weiss temperature θ is generally a negative value.

(c) Ferromagnetism

The magnetic moments are aligned parallel in a substance and exhibit a spontaneous magnetization below the Curie temperature T_C . Above the T_C , the magnetic susceptibility exhibits the Curie-Weiss type behavior and the Weiss temperature θ is generally a positive value.

(d) Ferrimagnetism

In a ferrimagnetic substance, two kinds of magnetic moments exist and they are aligned antiparallel. In a fashion similar of ferromagnetism, they exhibit a spontaneous magnetization below the T_C . Above the T_C , the magnetic susceptibility exhibits the Curie-Weiss type behavior, however, the Weiss temperature θ is negative due to the antiferromagnetic arrangement of the magnetic moments.

(e) Diamagnetism

Diamagnetic substances do not have a spontaneous magnetization and their magnetization is induced in a magnetic field. The induced magnetization is directed opposite to the applied magnetic field. The magnetic susceptibility is almost constant and irrespective of the temperature.

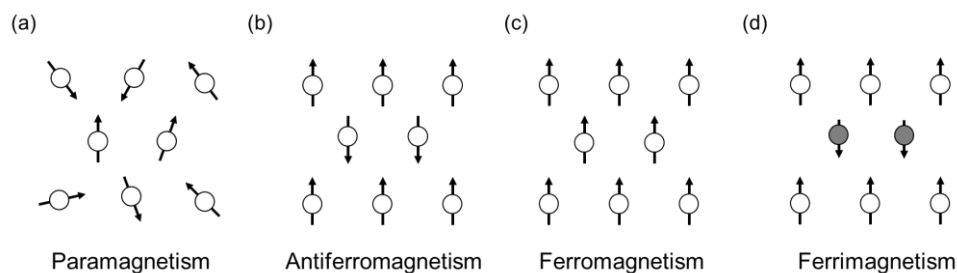


Figure 1-1 Classification of magnetism. (a) Paramagnetism, (b) Antiferromagnetism, (c) Ferromagnetism, (d) Ferrimagnetism.

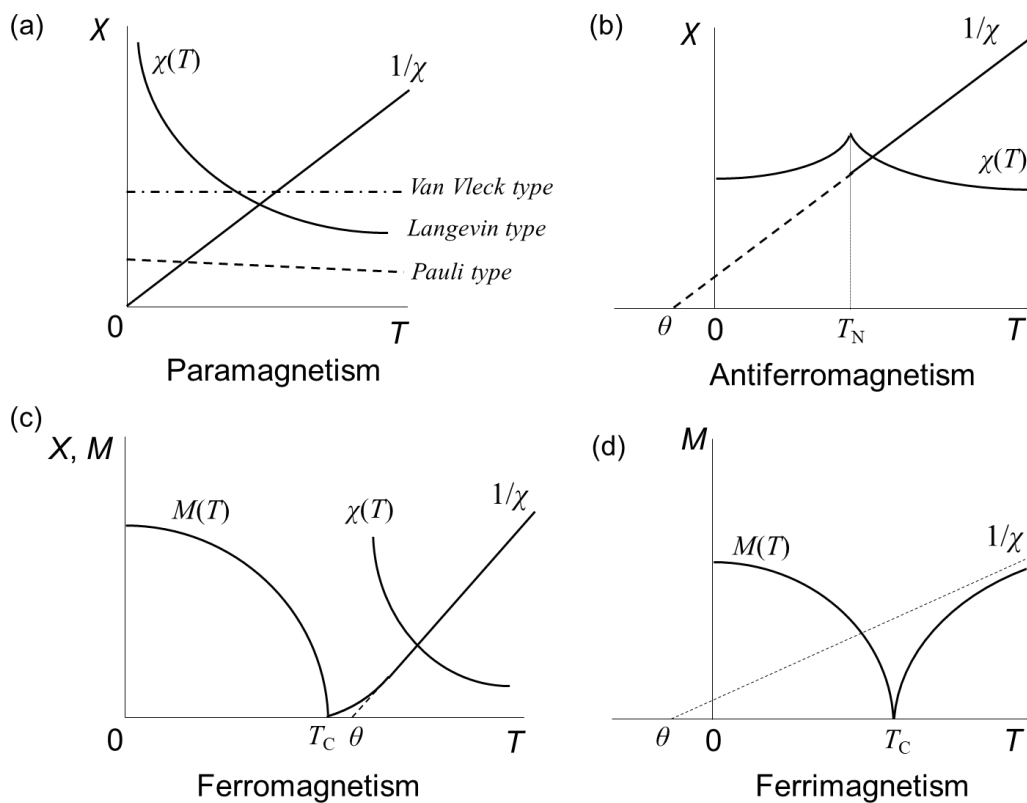


Figure 1-2. Thermal behavior of magnetization and magnetic susceptibility. (a) Paramagnetism, (b) Antiferromagnetism, (c) Ferromagnetism, (d) Ferrimagnetism.

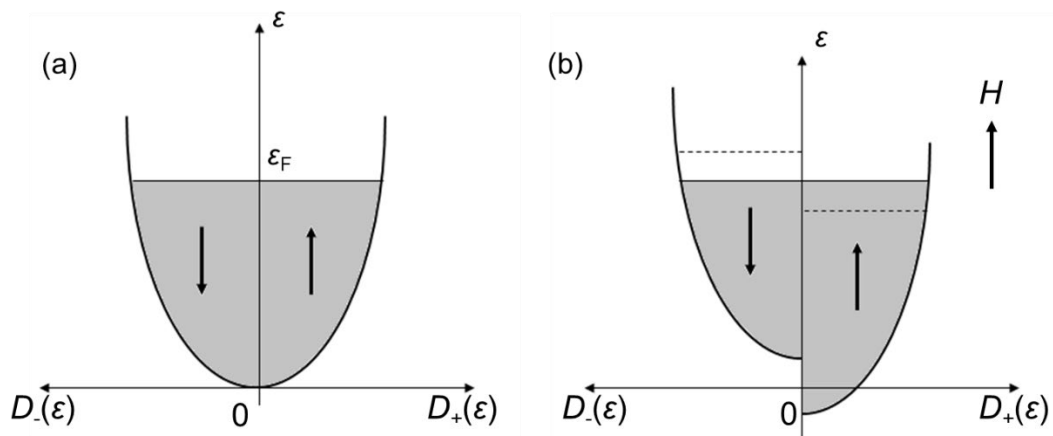


Figure 1-3. Density of state and fermi level of free electron under (a) non-magnetic field and (b) applied magnetic field.

In terms of the magnetization of a substance, the correlation between the magnetization and magnetic field is classified by three behaviors in response to their magnetic property (Figure 1-4).

(a) Linear magnetization curve

The magnetization of paramagnetic and antiferromagnetic substances, which have a positive magnetic susceptibility, exhibits a linear relationship versus the applied magnetic field.

(b) Non-linear magnetization curve

A ferromagnet shows a non-linear magnetization curve with hysteresis. Applying a magnetic field to the degaussing state of a substance, the magnetization curve (1) appears, which is reversible under a weak magnetic field. The magnetization is then saturated under a strong magnetic field and converges to M_s . By lowering the magnetic field, the magnetization follows curve (2), which shows a remnant magnetization M_R and abruptly decreased to zero at the coercive force $-H_C$. A hysteresis curve appears with repeated increasing and decreasing of the temperature.

(c) Metamagnetism

In a metamagnetic substance, the magnetization is abruptly increased in a given magnetic field and saturated. The field dependence of the magnetization is reversible and no remnant magnetization is observed. The derivation of the metamagnetism is mainly related to the antiferromagnetic spin alignment and magnetic anisotropy.

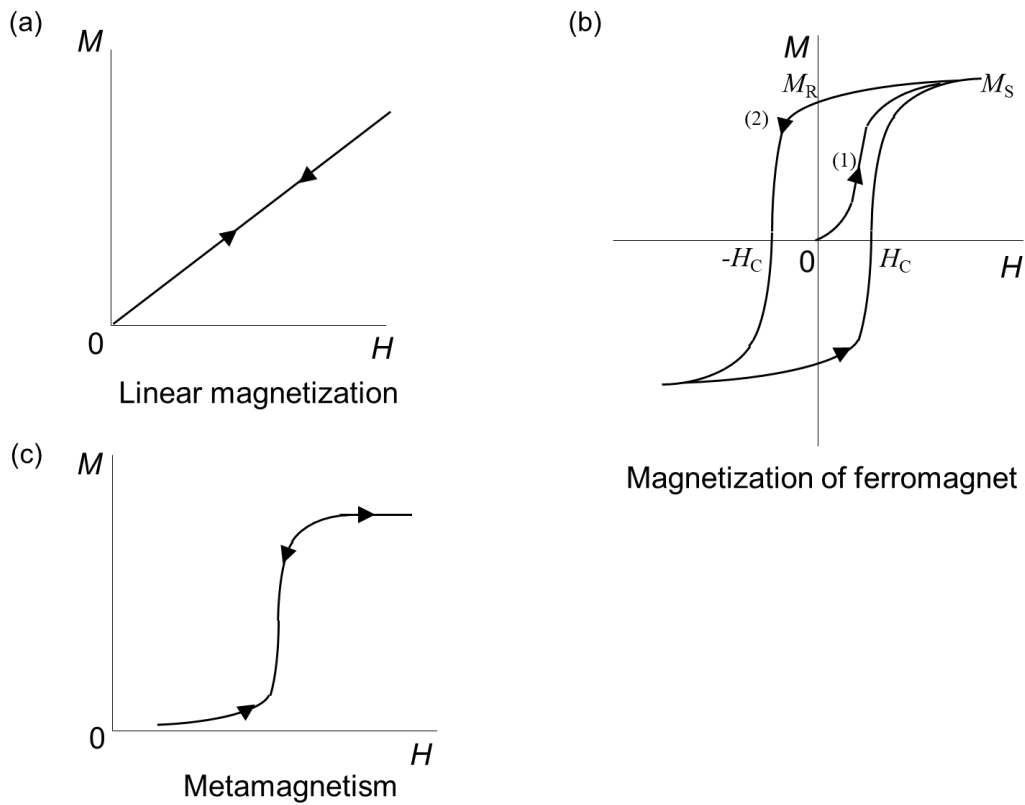


Figure 1-4. Magnetization curve. (a) Linear magnetization, (b) Magnetization behavior of ferromagnet, (c) Metamagnetism.

In the case of aggregate magnetic atoms having the total angular momentum J without a magnetic exchange interaction, each magnetic atom has the $(2J+1)$ degenerated state. Due to the magnetic moment in degenerated orbitals, the Zeeman effect occurs under the applied field H . Taking into account the Boltzmann distribution, the magnetization M arising from N atoms is described by equation 1-5.

$$M = M_S B_J(x) \quad (\text{eq. 1-5})$$

$$M_S = Ng\mu_B J$$

$$B_J(x) = \frac{2J+1}{J} \coth\left(\frac{2J+1}{2J}x\right) - \frac{1}{2J} \coth\left(\frac{1}{2J}x\right)$$

$$x = \frac{gJ\mu_B H}{k_B T}$$

$B_J(x)$, referred to as the Brillouin function, is in the range between zero and one and the value is abruptly saturated with a higher J (Figure 1-5). For organic radicals, carbene and 3d transition metals, the orbital angular momentum L disappeared and J is equal to the spin angular momentum S . Therefore, the S value of molecules can be evaluated by the field dependence of the magnetization.

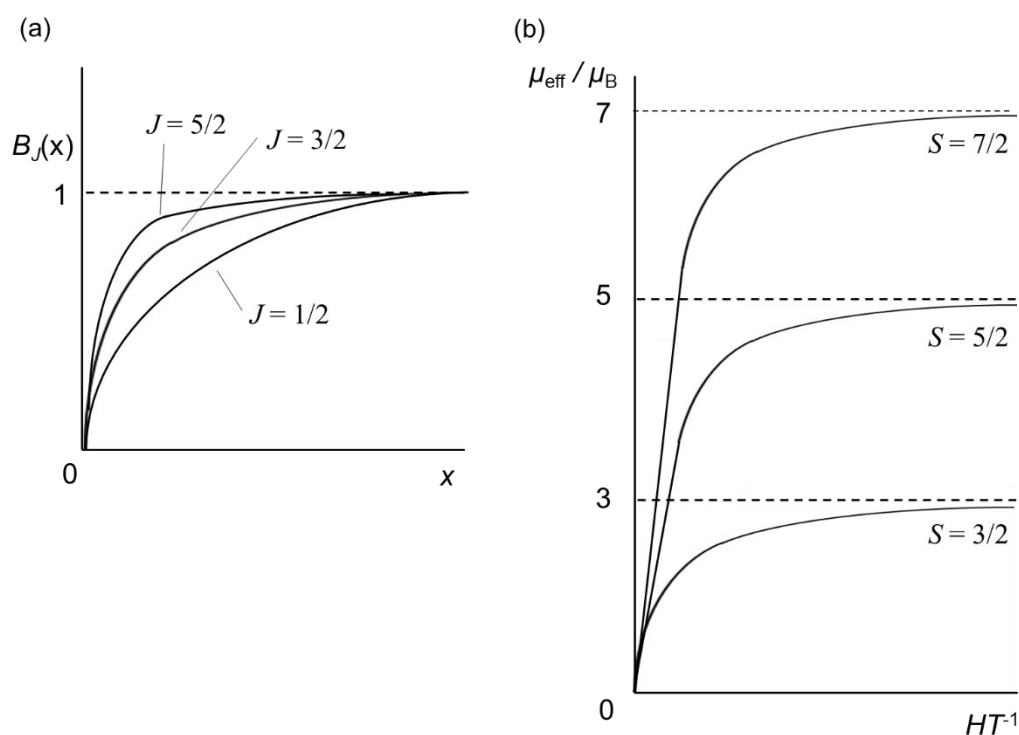


Figure 1-5. (a) Brillouin function. (b) Magnetization curves of spin angular momentum S for organic radicals, carbenes and 3d transition metals.

1.1.2. Cooperative Magnetic Behavior in Inorganic Substances

(a) Stoner Model

In terms of the magnetic interaction between itinerant electrons, their interaction is explained by Hund's rule and the exchange parameter is positive for free electrons. Therefore, the higher occupancy of electrons in the positive spin band affords a higher J value, resulting in metallic ferromagnetism. The magnetic moment of 3d transition metals is not an integer number using the Bohr magneton as the basis unit due to the difference in the occupied density of state between the positive spin band and negative spin band. As shown, the explanation of ferromagnetism for metals using the band structure is referred to as the Stoner model (Figure 1-6).

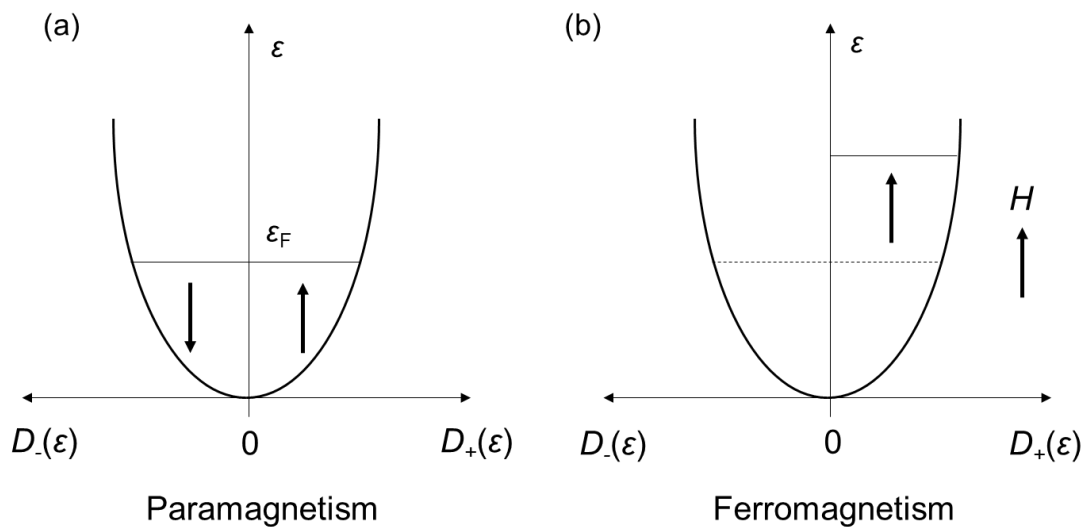


Figure 1-6. Stoner model for itinerant electrons. (a) Paramagnetism, (b) Ferromagnetism.

(b) Superexchange interaction

In a metal oxide, the 3d electrons of transition metals interact via the non-magnetic anion, which is called the superexchange interaction. The magnetic property arising from the superexchange interaction is determined by the orthogonality between the 3d orbital occupied by an unpaired electron and p orbital of the non-magnetic anion. For example, there is an antiferromagnetic interaction in the

linear arrangement of two magnetic atoms having an electron spin in the d_{xy} orbital and anion (Figure 1-7).

- (1) In the case of a positive spin in the d_{xy} orbital of magnetic atom A, the electron with a positive spin in the p_x orbital of anion X is transferred to the unoccupied $d_{x^2-y^2}$ orbital on atom A. The valence of atom A and anion X is reduced.
- (2) Because of the orthogonality between the p_x orbital of anion X and d_{xy} orbital of magnetic atom B, there is a ferromagnetic coupling between atom B and anion X. Therefore, the negative electron spin on the d_{xy} orbital of magnetic atom B is preferred.
- (3) The electron in the $d_{x^2-y^2}$ orbital is back to the p_x orbital of anion X. Due to the behavior of an electron, a magnetic coupling between magnetic atoms A and B is induced. In this case, the electron spins of the magnetic atoms are aligned antiparallel, resulting in an antiferromagnetic interaction.

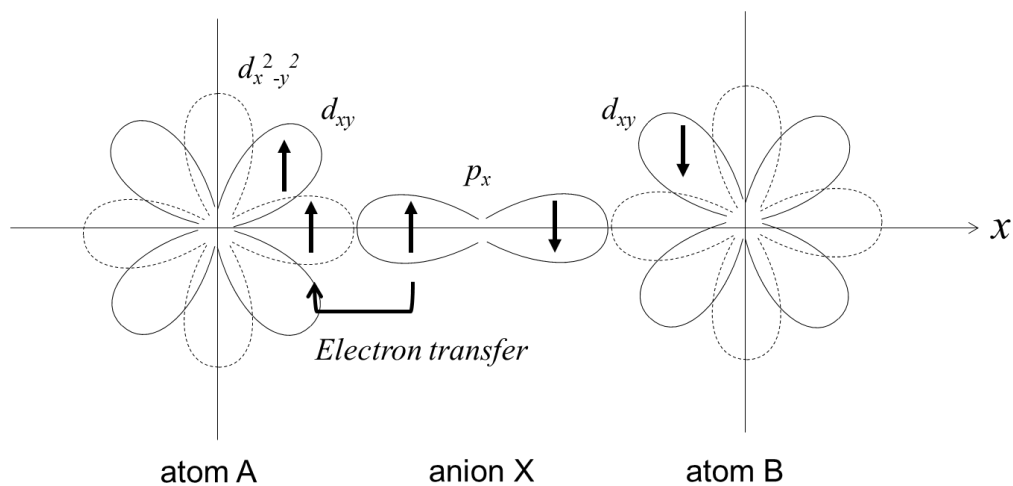


Figure 1-7. Schematic illustration of superexchange interaction.

1.2. Molecule-Based Magnetism

1.2.1. Intramolecular Magnetic Interaction

In the twentieth century, several molecular designs of parallel spin alignments for alternant hydrocarbons with a π -conjugation system have been developed. The alternant hydrocarbon is defined below; in the case of every other carbon atom marked by a star, the marked carbon atoms are not bonded to each other. For example, benzene, trimethylenemethane (**TMM**), tetramethylene ethane (**TME**), pentamethylenepropane (**PMP**) (Figure 1-8) and trityl radical are classified as alternant hydrocarbons, however, molecules with an odd-number ring, such as azulene, are classified as non-alternant hydrocarbons.

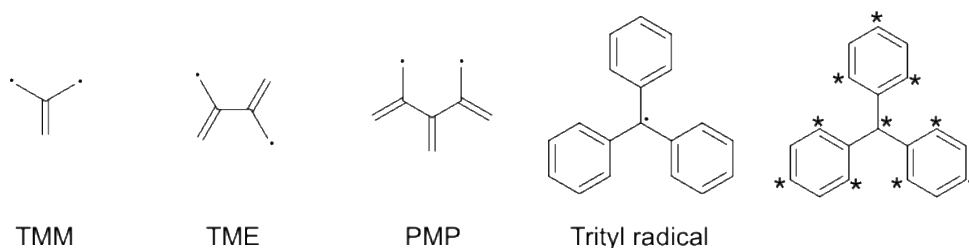


Figure 1-8. Molecular structure of alternant hydrocarbons.

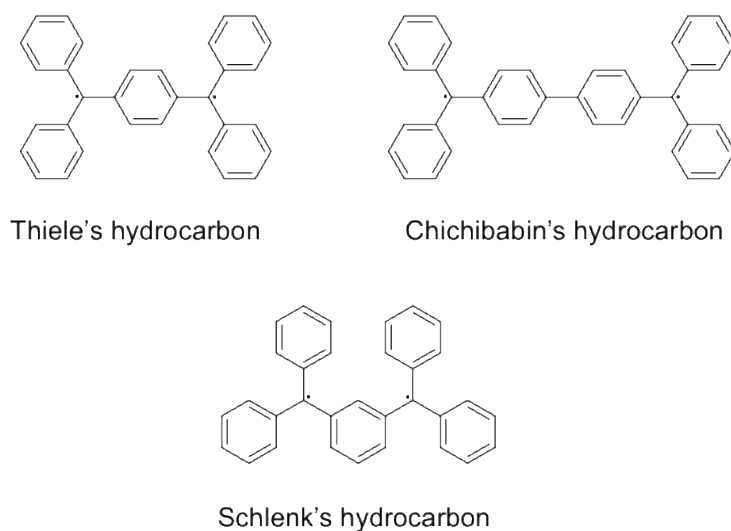


Figure 1-9. Molecular structure of trityl radical-based biradicals.

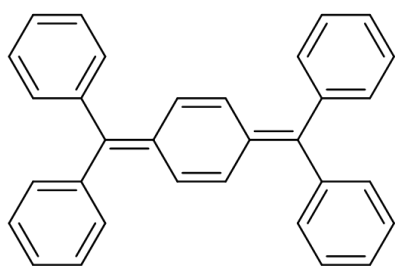
After the discovery of the first organic radical, Gomberg's radical (trityl radical), their biradical analogues were synthesized (Figure 1-9). The *para*-connected biradical (Thiele's hydrocarbon) exhibits an intramolecular antiferromagnetic interaction, whereas a ferromagnetic interaction occurs in Schlenk's hydrocarbon, which is the meta-connection of the trityl radical. Their magnetic interactions are explained by several spin alignment theories.

Longuet-Higgins proposed the molecular orbitals of alternant hydrocarbons in terms of π -topology.⁴ He predicted the number of NBMOs by equation 1-6 and predicted that the NBMOs will be degenerated. According to Longuet-Higgins' theory, the number of NBMOs is zero for Thiele's hydrocarbon, which suggests a ground singlet state. On the other hand, two NBMOs are predicted for Schlenk's hydrocarbon, which means that Schlenk's hydrocarbon has a ground triplet state (Figure 1-10).

$$(\text{The number of NBMOs}) = N - 2T \quad (\text{eq. 1-6})$$

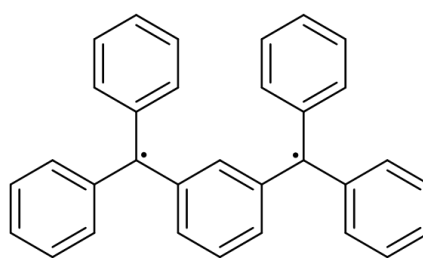
N : the number of C atoms

T : the maximum number of double bonds occurring in any resonance structure



The number of NBMOs

$$N - 2T = 32 - 2 \times 16 = 0$$



$$N - 2T = 32 - 2 \times 15 = 2$$

Figure 1-10. Prediction of the number of NBMOs using Longuet-Higgins' theory.

In 1978, Ovchinnikov suggested that the total spin of alternant hydrocarbons can be described by equation 1-7, where n^* is the number of C^* atoms and n is the number of non-labeled C atoms (Figure 1-11).⁵ The total spins of Thiele's hydrocarbon and Schlenk's hydrocarbon are $S = 0$ and 1, respectively.

$$S = \frac{|n^* - n|}{2} \quad (\text{eq. 1-7})$$

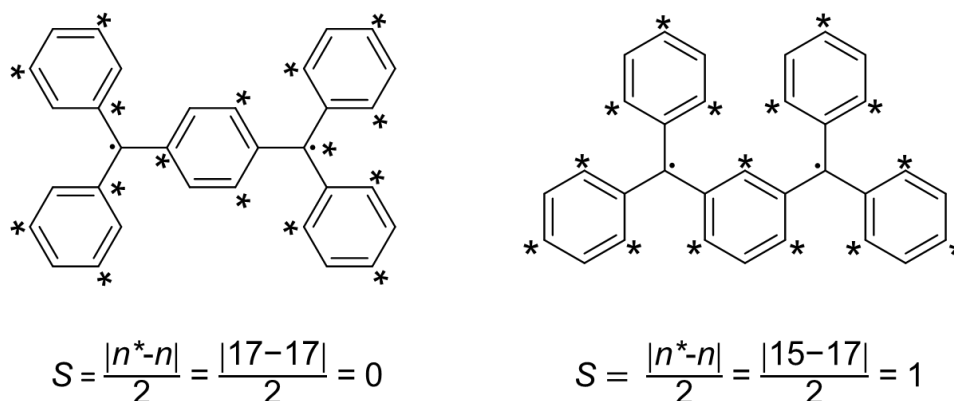


Figure 1-11. Prediction of total spin S using Ovchinnikov's theory.

Regarding the NBMOs of non-Kekulé molecules, Borden and Davidson reported two types of biradicals categorized by the distribution of the NBMOs.⁶ Each NBMO of the non-disjoint type is overlapped on the π -coupler, whereas no overlap occurs in disjoint biradicals. When the NBMOs are degenerated, disjoint type biradicals can have a triplet or singlet ground state and a weak magnetic interaction is observed. On the other hand, non-disjoint type biradicals exhibit a ground triplet state because of a lower electron repulsion than that of the singlet state (Figure 1-12). Schlenk's hydrocarbon is one of the non-Kekulé molecules and the coupler moiety is composed of *meta*-quinodimethane, which is a non-disjoint type biradical.

On the other hand, *para*-quinodimethane derivatives, such as Thiele's hydrocarbon and Chichibabin's hydrocarbon, are some of the Kekulé type molecules and they have a small HOMO-

LUMO energy gap. Therefore, these compounds are highly reactive, however, they have a biradical character because an open-shell singlet structure appears in resonance structure. The contribution of the biradical character can be predicted by the number of aromatic rings in the biradical form. From this point of view, Chichibabin's hydrocarbon has a greater biradical character than Thiele's hydrocarbon.

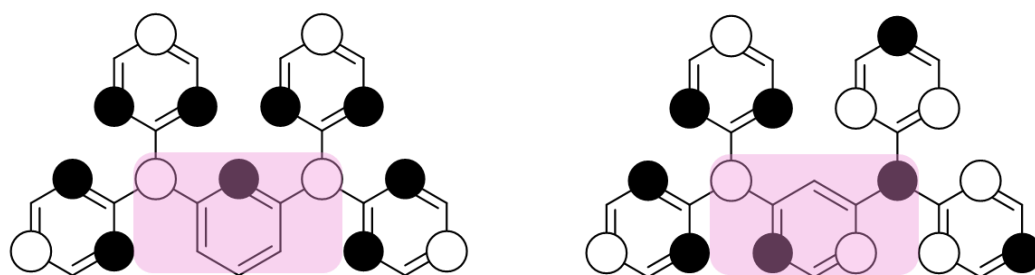


Figure 1-12. NBMOs of Schlenk's hydrocarbon, which has *meta*-quinodimethane as a π -coupler.

1.2.2. Intermolecular Magnetic Interaction

In 1963, McConnell reported the mechanism of intermolecular magnetic exchange between two aromatic radicals based on the spin polarization.⁷ His theory was expanded to the contact of the NBMO by Hoffmann *et al.* in 1995.⁸ McConnell suggested that the magnitude of the magnetic exchange could be described by the Heisenberg-type Hamiltonian (equation 1-8).

$$\mathcal{H} = -\sum_{i,j} J_{ij}^{AB} S_i^A \cdot S_j^B = -S^A S^B \sum_{i,j} J_{ij}^{AB} \rho_i^A \rho_j^B \quad (\text{eq. 1-8})$$

J_{ij} : exchange integral between atom i of molecule A and atom j of molecule B

S_i^A : electron spin density on atom i of molecule A

S^A : total spin operator for molecule A

ρ_i^A : spin density on atom i of molecule A

The exchange integral J_{ij} is usually negative, thus the magnetic interaction will be ferromagnetic when $\rho_i^A \rho_j^B$ is negative. It means that there is alternating positive-negative spin density distributions between the radicals leading to the intermolecular ferromagnetic interaction. In addition, Hoffmann *et al.* focused on the overlap of the SOMO and they predicted that the J value is mainly controlled by their overlap integral. If there is a large overlap of the SOMOs, the antiferromagnetic interaction will be dominant. Therefore, an effective ferromagnetic interaction is achieved when the contact of two SOMOs are orthogonal as much as possible to reduce overlap integral. The unpaired electron of many organic radicals is on the 2p orbital, which suggests that the geometry of the molecular arrangement will determine their magnetic property.

For example, the correlation between the molecular contact and magnetic property of two allyl radicals is considered. Regarding the spin density distribution, in contact(a), the positive spins of the molecules have interacted ($\rho_i^A \rho_j^B > 0$) and an antiferromagnetic interaction is observed. In contrast, the positive spin facing another radical's negative spin in contact (b) and $\rho_i^A \rho_j^B$ should be negative, leading to the ferromagnetic interaction (Figure 1-13). In contact (a), two SOMOs have interacted,

leading to a large overlap integral, and the φ_+ and φ_- orbitals are stabilized and destabilized, respectively. Two unpaired electrons are contained in the φ_+ orbital and the singlet ground state is favored. On the other hand, in contact (b), the overlap integral is cancelled and the φ_+ and φ_- orbitals are degenerated, resulting in the triplet ground state being favored following Hund's rule (Figure 1-14).

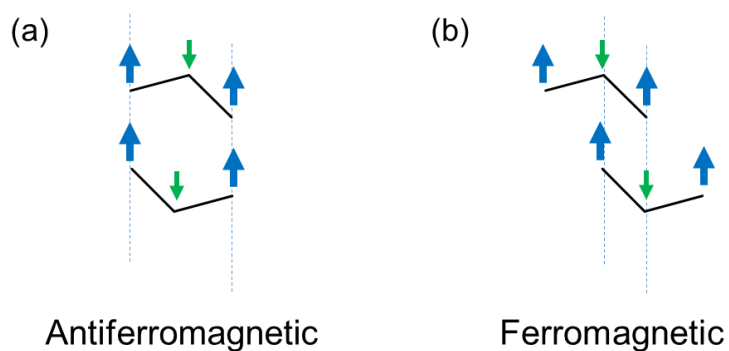


Figure 1-13. Spin alignment of allyl radical and their intermolecular magnetic interaction.

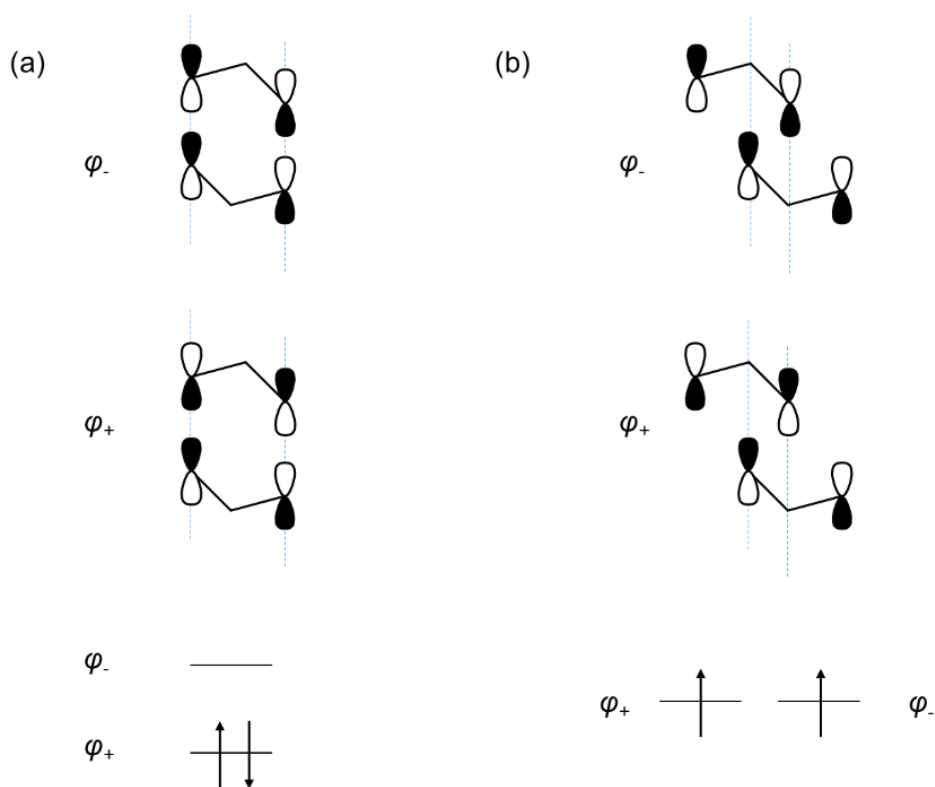


Figure 1-14. Interaction of SOMOs between two allyl radicals.

McConnell also suggested a ferromagnetic spin alignment model for ionic charge-transfer complexes.⁹ Based on his theory, if an ionic charge-transfer pair (D^+A^-) is formed with a back charge-transfer excitation to a triplet state instead of a singlet state (Figure 1-15). For example, decamethylferrocenium tetracyanoethenide ($DMFc^+TCNE^-$) exhibits a ferromagnetic behavior, which was reported by Miller *et al.*¹⁰ The DMFc complexes have the $\cdots D^+A^-D^+A^- \cdots$ motif and the electron spin density in the cation's ring and CN groups of the anion are positive. According to the McConnell theory, there is a negative spin density on the methyl groups. Due to the contribution of the negative spin on the methyl group, an alternating pattern of positive and negative spins appeared in the 1D molecular arrangement¹¹ (Figure 1-16).

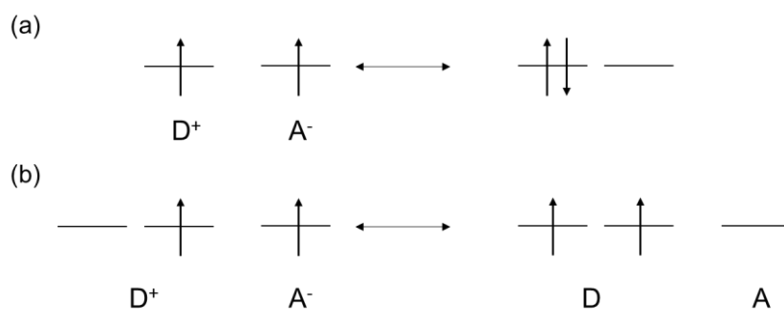


Figure 1-15. Charge-transfer mixing of (a) ionic charge-transfer complex and (b) McConnell's charge-transfer ferromagnet.

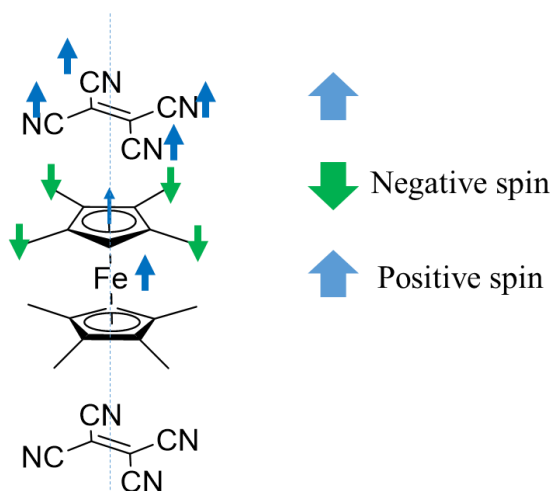


Figure 1-16. Molecular arrangement of $DMFc^+TCNE^-$ salt and its spin alignment.

1.3. Physicochemical Properties of Stable Organic Radicals

1.3.1. Stability of Organic Radicals

Organic radicals, which have an unpaired electron in their structure, have potential applications in many fields as materials for a molecule-based conductor,¹² spin probe in a biological study¹³ and molecule-based magnet.¹⁴ The presence of an unpaired electron exhibits unique optical, conductive and magnetic properties and several properties can be combined by controlling their spin state. However, generally, organic radicals are unstable and show a high reactivity. Thus, to avoid any undesired reaction and disproportionation, stabilization of the organic radicals is required. Typically, two kinds of stabilization methods for increasing the Gibbs free energy of activation ΔG^\ddagger are applied as shown in Figure 1-17.

(1) Kinetically stabilization by introducing a functional group

The kinetical stability is mainly attributed to the steric effect of a substituent. When the reactive site of a molecule is capped by a bulky substituent, the reactivity will be decreased and radicals can maintain their unpaired electron, reflecting the increased energy level of the transition state.

(2) Resonance stabilization

When a reaction occurs, there is large electron density at the reactive site. In this method, the unpaired electron is delocalized to the aromatic ring to decrease the electron density at the reaction point. It affects the decrease in the energy level of organic radicals.

For instance, the stability of the perchlorotriphenylmethyl (**PTM**) radical is explained below. Three phenyl rings are twisted due to the steric effect of the chlorine atoms, resulting in localization of the unpaired electron on the methyl carbon. The unpaired electron slightly delocalizes on the phenyl groups by resonance and their reactivity is reduced by the substituent (Figure 1-18). Thus, the contributions of (1) and (2) stabilize the organic radicals.

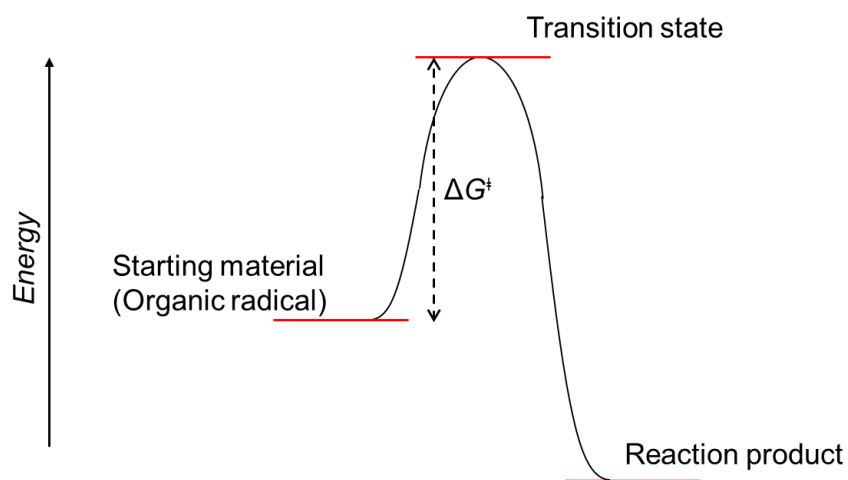


Figure 1-17. Energy level diagram of decomposition reaction.

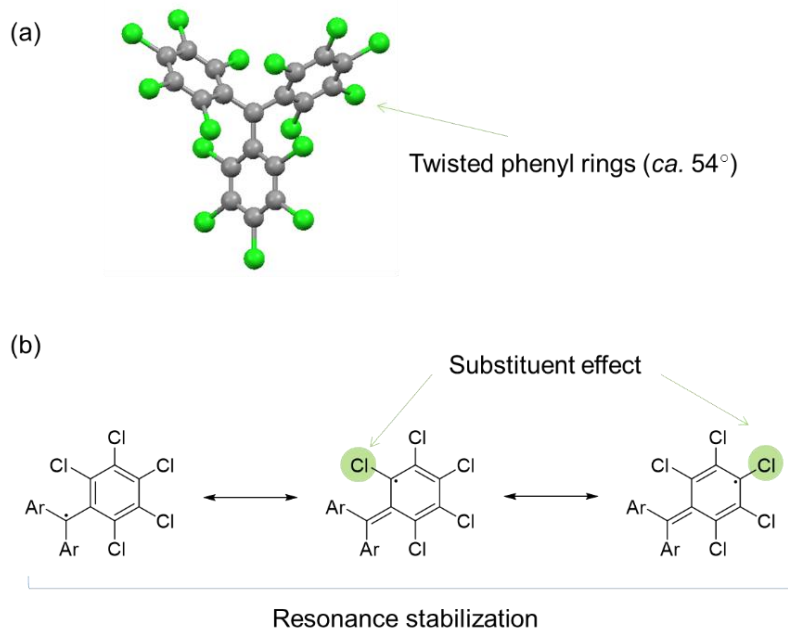


Figure 1-18. (a) Crystallographic structure¹⁵ and (b) resonance structure of **PTM**.

1.3.2. Electronic Structure of Organic Radicals

(a) Classification of Organic Radicals

Organic radicals are categorized into three types in terms of their SOMO and spin density distribution (Figure 1-19). In type (a), the SOMO and spin density are localized on the molecule such as aliphatic nitroxides represented by TEMPO. In type (b), the SOMO is localized on the spin site, however, the spin density delocalizes to the attached π -conjugation system. For example, the SOMO of nitronyl nitroxide radicals and verdazyl radicals is not delocalized to the π -conjugation system due to the existence of a node. In spite of the SOMO localization, the spin density distributes on the π -conjugation system due to the spin polarization effect. In type (c), the SOMO and spin density are delocalized over the molecules such as the benzotriazinyl radicals and trityl radicals. In the field of molecule-based magnetism, organic radicals belonging to types (b) and (c) have been mainly highlighted because the interaction of the spin or SOMO is required to exhibit the intra- and intermolecular magnetic interactions.

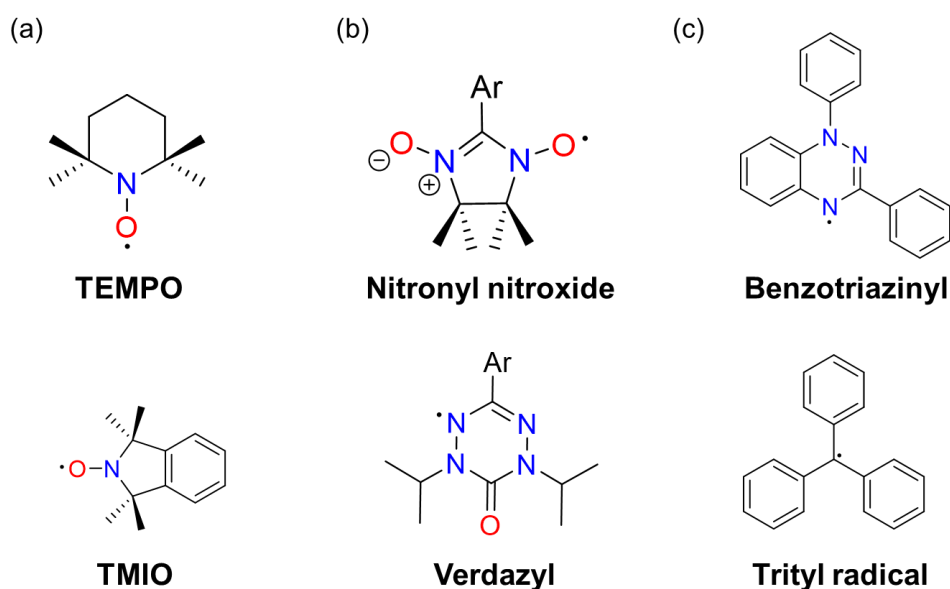


Figure 1-19. Classification of organic radicals

(b) ESR Spectroscopy¹⁶

ESR spectroscopy is one of the best tools to evaluate the existence and distribution of unpaired electrons. The principle of ESR is described below. Considering organic radicals, their unpaired electrons generate small magnetic moments and their magnetic moments are randomly aligned in the case of a negligible interaction between the moments. In the magnetic field H , the magnetic moment of the electrons is directed parallel or antiparallel to the magnetic field. The energy electrons aligned parallel is $E_1 = -\beta H$, whereas that of electrons aligned antiparallel is $E_2 = \beta H$. When microwaves, which have a frequency satisfied by equation 1-9, pass the electrons, the electrons aligned parallel absorb the energy and change to the opposite direction. In contrast, the electrons aligned antiparallel releases the energy and also changes in the opposite direction (Figure 1-20). This phenomenon is similar to the resonance of a sonic wave in terms of the occurrence of an energy exchange by microwave irradiation with a specified frequency. In fact, the magnetic moment arising from the orbital motion of an electron and nucleus affect the $E_2 - E_1$ value and the difference in the energy level is slightly changed from $2\beta H$. Therefore, equation 1-9 is rewritten as equation 1-10. The g -factor depends on the liquid, solid, powder or single crystal.

$$E_2 - E_1 = 2\beta H = h\nu \quad (\text{eq. 1-9})$$

$$g\beta H = h\nu \quad (\text{eq. 1-10})$$

In general, the ESR spectra exhibit a hyperfine structure because of the magnetic interaction between the unpaired electron and nuclei containing a magnetic moment. The line width of the hyperfine structure is called the hyperfine coupling constant (hfcc) a . The number of splitting lines is predicted by equation $2I+1$, where I is the nuclear spin quantum number because the quantum state of the nuclear spin I can be split into $2I+1$ number of m_I components. For example, the ESR spectrum of the hydrogen atom ($S = 1/2, I = 1/2$) exhibits two lines attributed to $\Delta m_s = \pm 1$ transition and a_H of the

hydrogen atom is 508 G (Figure 1-21). The sign of hfc is not determined by the ESR spectra because if the sign of hfc is changed from positive to negative, the replacement of the right and left lines in Figure 1-21 (c) only occurs.

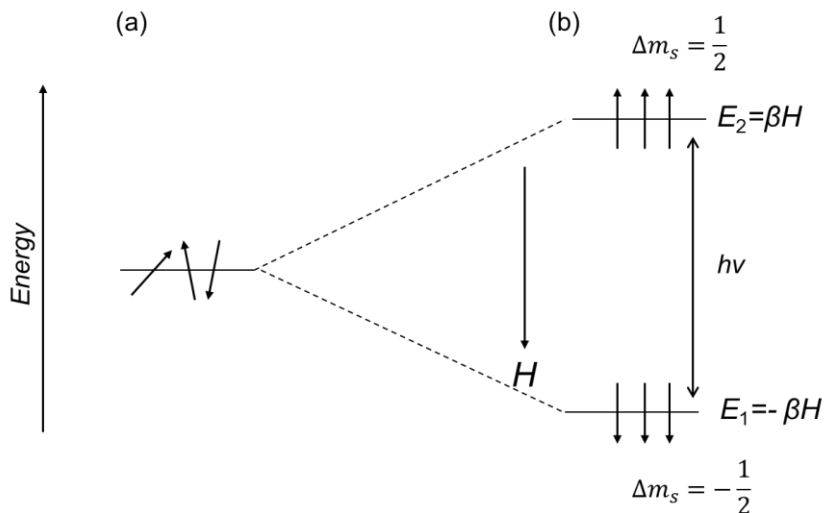


Figure 1-20. Principle of Zeeman effect. (a) under non-magnetic field. (b) under magnetic field.

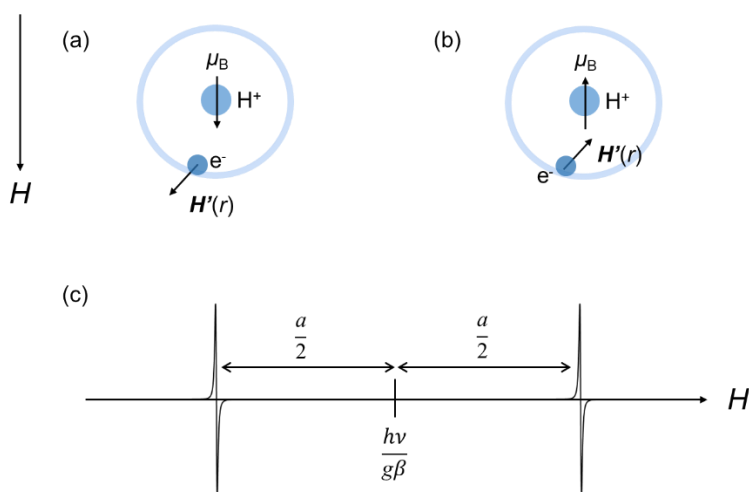


Figure 1-21. The direction of magnetic field for electron on hydrogen atom; (a) the direction of magnetic moment for hydrogen nucleus parallel to external magnetic field. (b) the direction of magnetic moment for hydrogen nucleus antiparallel to external magnetic field. (c) Observed ESR spectrum.

Regarding two equivalent $I = 1/2$ nuclei with $S = 1/2$, such as two equivalent hydrogen nuclei, the spectrum exhibits three lines with the 1:2:1 intensity ratio. Considering the component of m_l , that

of $m_I = 0$ is doubly degenerated because the nuclear spin state can be described in the ($\uparrow\downarrow$) and ($\downarrow\uparrow$) states (Figure 1-22). Therefore, for the transition intensity of $\Delta m_s = \pm 1$, $\Delta m_I = 0$ is twice that of the other transition intensity and the 1:2:1 intensity ratio appeared. When the nuclei are non-equivalent, the spectrum pattern is changed. For example, considering the pair of two equivalent hydrogen nuclei H_1 and one hydrogen nucleus H_2 , whose hfccs are described as a_1 and a_2 . The spectrum pattern depends on the ratio of a_1 and a_2 (Figure 1-23). In the case of $a_1 > a_2$, the spectrum exhibits the 1:1:2:2:1:1 pattern. In the case of $a_1 = a_2$, these hydrogen nuclei are equivalent and the spectrum exhibits the 1:3:3:1 pattern. In the case of $a_1 < a_2$, the spectrum exhibits the 1:2:1:1:2:1 pattern. Regarding $2a_1 = a_2$, some split lines are overlapped and the spectrum exhibits the 1:2:2:2:1 pattern.

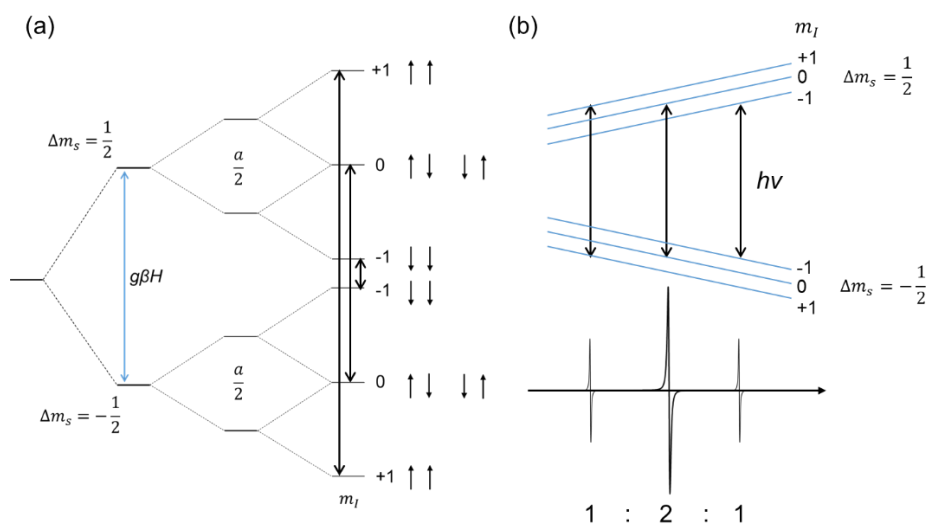


Figure 1-22. (a) Prediction and (b) observed ESR spectrum of $S = 1/2$ system for two equivalent $I = 1/2$ nuclei.

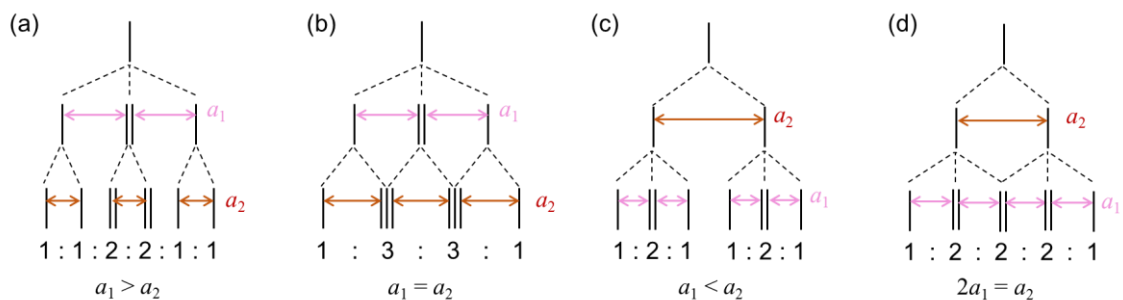


Figure 1-23. The ESR spectra of $S = 1/2$ system for the pair of two equivalent hydrogen nuclei H_1 and one hydrogen nucleus H_2 . (a) $a_1 > a_2$, (b) $a_1 = a_2$, (c) $a_1 < a_2$, (d) $2a_1 = a_2$.

The hfccs are proportional to the density of the unpaired electron and determined by equation 1-11 reported by McConnell. Therefore, the spin density distribution will be estimated in the case of observing the hyperfine structure.

$$a = Q\rho \quad (\text{eq. 1-11})$$

Q : proportional constant

ρ : density of unpaired electron

Considering a biradical, there are two unpaired electrons, and the triplet state of its ESR spectrum will exhibit two lines of fine structure and the line width d is described by equation 1-12.

$$d = \frac{3}{2}g\beta \int \frac{(3\cos^2\theta - 1)}{r^3} \rho(\mathbf{r}) dv \quad (\text{eq. 1-12})$$

In the case of r belonging to the Cartesian coordinate as the main axes and l, m, n as the direction cosine, the line width is described by equation 1-13. According to equation 1-14, D_{xx}, D_{yy} and D_{zz} will be expressed in equation 1-15. In general, the x, y and z axes are set as the higher D value and lower E value (the spectrum is shown in Figure 1-24). The estimated D and E values are used for structure determination of a radical pair.

$$\begin{aligned} d &= \frac{3}{2}g\beta \int \left[3 \left(\frac{x}{r}l + \frac{y}{r}m + \frac{z}{r}n \right)^2 - 1 \right] \frac{1}{r^3} \rho(\mathbf{r}) dv \\ &= \frac{3}{2}g\beta \int \left(\frac{3x^2 - r^2}{r^2} l^2 + \frac{3y^2 - r^2}{r^2} m^2 + \frac{3z^2 - r^2}{r^2} n^2 \right) \frac{1}{r^3} \rho(\mathbf{r}) dv \\ &= D_{xx}l^2 + D_{yy}m^2 + D_{zz}n^2 \end{aligned} \quad (\text{eq. 1-13})$$

$$\text{where} \quad D_{xx} = \frac{3}{2}g\beta \int \frac{3x^2 - r^2}{r^5} \rho(\mathbf{r}) dv$$

$$D_{yy} = \frac{3}{2}g\beta \int \frac{3y^2 - r^2}{r^5} \rho(\mathbf{r}) dv$$

$$D_{zz} = \frac{3}{2}g\beta \int \frac{3z^2 - r^2}{r^5} \rho(\mathbf{r}) dv$$

$$D_{xx} + D_{yy} + D_{zz} = 0 \quad (\text{eq. 1-14})$$

$$\begin{cases} D_{zz} = 2D \\ D_{xx} = -D-3E \\ D_{yy} = -D+3E \end{cases} \quad (\text{eq. 1-15})$$

In terms of the point-dipole approximation, the distance between the unpaired electrons is determined by equation 1-16, resulting in determination of the distance between the unpaired electrons. In a solution, due to the rapid rotation of the molecule, the averaged spectrum is observed. In this case, d is averaged to zero and the fine structure cannot be observed. Therefore, a sample of a frozen solution is often used to obtain the fine structure.

$$|D| = \left| \frac{-3g\mu_B}{2r^3} \right| \quad (\text{eq. 1-16})$$

In addition, triplet state molecules exhibit spectra corresponding to the $g = 4$. The flipping energy of the magnetic moment for an unpaired electron in a magnetic field H is $|2\beta H|$. Normally, one of the unpaired electrons changes its direction, however, when a strong magnetic interaction between unpaired electrons exists, both of the unpaired electrons change their direction at once, which corresponds to the $g = 4$ signal (Figure 1-25(a)). According to equation 1-10, $h\nu$ is a fixed value, therefore, the $g = 4$ signal is observed on the half field (H_1 in Figure 1-25(b)) of $g = 2(H_2$ in Figure 1-25(b)). The observation of the $g = 4$ signal is conclusive proof of the triplet state existence.

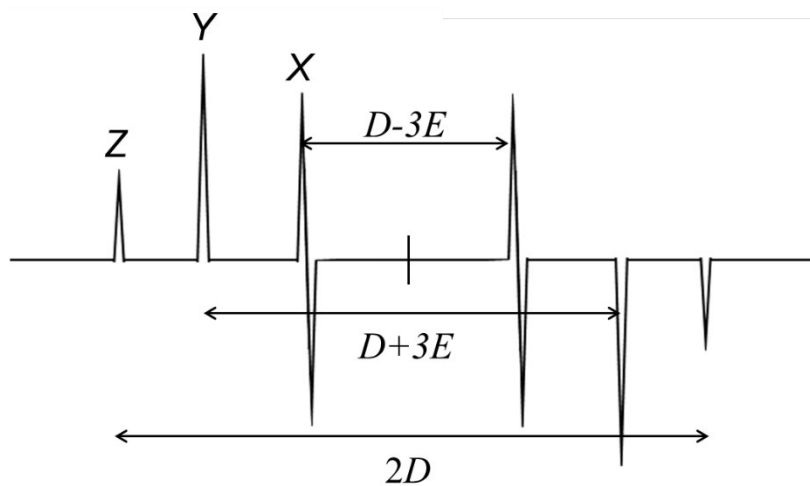


Figure 1-24. ESR spectrum of triplet biradical in glass matrix.

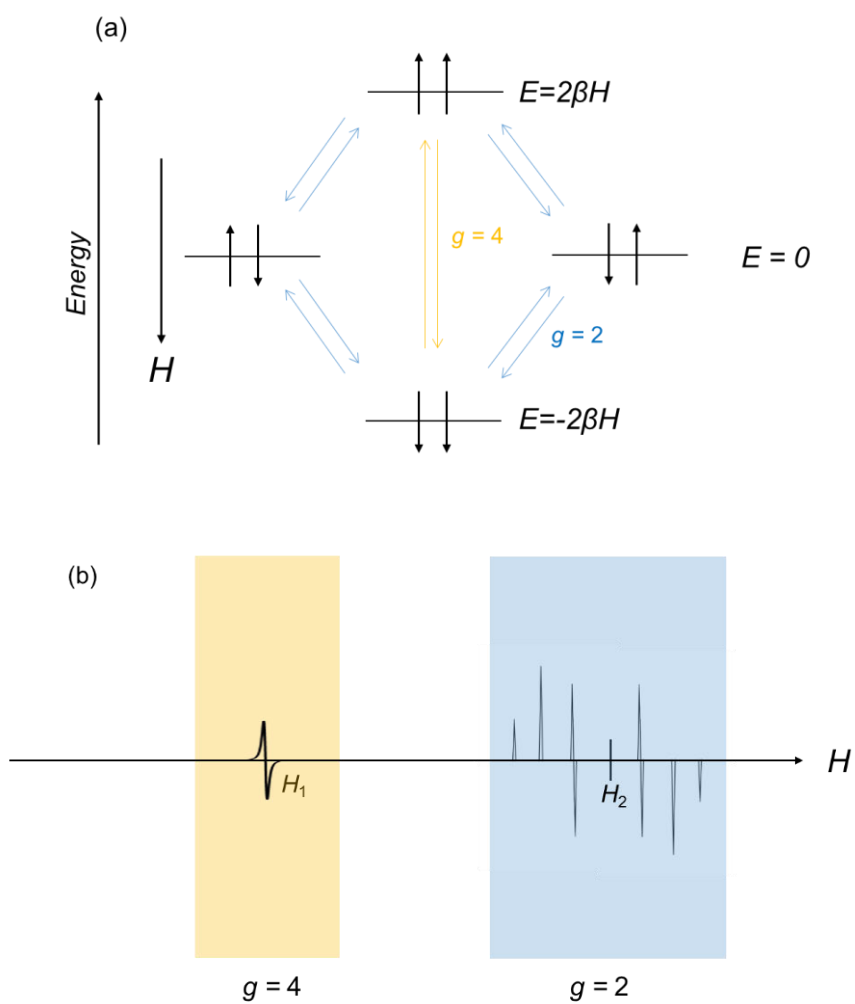


Figure 1-25. (a) The energy diagram of unpaired electrons in triplet molecule. (b) The typical spectrum of triplet biradical with a large magnetic coupling.

(c) Intramolecular Magnetic Interaction Derived from Spin Polarization

Regarding biradicals using the type (b) radical, such as the nitronyl nitroxide, the spin centers are connected by the π -conjugation system. In this case, a magnetic interaction can be observed due to the spin polarization effect in spite of the non-distribution of SOMOs on the π -conjugation system. Their magnetic property can be determined by the spin alignment. For example, the *meta*-phenylene coupled nitronyl nitroxide biradical exhibits a ferromagnetic interaction because of parallel spin alignment on the nitronyl nitroxide sites, whereas there is antiferromagnetic interaction in the *ortho*- and *para*-phenylene coupled biradicals. In addition, an intramolecular antiferromagnetic interaction is observed in the olefin bridged nitronyl nitroxide biradical¹⁷ (Figure 1-26).

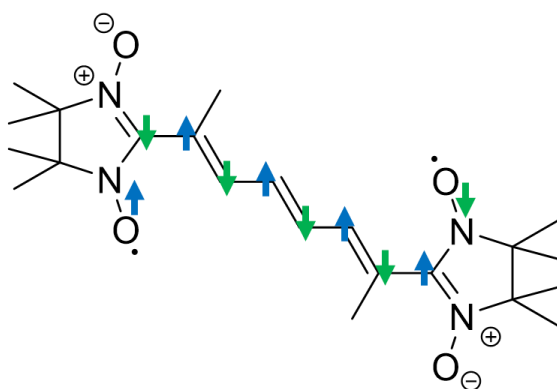


Figure 1-26. Intramolecular magnetic interaction by spin polarization.

(d) Intramolecular Magnetic Interaction in σ -Bridged Biradical

The intramolecular magnetic interaction has been studied not only for the π -conjugation system but also for the non-conjugated framework. Dougherty reported that the cyclobutanediyl and cyclopentanediyl derivatives have ground triplet state.¹⁸ This intramolecular ferromagnetic interaction is interpreted by considering a through-space and through-bond interaction (Figure 1-27(a)). The NBMOs of unpaired electrons directly interact with each other (through-space interaction), producing a large HOMO-LUMO gap. Considering the through-bond interaction, the CH₂ groups have filled p orbitals, regarded as a pseudo π orbital, and interacted with the HOMO. The through-bond interaction raises the energy level of the HOMO to almost the same energy level of the LUMO, leading to the almost degeneration of the HOMO and LUMO and ground triplet state. Dougherty *et al.* also proposed the magnetic interaction through the spiroconjugation system for 1,4,6,9-spiro[4.4]nonatetrayl,¹⁹ and the interaction of the spirobiradical has been experimentally investigated by Kahn *et al.*,²⁰ Tanaka *et al.*,²¹ and Ishida *et al.*²² In the spirobiradical system, its intramolecular magnetic interaction can be interpreted by the interaction of two perpendicular subunits (Figure 1-27(b)). Considering the symmetry of the NBMOs, the interaction of the NBMOs between subunits can occur when the NBMOs are asymmetric to both subunits, leading to the ground singlet state (Figure 1-27(b-1)). In contrast, the NBMOs are degenerate when they are symmetric, leading ground triplet state (Figure 1-27(b-2)). Rassat *et al.* reported that the 2,6-diazaadamantane-*N, N'*-dioxyl derivatives show a ground triplet state.²³ In this case, the azaadamantane skeleton has a D_{2d} symmetry and there is no overlap between the NBMOs of the nitroxyl group, thus reducing the overlap integral (Figure 1-27(c)). Thus, the two NBMOs are degenerated and intramolecular ferromagnetic interaction is observed.

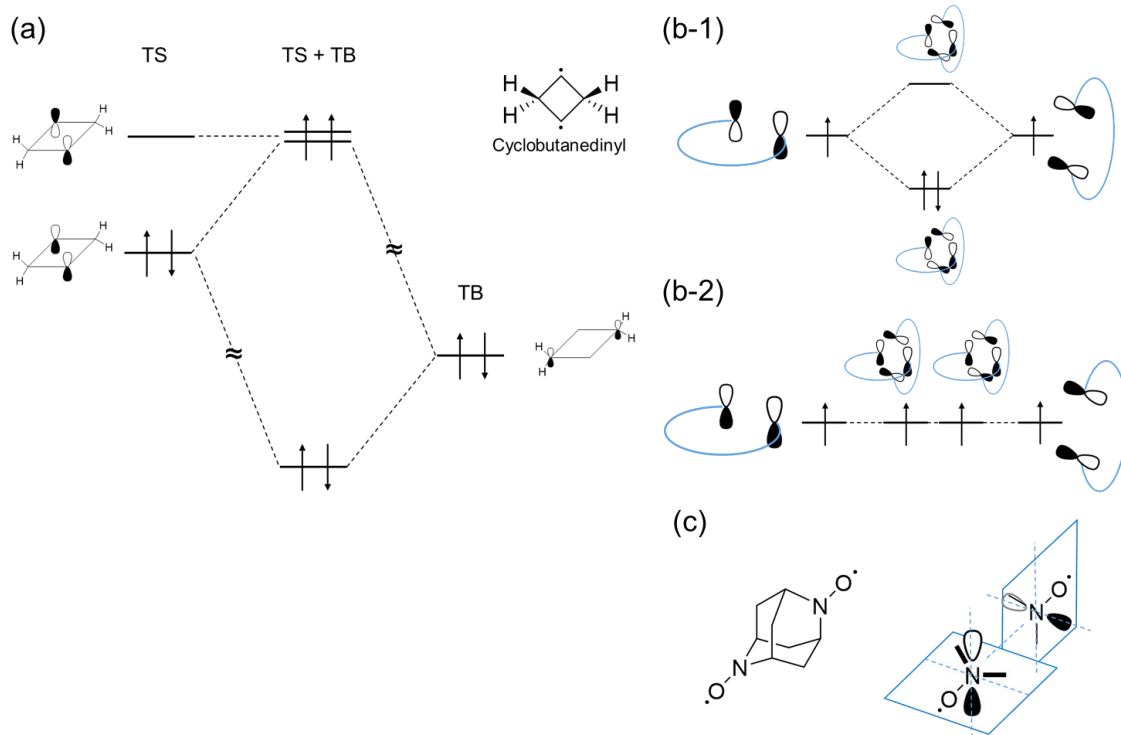


Figure 1-27. Intramolecular magnetic interaction of σ -bridged biradicals. (a) cyclobutanediyl, (b) spirobiradical, (c) 2,6-diazaadamantane- N, N' -dioxy.

1.3.3. Magnetic Properties of Organic Radicals

(a) One-Dimensional Heisenberg Chain Model

The Heisenberg chain model is suitable for the situation when there is the same magnitude of interaction between the close contact of the spin centers in a 1D chain. When the ferromagnetic interaction is dominant in the chain with the $S = 1/2$ spin, the paramagnetic susceptibility χ_p is described by equation 1-17, which is the approximate formula reported by Baker *et al.*²⁴

$$\chi_p = \frac{N_A g^2 \beta^2}{k_B T} F(J, T) \quad (\text{eq. 1-17})$$

$$F(J, T) = \frac{1}{4} [(1 + 5.7979916x + 16.902653x^2 + 29.376885x^3) + 29.832959x^4 + 14.036918x^5 / (1 + 2.7979916x + 7.0086780x^2 + 8.6538644x^3 + 4.5743114x^4)]^{2/3}$$

$$x = \frac{J}{2k_B T}$$

k_B : Boltzmann constant g : g-factor

β : Bohr's magneton

In the case of the 1D antiferromagnetic Heisenberg chain with $S = 1/2$ spin, χ_p is described by equation 1-18, which is the approximate formula reported by Bonner and Fisher²⁵.

$$\chi_p = \frac{N_A g^2 \beta^2}{k_B T} \frac{1 - 0.25 + 0.14995x + 0.30094x^2}{1 + 1.9862x + 0.68854x^2 + 0.0626x^3} \quad (\text{eq. 1-18})$$

$$x = \frac{|J|}{k_B T}$$

(b) Dimer model (Bleaney-Bowers model)²⁶

Regarding the magnetic interaction between $S = 1/2$ spins, the Hamiltonian and paramagnetic susceptibility χ_p are described below (equations 1-19, 1-20).

$$\mathcal{H} = -2J S_1 \cdot S_2 \quad (\text{eq. 1-19})$$

$$\chi_p = \frac{N_A g^2 \beta^2}{k_B T} \frac{1}{3 + \exp\left(\frac{-2J}{k_B T}\right)} \quad (\text{eq. 1-20})$$

1.3.4. Bistability in Organic Radical Solids

Several organic radicals display a magnetic bistability that originated from a phase transition (Figure 1-28). The galvinoxyl radical, known as Coppinger's radical, exhibits a ferromagnetic interaction with positive Weiss value $\theta = +19$ K in the high temperature phase ($T > 85$ K), however, the magnetic phase transition to the antiferromagnetic phase occurred below 85 K. Kinoshita *et al.* described that the precursor of the galvinoxyl radical had the same molecular arrangement in the crystal and solid dispersion of the galvinoxyl radical and its precursor.²⁷ The magnetic susceptibility and heat capacity measurement revealed that the radical precursor suppressed the phase transition, and the dispersion samples display a 1D chain ferromagnetic interaction with $J = +56.5$ cm⁻¹.

1,3,2-Dithiazolyl radicals also exhibit a magnetic bistability. 1,3,5-Trithia-2,4,6-triazapentalenyl (TTTA),²⁸ and 1,3,2-pyrazinothiazol-2-yl (PDTA)²⁹ display a Spin Peierls-like magnetic phase transition with hysteresis. Their magnetic phase transitions are attributed to the rotation of the molecules to form a dimer during the cooling process by keeping their slipped π -stacked structure and the transitions are fully reversible.

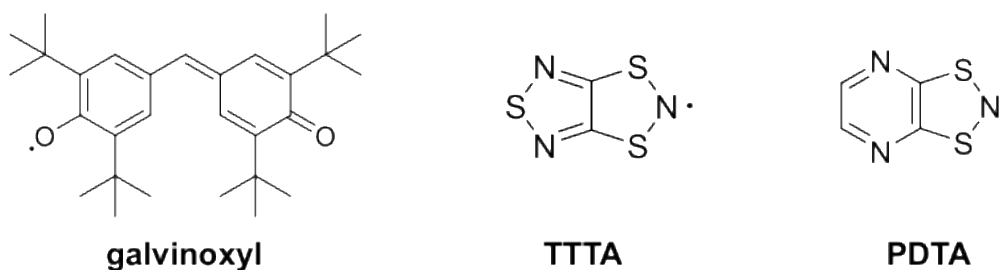


Figure 1-28. Molecular structure of organic radicals exhibiting a magnetic phase transition.

1.4. Purpose of Study

Based on the background described in chapter 1, stable organic radicals act as a spin center for paramagnetic species and they exhibit various magnetic properties depending on their molecular assembly. Thanks to the existence of unpaired electrons, organic radicals show not only a magnetic interaction, but also a conductivity, electronic bistability. Therefore, organic radical derivatives are promising building blocks for novel functional materials.

In order to construct novel molecule-based magnetic materials using organic radicals as the paramagnetic source, it is required to align their magnetic moments. Thus, it is important to reveal their steric contribution, electronic state and magneto-structural correlation because the construction design guide for an organic ferromagnet has not yet established. In this thesis, to control the inter- and intramolecular magnetic interactions for establishment of the molecular design of magnetic materials, the author focused on the two radical systems, i.e. benzotriazinyl radicals and pyrroline *N*-oxyl attached biradicals. A summary of the chapters is shown below.

In chapter 2, the synthesis and substituent effect on the physicochemical properties of the 3-*tert*-butyl benzotriazinyl radical derivatives are reported. To control the intermolecular magnetic interaction, it is required to control the molecular assembly, and the benzotriazinyl radicals are designed based on a crystallographic engineering approach. The trifluoromethyl group-introduced derivative at the 7 position (**7CF3**) forms a 1D ferromagnetic chain. Notably, the cyano group introduced derivative at the 6 position (**6CN**) exhibits a spin transition with a small hysteresis at *ca.* 280 K. In spite of the carrying bulky *tert*-butyl group, the 3-*tert*-butyl benzotriazinyl radical derivatives exhibit an intermolecular interaction through the π -conjugation system. The experimental result of **6CN** suggested that the construction of a 1D columnar structure with a dimer may be the one of designs to exhibit a spin transition behavior involving the structural phase transition.

In chapter 3, the synthesis and physicochemical properties of the pyrroline *N*-oxyl attached

benzotriazinyl hetero biradicals are reported. To control the intramolecular magnetic interaction, many experimental and theoretical studies about the interaction through the π -conjugation framework have been carried out. Considering the polyradical, decomposition and disproportionation often occur in the π -conjugation framework. On the other hand, a cyclic nitroxide, such as **TEMPO**, shows a high stability against air and moisture, however, it has been considered not to exhibit a strong intramolecular magnetic interaction due to the localization of their SOMO and spin density. If cyclic nitroxides are utilized for the spin center of a magnetic polyradical, the stability of a polyradical could be improved. Therefore, it is important to discuss the magnetic interaction through the non-conjugated framework. Pyrroline *N*-oxyl attached the benzotriazinyl hetero biradicals exhibited an unexpected large intramolecular antiferromagnetic interaction attributed to the effective the SOMO-SOMO interaction.

In chapter 4, the synthesis and physicochemical properties of the pyrroline *N*-oxyl attached verdazyl and nitronyl nitroxide hetero biradicals are reported. The experimental and computational results revealed that the prepared biradicals have a ground triplet state attributed to the intramolecular spin-spin interaction between the spin centers.

In chapter 5, a computational study of hetero biradicals carrying the pyrroline *N*-oxyl for evaluation of the intramolecular magnetic interaction through the non-conjugated framework is described. It suggests that the magnetic interaction through the non-conjugated framework is attributed to the through σ -bond, and the SOMO-SOMO and spin-spin interactions between nitroxyl moiety and vinylic carbons. The guideline for the presence of the intramolecular magnetic interaction through the non-conjugated framework based on experimental and computational studies is described.

In chapter 6, the conclusion and future scope are presented.

In chapter 7, the detailed synthetic procedures are described.

References in Chapter 1

- (a) K. Adachi, *Busseikagakusensho Kagoubutujisei - kyokuzaisupinkei* [Material Science Library Magnetism of Comounds – Localized Spin System], Shokabo, Tokyo, Japan, 1996.
 - (b) K. Adachi, *Busseikagakusensho Kagoubutujisei - Henrekisupinkei* [Material Science Library Magnetism of Comounds – Itinerant Spin System], Shokabo, Tokyo, Japan, 1996.
- K. Yoshida, *Jisei* [Magnetism], Iwanamishoten, Tokyo, Japan, 1991.
- (a) P. M. Lahti ed., *Magnetic Properties of Organic Materials*, Marcel Dekker, New York, 1999.
 - (b) R. G. Hicks ed., *Stable Radicals: Fundamentals and Applied Aspects of Odd-Electron Compounds*, Wiley, Chichester, UK, 2010.
 - (c) C. Chatgililoglu and A. Studer ed., *Encyclopedia of Radicals in Chemistry, Biology and Materials*, Wiley, Hoboken, NJ, 2012.
 - (d) A. Rajca, *Chem. Rev.*, **1994**, *94*, 871.
 - (e) I. Ratera, J. Veciana, *Chem. Soc. Rev.* **2012**, *41*, 303.
 - (f) M. Abe, *Chem. Rev.*, **2013**, *113*, 7011.
- H. Longuet-Higgins, *J. Chem. Phys.*, **1950**, *18*, 265.
- A. A. Ovchinnikov, *Theoret. Chim. Acta*, **1978**, *47*, 297.
- W. Borden, E. R. Davidson, *J. Am. Chem. Soc.*, **1977**, *99*, 4587.
- H. M. McConnell, *J. Phys. Chem.*, **1963**, *39*, 1910.
- K. Yoshizawa, R. Hoffmann, *J. Am. Chem. Soc.*, **1995**, *117*, 6921.
- H. M. McConnell, *Proc. Robert A. Welch Found. Conf. Chem. Res.*, **1967**, *11*, 144.
- J. S. Miller, J. C. Calabrese, H. Rommelmann, S. Chittipeddi, J. H. Zhang, W. M. Reiff, A. J. Epstein, *J. Am. Chem. Soc.*, **1987**, *109*, 769.
- A. L. Buchachenko, *Mol. Cryst. Liq. Cryst.*, **1989**, *176*, 307.
- (a) H. Haick, D. Cahen, *Acc. Chem. Res.*, **2008**, *41*, 359.
 - (b) Y. Morita, S. Nishida, T. Murata, M. Moriguchi, A. Ueda, M. Satoh, K. Arifuku, K. Sato, T. Takui, *Nat. Mater.*, **2011**, *10*, 947.
 - (c) A. Sarkar, M. E. Itkis, F. S. Tham, R. C. Haddon, *Chem. – Eur. J.*, **2011**, *17*, 11576.
 - (d) A. Mailman, S. M. Winter, X. Yu, C. M. Robertson, W. Yong, J. S. Tse, R. A. Secco, Z. Liu, P. A. Dube, J. A. K. Howard, R. T. Oakley, *J. Am. Chem. Soc.*, **2012**, *134*, 9886.
- (a) O. H. Griffith, A. S. Waggoner, *Acc. Chem. Res.*, **1969**, *2*, 17.
 - (b) J. F. W. Keana, *Chem. Rev.*, **1978**, *78*, 37.
 - (c) Q. Z. Ni, E. Daviso, T. V. Can, E. Markhasin, A. K. Jawla, T. M. Swager, R. J. Temkin, J. Herzfeld, R. G. Griffin, *Acc. Chem. Res.*, **2013**, *46*, 1933.
 - (d) E. G. Bagryanskaya, O. A. Krumkacheva, M. V. Fedin, S. R. A. Marque, *Method Enzymol.*, **2015**, *563*, 365.
- (a) M. Kinoshita, *Jpn. J. Appl. Phys.*, **1994**, *33*, 5718.

- (b) J. S. Miller, M. Drillon, *Magnetism: Molecules to Materials II, Molecule-Based Materials*, Wiley-VCH, New York, 2001.
- (c) H. Iwamura, *Polyhedron*, **2013**, *66*, 3.
15. J. Guasch, X. Fontrodona, I. Ratera, C. Rovira, J. Veciana, *Acta Cryst.*, **2013**, *C69*, 255.
16. (a) Y. Kurita, *Denshisupinkyomei nyumon* [Tutorial of Electron Spin Resonance], Kodansha, Tokyo, Japan, 1975.
- (b) J. Yamauchi, *Jikikyomei-ESR -Denshisupinnobunkougaku-* [Magnetic Resonance-ESR - Spectroscopy of Electron Spin-], Saiensusha, Tokyo, Japan, 2006.
17. C. Stroh, P. Turek, R. Ziessel, *Chem. Commun.*, **1998**, 2337.
18. D. A. Dougherty, *Acc. Chem. Res.*, **1991**, *24*, 88.
19. L. McElwee-White, W. A. Goddard III, D. A. Dougherty, *J. Am. Chem. Soc.*, **1984**, *106*, 3461.
20. N. L. Frank, R. Clérac, J-P. Sutter, N. Daro, O. Kahn, C. Conlon, M. T. Green, S. Golhen, L. Ouahab, *J. Am. Chem. Soc.*, **2000**, *122*, 2053.
21. A. Ito, M. Urabe, K. Tanaka, *Angew. Chem. Int. Ed.*, **2003**, *42*, 921.
22. T. Ishida, M. Ooishi, N. Ishii, H. Mori, T. Nogami, *Polyhedron*, **2007**, *26*, 1793.
23. (a) R-M. Dupeyre, A. Rassat, J. Ronzaud, *J. Am. Chem. Soc.*, **1974**, *96*, 6559.
- (b) R. Chiarelli, M. A. Novak, A. Rassat, J. L. Tholence, *Nature*, **1993**, *363*, 147.
24. G. A. Baker Jr., G. S. Rushbrooke, H. E. Gilbert, *Phys. Rev. A: At., Mol., Opt. Phys.*, **1964**, *135*, 1272.
25. J. Bonner, M. Fisher, *Phys. Rev.*, **1964**, *135*, A640.
26. B. Bleaney, K. D. Bowers, *Proc. R. Soc. A*, **1952**, *214*, 451.
27. K. Awaga, T. Sugano, M. Kinoshita, T. Matsuo, H. Suga, *J. Chem. Phys.* **1987**, *87*, 3062.
28. W. Fujita, K. Awaga, *Nature*, **1999**, *286*, 261.
29. J. L. Brusso, O. P. Clements, R. C. Haddon, M. E. Itkis, A. A. Leitch, R. T. Oakley, R. W. Reed, J. F. Richardson, *J. Am. Chem. Soc.*, **2004**, *126*, 8256.

Chapter 2: Substituent Effects on Magnetic Properties of Benzotriazinyl Radicals

2.1. Introduction

Physicochemical properties of π -delocalized radicals have been investigated to develop the novel functional materials. In order to construct the molecule-based ferromagnet, the magnetic moment of molecules has to make three-dimensional network with ferromagnetic interaction. In the field of molecule-based magnetism, the magnetic property of organic radicals significantly depends on their molecular assembly. Hence, it is required to control the molecular assembly by crystallographic engineering approach¹ as described below; with the assistance of non-covalent bond such as hydrogen-bond, π - π interaction and halogen-bond, one-dimensional columnar structure is formed by self-assembly of the molecules with the magnetic interaction, then, the construction of intercolumnar interaction, resulting the three-dimensional magnetic network (Figure 2-1).

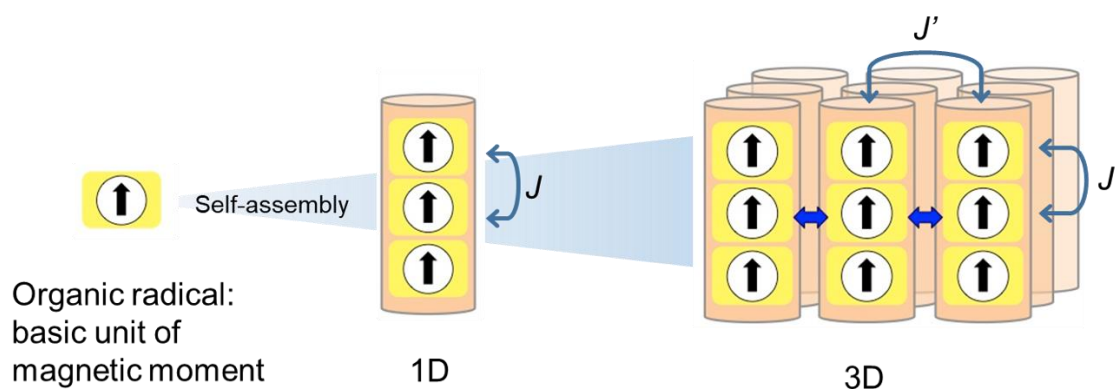


Figure 2-1. The strategy for constructing molecule-based ferromagnet based on crystallographic engineering approach. J and J' represent the magnetic interaction within and between columns.

Verdazyl radicals, which was firstly reported by Kuhn *et al*² (Figure 2-2(a)), are one of hydrazyl radical derivatives. Several substituents can be introduced to 1-, 3- and 5-position and functional group transformation can be proceeded without protection of radical moiety,³ verdazyl radical derivatives are promising species as building block for functionalized material. Their unpaired electron delocalizes on N1-N2-C3-N4-N5 moiety and the nodal planes of SOMO are on C3 and C6 atoms⁴ (Figure 2-2(b)). Regarding spin density, there is small distribution on C3 substituent due to the spin polarization effect. The SOMO and spin density delocalize to substituents of N1 and N5 atoms. In the case of N1 or N5 substituents as aromatic rings, they can contribute to form π - π interaction and exhibit intermolecular magnetic interaction because unpaired electron can delocalize to the aromatic rings as shown in Figure 2-2(c). According to the ESR and computational studies, spin density distribution on nitrogen atoms are different in depending on C6 substituent. In Kuhn's verdazyl, there is slightly larger spin density on N1 and N5 atoms than that of N2 and N4 atoms. On the other hand, 6-oxoverdazyl analogue have larger spin density on N2 and N4 atoms due to the electron withdrawing character of carbonyl group.⁵ The magnetic, spectroscopic and electrochemical studies of verdazyl radical derivatives have been reported. For example, the observation of spin-Peierls transition in 3-(4-cyanophenyl)-1,5-dimethyl-6-oxoverdazyl radical at 16 K was reported by Mukai *et al*.⁶ and 6-oxo- and thioverdazyl radicals have been utilized for mesogenic group for paramagnetic liquid crystals reported by Kaszyński *et al*.⁷

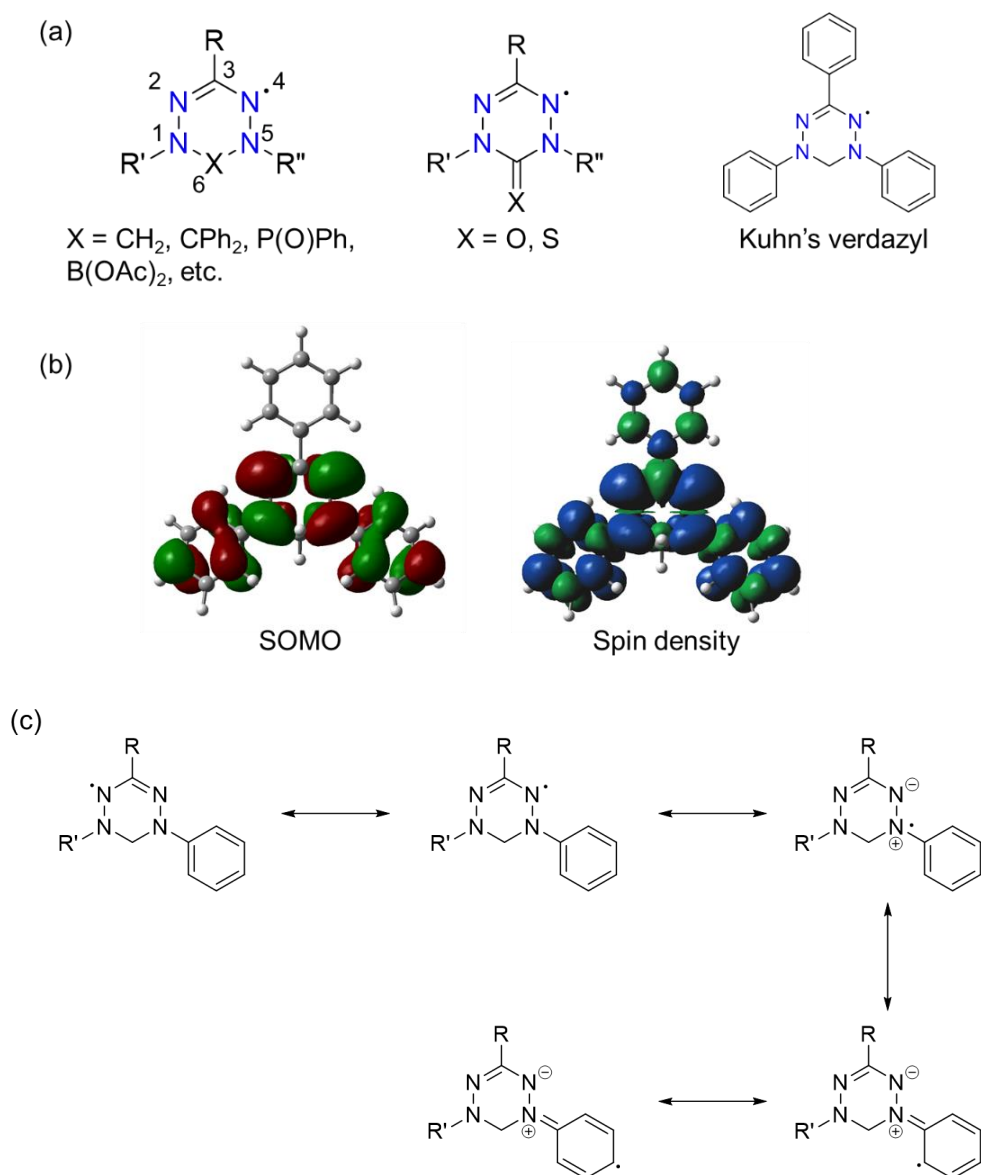


Figure 2-2. (a) Molecular structure of verdazyl radicals. (b) SOMO and spin density distributions of Kuhn's verdazyl. (c) Resonance structure of verdazyl radical.

Benzotriazinyl radicals are also known as a kind of π -delocalized hydrazyl radical and first reported by Blatter *et al*⁸. The structure is similar to verdazyl radicals. *N*-aryl substituent of verdazyl radical is fused to N5-C6 bond and N5 atom replaced to carbon atom, resulting the formation of benzotriazinyl structure. Their unpaired electron delocalizes over the molecule except for substituent at 3-position due to the existence of node of SOMO and electronic state is tunable by functionalization

of benzo ring (Figure 2-3). Since the facile preparation of benzotriazinyl radicals was reported by Koutentis *et al*⁹, several synthetic routes¹⁰ and transformation of functional groups,¹¹ and computational study¹² have been reported in a decade. Because of the enhanced stability for moisture and aerial oxidation¹³, transformations of functional groups and metal-catalyzed coupling reactions¹¹ are undergone in practical yield in the similar fashion of nonconjugated nitroxides.

In terms of the molecular arrangement, benzotriazinyl radicals tend to form columnar structure derived from π - π interaction. It indicates that their self-assembling property is suitable to basic constitutional elements for magnetic material because of the prediction of strong magnetic interaction through π - π interaction. Regarding magnetic property, they exhibit interesting property in attribution to their unique electronic state, whose SOMO distributes like that of even alternant hydrocarbon. 7-Furanyl derivative **7FB** has thermally excited triplet state arising from π - π interaction¹⁴. 3-Trifluoromethyl derivative **3TB** exhibits spin transition between diamagnetic and paramagnetic state with negligible hysteresis.¹⁵ 3-(2-Pyridyl) derivative play a role of paramagnetic ligand for metal complex¹⁶ and 3-(3-vinylphenyl) derivative exhibited metamagnetism.¹⁷ As the analogue of benzotriazinyl radical, **TPHA** shows twitter ionic character¹⁸ and planar benzotriazinyl radicals are also stable in the air.¹⁹ Therefore, as shown above, benzotriazinyl radical derivatives are promising species for functionalized materials.

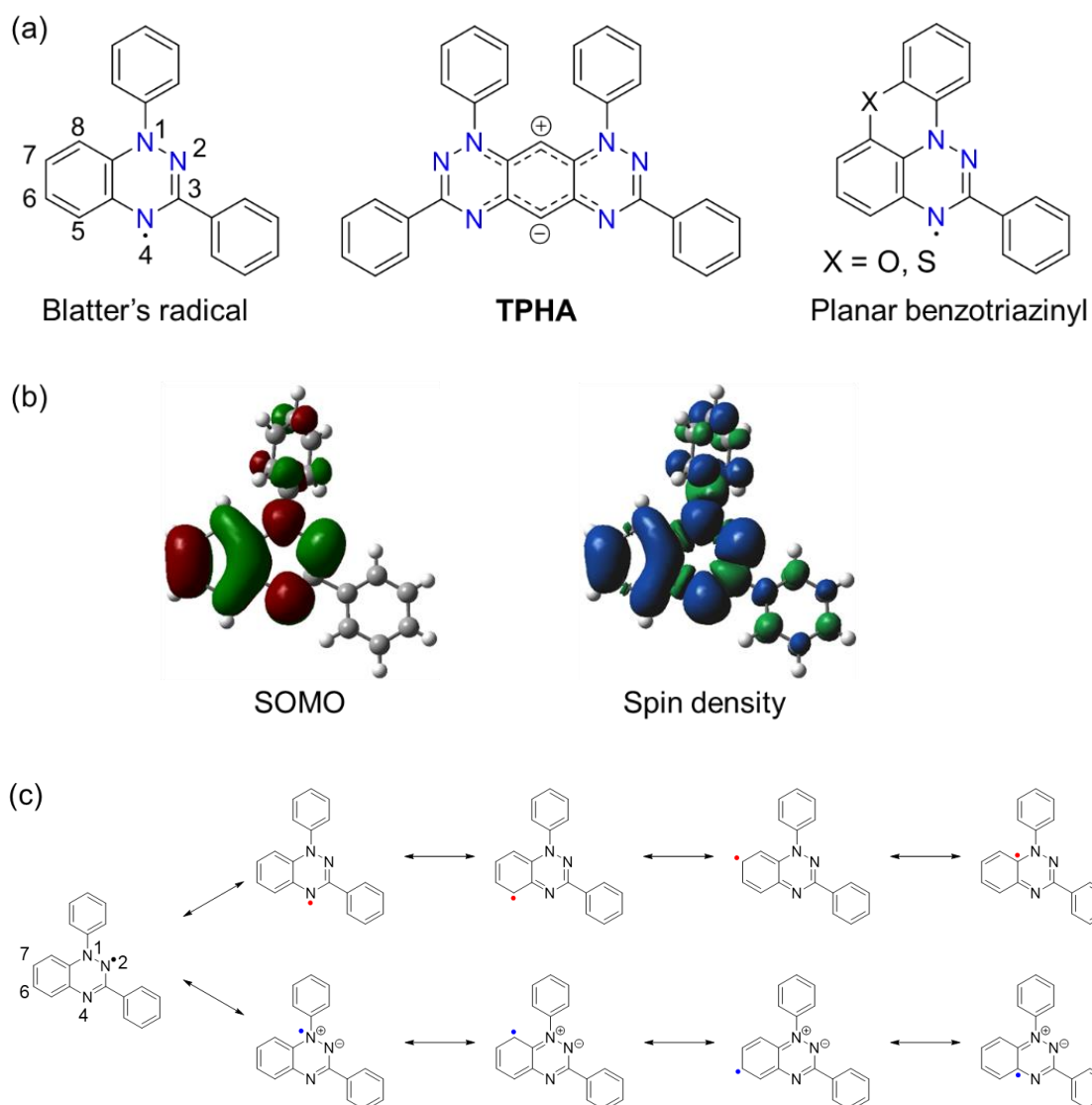


Figure 2-3. (a) Molecular structure of benzotriazinyl radicals. (b) SOMO and spin density distributions of Blatter's radical. (c) Resonance structure of Blatter's radical.

Benzotriazinyl radicals exhibit various interesting magnetic properties arising from their unique unpaired electron distribution. Spectroscopic²⁰ and magnetic²¹ properties of 3-*tert*-butyl benzotriazinyl radical **1** have been reported, however, magneto-structural correlation of 3-*tert*-butyl benzotriazinyl analogues have not been reported because bulky *tert*-butyl group prevent the contact of π -conjugated system and the magnitude of magnetic interaction will be weakened. In this point of view, the weak π - π interaction allow to enhance the substituent effect for their electronic state and their molecular

assembly. Hence, in chapter 2, the spectroscopic property and magneto-structural correlation of 3-*tert*-butyl benzotriazinyl radical derivatives carrying electron withdrawing group, *i.e.* trifluoromethyl and cyano groups, are discussed (Figure 2-4). These functional groups produce large dipole moments for molecule due to large electronegativity and encourage the molecule to assembly with canceling dipole moment in crystal structure.

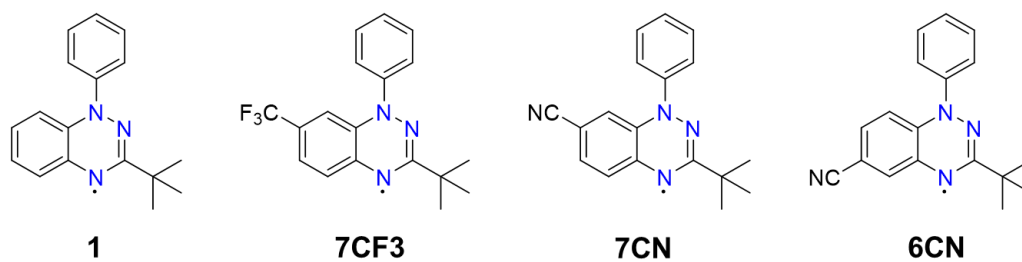
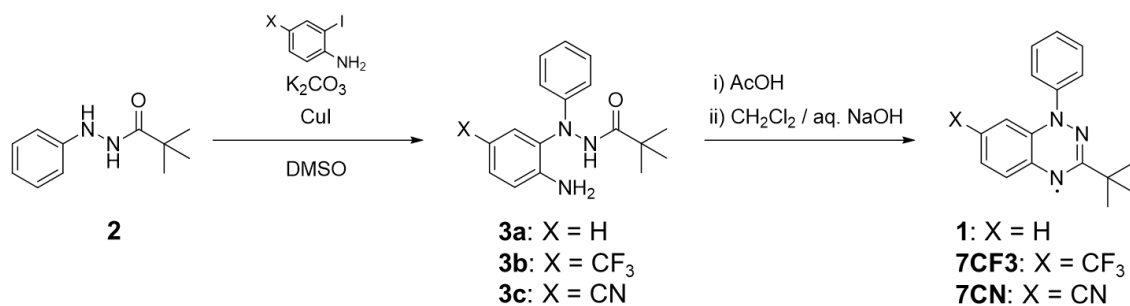


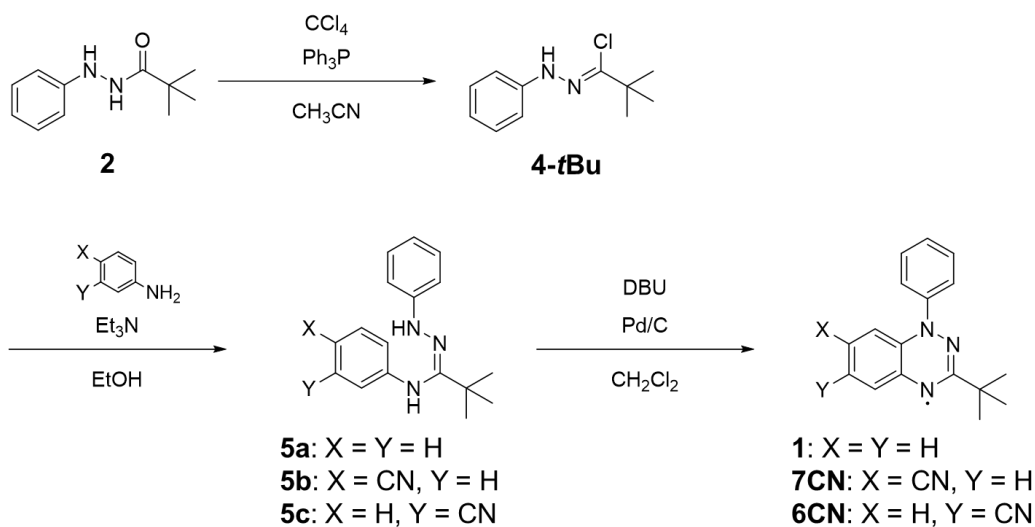
Figure 2-4. Molecular structure of 3-*tert*-butyl benzotriazinyl radicals.

2.2. Synthesis

Benzotriazinyl radicals **1**, **7CF3**, **7CN** were synthesized according to Scheme 2-1. Hydrazide **2** was obtained by condensation of phenylhydrazine and pivaloyl chloride. Cu-catalyzed C-N coupling²² between **2** and 4-substituted 2-iodoaniline gave radical precursor **3a**, which were not purified due to the instability of **3b** and **3c**. Condensation and aerial oxidation under basic condition to afford 3-*tert* benzotriazinyl radicals (**1**: 34%, **7CF3**: 26%, **7CN**: 8%). Instability of **3** reflected the low yield, therefore, another synthetic route was introduced (Scheme 2-2). After chlorination of **2**, condensation between **4-*t*Bu** and substituted aniline gave radical precursor **5** with moderate yield. Oxidative cyclization was proceeded under DBU and 10% Pd/C to afford **1** and **7CN**. Total yields (**1**:64%, **7CN**:27%) were improved compared to that of previous synthetic route (Scheme 2-2). Thus, **6CN** was prepared in the same procedure according to Scheme 2-2 (total yield:15%).



Scheme 2-1. Synthetic route of benzotriazinyl radicals via Cu-catalyzed coupling.



Scheme 2-2. Synthetic route of benzotriazinyl radicals via oxidative cyclization with Pd/C.

2.3. Crystallographic Analysis

Single crystals of **1**, **7CF3**, **7CN** and **6CN** suitable for X-ray analysis were obtained by slow evaporation method. The ORTEP drawings of benzotriazinyl radicals are shown in Figure 2-5 and selected bond lengths and dihedral angle between phenyl ring and amidorazonyl ring are shown in Table 2-1. Crystallographic data are shown in Table 2-2. Single crystal of **6CN** exhibits two polymorphs in response to the temperature (denoted as HT and LT phases, respectively), which are shown below. The bond lengths of π -conjugated system are similar values and suggested delocalization of unpaired electron. The dihedral angle of **7CN** is smaller than that of other derivatives, which is attributed to the packing effect.

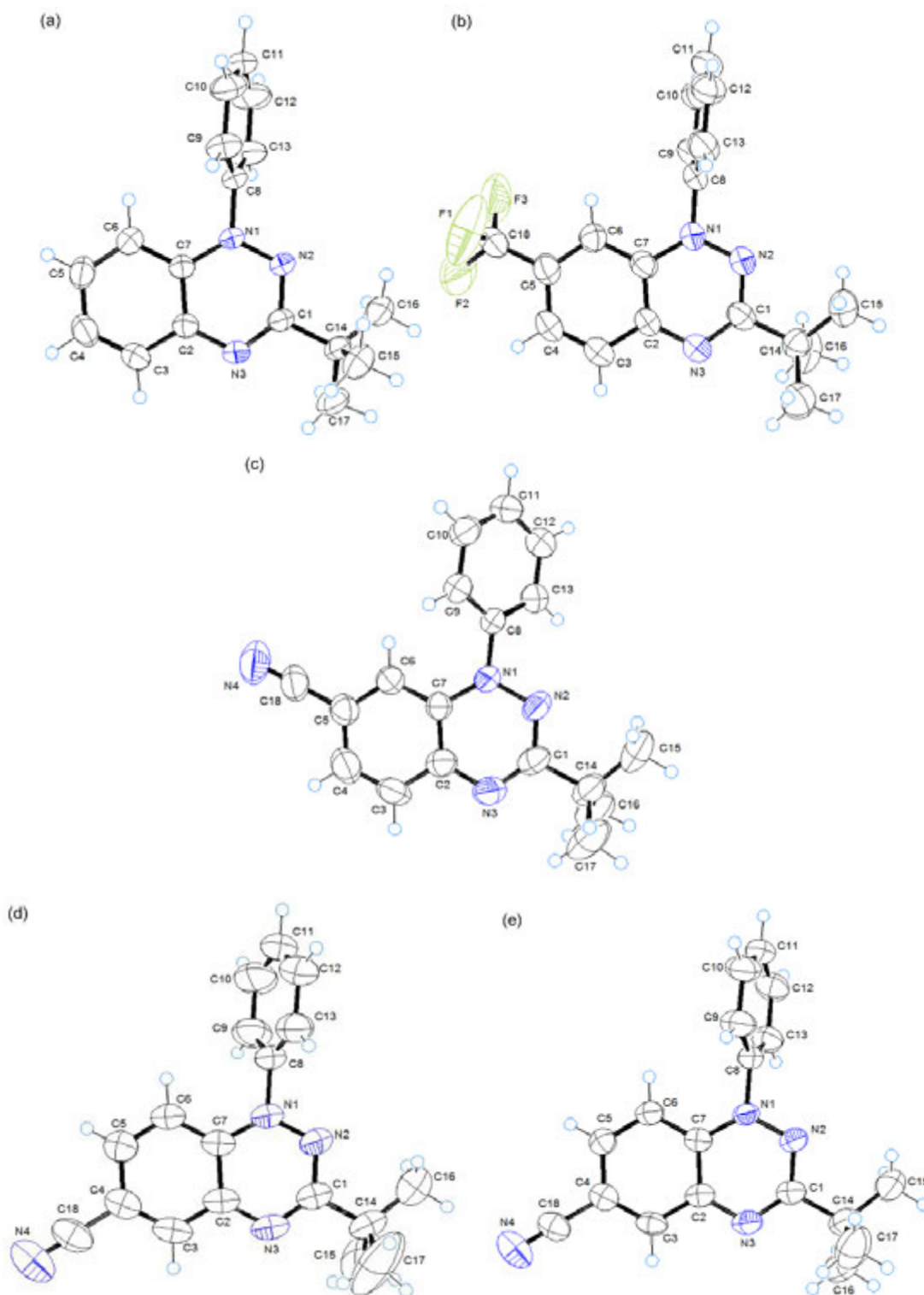


Figure 2-5. ORTEP drawings of (a) **1** (b) **7CF3** (c) **7CN** (d) **6CN_HT** (300 K) (e) **6CN_LT** (263 K) with 50% thermal ellipsoids. [*New J. Chem.*, **2015**, *39*, 4783] - Reproduced by permission of The Royal Society of Chemistry (RSC) on behalf of the Centre National de la Recherche Scientifique (CNRS) and the RSC.

Table 2-1. Selected bond lengths and dihedral angle of 3-*tert*-butyl benzotriazinyl radicals.

Compound	1	7CF3	7CN	6CN	
				HT (300 K)	LT (263 K)
$d_{\text{N1-N2}} / \text{\AA}$	1.3663(16)	1.357(6)	1.375(3)	1.360(3)	1.364(3)
$d_{\text{N2-C1}} / \text{\AA}$	1.3372(17)	1.338(7)	1.324(4)	1.330(3)	1.325(4)
$d_{\text{C1-N3}} / \text{\AA}$	1.3265(19)	1.331(7)	1.335(4)	1.332(3)	1.339(4)
$d_{\text{N3-C2}} / \text{\AA}$	1.3684(19)	1.368(7)	1.365(4)	1.364(3)	1.368(4)
$d_{\text{C2-C3}} / \text{\AA}$	1.402(2)	1.393(8)	1.400(5)	1.392(4)	1.399(4)
$d_{\text{C3-C4}} / \text{\AA}$	1.364(3)	1.380(9)	1.360(5)	1.371(4)	1.378(4)
$d_{\text{C4-C5}} / \text{\AA}$	1.390(3)	1.389(8)	1.384(5)	1.395(4)	1.389(4)
$d_{\text{C5-C6}} / \text{\AA}$	1.373(2)	1.371(8)	1.378(4)	1.366(3)	1.384(4)
$d_{\text{C6-C7}} / \text{\AA}$	1.390(2)	1.412(8)	1.381(4)	1.388(3)	1.394(4)
$d_{\text{C2-C7}} / \text{\AA}$	1.4109(19)	1.401(7)	1.402(4)	1.416(3)	1.408(4)
$d_{\text{N1-C7}} / \text{\AA}$	1.3806(18)	1.382(7)	1.384(4)	1.375(3)	1.375(4)
$d_{\text{C18-F1}} / \text{\AA}$	-	1.291(9)	-	-	-
$d_{\text{C18-F2}} / \text{\AA}$	-	1.296(9)	-	-	-
$d_{\text{C18-F3}} / \text{\AA}$	-	1.258(8)	-	-	-
$d_{\text{C18-N4}} / \text{\AA}$	-	-	1.137(5)	1.143(4)	1.141(4)
dihedral angle / °	73.85(6)	82.18(17)	45.236(80)	68.408(97)	69.858(130)

Table 2-2. Crystallographic data of 3-*tert*-butyl benzotriazinyl radicals.

	1	7CF3	7CN	6CN_HT	6CN_LT
Chemical formula	C ₁₇ H ₁₈ N ₃	C ₁₈ H ₁₇ F ₃ N ₃	C ₁₈ H ₁₇ N ₄	C ₁₈ H ₁₇ N ₄	C ₁₈ H ₁₇ N ₄
Formula weight	264.34	332.34	289.35	289.35	289.35
Temperature / K	296	296	296	300	263
Crystal size / mm ³	0.85 × 0.73 × 0.20	0.78 × 0.32 × 0.12	0.74 × 0.17 × 0.08	1.24 × 0.54 × 0.06	1.24 × 0.54 × 0.06
Space group	<i>P2₁/n</i> (No. 14)	<i>Cc</i> (No. 9)	<i>I2/a</i> (No.15)	<i>I2/a</i> (No.15)	<i>P</i> -1 (No. 2)
<i>a</i> / Å	9.6624(13)	5.592(2)	18.709(3)	26.317(4)	6.8527(6)
<i>b</i> / Å	9.8119(11)	18.904(7)	7.8316(12)	6.7524(7)	9.1813(9)
<i>c</i> / Å	15.7422(18)	15.882(5)	21.501(6)	18.003(2)	13.1091(12)
α / °	90	90	90	90	86.834(3)
β / °	104.595(4)	92.487(11)	90.945(4)	90.578(3)	80.616(3)
γ / °	90	90	90	90	74.983(3)
<i>V</i> / Å ³	1444.3(3)	1677.3(11)	3149.9(11)	3199.0(7)	785.88(13)
<i>Z</i>	4	4	8	8	2
<i>d</i> _{calc} / g cm ⁻³	1.216	1.316	1.220	1.202	1.223
μ / mm ⁻¹	0.074	0.103	0.075	0.074	0.075
F(000)	564	692	1224	1224	306
θ (min, max) / °	2.25, 29.38	2.15, 27.35	2.18, 23.02	2.73, 24.44	2.77, 25.10
	-13 ≤ <i>h</i> ≤ 13	-6 ≤ <i>h</i> ≤ 7	-19 ≤ <i>h</i> ≤ 20	-30 ≤ <i>h</i> ≤ 30	-7 ≤ <i>h</i> ≤ 8
Index ranges	-10 ≤ <i>k</i> ≤ 13	-19 ≤ <i>k</i> ≤ 24	-8 ≤ <i>k</i> ≤ 8	7 ≤ <i>k</i> ≤ 7	-10 ≤ <i>k</i> ≤ 10
	-21 ≤ <i>l</i> ≤ 17	-17 ≤ <i>l</i> ≤ 20	-23 ≤ <i>l</i> ≤ 22	-18 ≤ <i>l</i> ≤ 20	0 ≤ <i>l</i> ≤ 15
Measured reflection	13831	4642	10772	13670	2512
Independent reflection (<i>R</i> _{int})	3762 (0.0357)	2871 (0.0559)	2196 (0.0486)	2605 (0.0641)	2512 (-)
Obs. reflection (<i>I</i> ≥ 2σ(<i>I</i>))	2323	1725	1422	1929	1707
Goodness of fit on <i>F</i> ²	0.860	1.060	1.380	1.396	1.103
<i>R</i> , <i>R</i> _w (<i>I</i> ≥ 2σ(<i>I</i>))	0.0523, 0.1345	0.0662, 0.1736	0.0702, 0.1891	0.0712, 0.2160	0.0647, 0.1763
<i>R</i> , <i>R</i> _w (all data)	0.0929, 0.1683	0.1132, 0.2069	0.1153, 0.2190	0.0901, 0.2370	0.0975, 0.2128
Resd density (min, max) / e Å ⁻³	-0.345, 0.192	-0.264, 0.348	-0.300, 0.438	-0.190, 0.289	-0.276, 0.220

Radical **1** belongs to monoclinic crystal system and $P2_1/c$ space group. In the crystal structure, **1** form 1D columnar structure and antiparallely stacked in the column along b axis, however, there is no effective interaction to form columnar structure (Figure 2-6). It suggests that π - π interaction didn't work as driving force to form columnar structure due to the steric effect of *tert*-butyl group.

Radical **7CF3** belongs to monoclinic crystal system and Cc space group. **7CF3** form slipped 1D columnar structure along a axis and parallelly stacked with 4.35 Å (Figure 2-7). The bulky *tert*-butyl group prevents the contact of π -conjugated system. Regarding the arrangement of the column, it aligned to cancel the dipole moment between the columns.

Radical **7CN** belongs to monoclinic crystal system and $I2/a$ space group. **7CN** also form 1D columnar structure arising from π - π interaction between phenyl ring and amidrazonyl ring with *ca.* 3.6 Å separation (Figure 2-8).

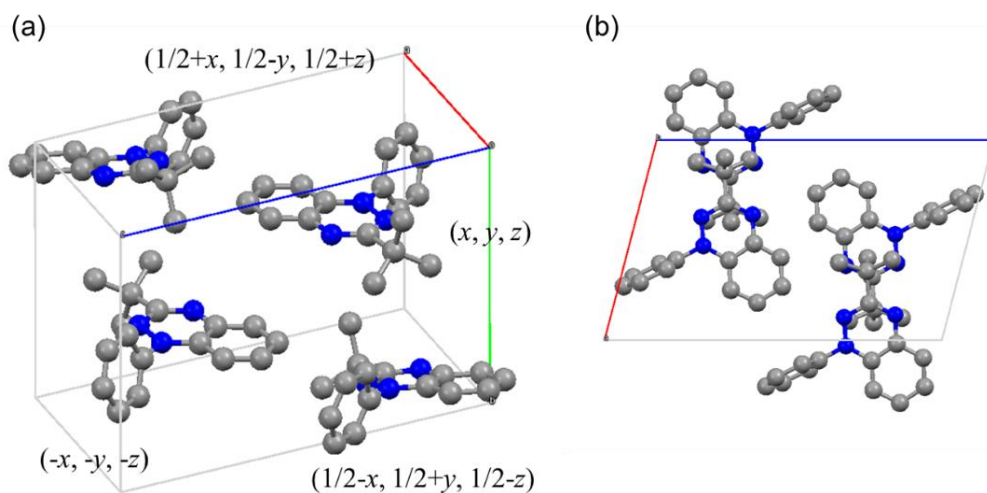


Figure 2-6. (a) Crystal structure and (b) b -axis projection of **1**. Hydrogen atoms are omitted for clarity.

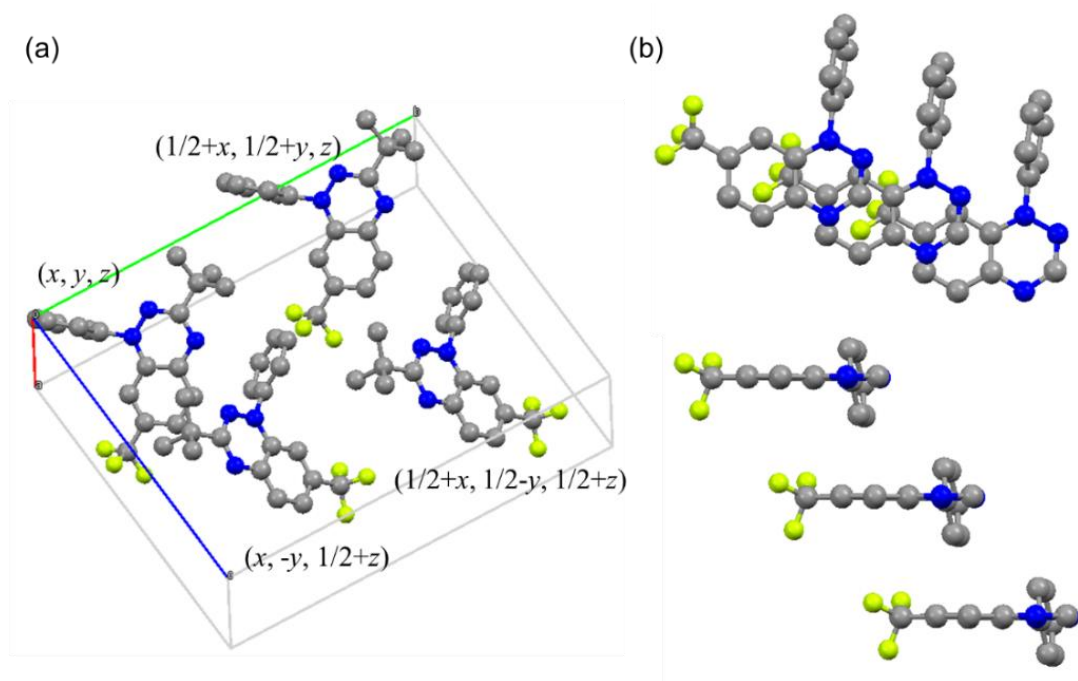


Figure 2-7. (a) Crystal structure and (b) columnar structure of 7CF3. *tert*-Butyl group and hydrogen atoms are omitted for clarity.

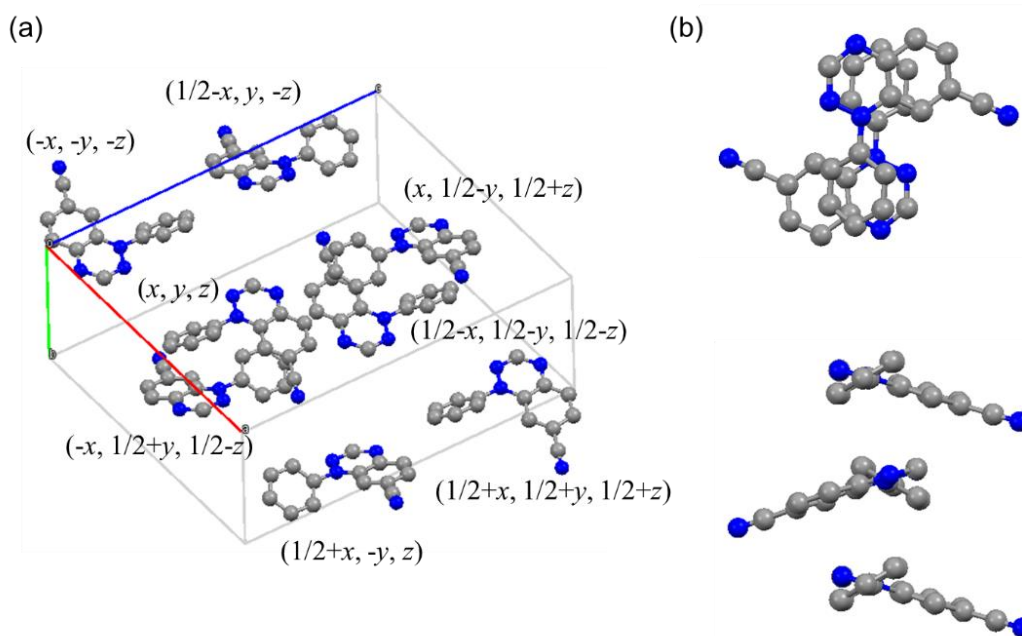


Figure 2-8. (a) Crystal structure and (b) columnar structure of 7CN. *tert*-Butyl group and hydrogen atoms are omitted for clarity.

In terms of **6CN**, it demonstrated structure phase transition at *ca.* 283 K. Transition temperature was also confirmed by DSC measurement (Figure 2-9). Two polymorphs are referred to as high temperature (HT) phase and low temperature (LT) phase. The rapid conversion from HT/LT to LT/HT phases were observed without the break of single crystal, therefore the reflection data of HT/LT phases were collected using the same crystal. The reflection data of HT and LT were obtained at 300 K and 263 K. At 300 K, HT phase of **6CN** belongs to monoclinic crystal system and $I2/a$ space group. HT of **6CN** form 1D columnar structure along c axis derived from weak π - π interaction between cyano group and benzo ring with *ca.* 3.3 Å separation (Figure 2-10). At 263 K, LT phase of **6CN** belongs to triclinic crystal system and $P-1$ space group. The LT phase exhibited twinning, the data was analyzed with *TWINABS* program²³ with volume fraction parameter = 0483. The bond lengths and dihedral angle is similar to that of HT phases, however, the molecular arrangement is slightly changed. Due to the weak π - π interaction, a rotation of the molecules occurred, resulting to form dimer with keeping 1D columnar structure (Figure 2-11). The longitudinal slippage ϕ_1 and latitudinal slippage ϕ_2 are shown in Table 2-3, these slippages are defined according to the literature¹⁵ (Figure 2-12). It insists that there is larger overlap of π -conjugation system in HT phase than that of LT phase.

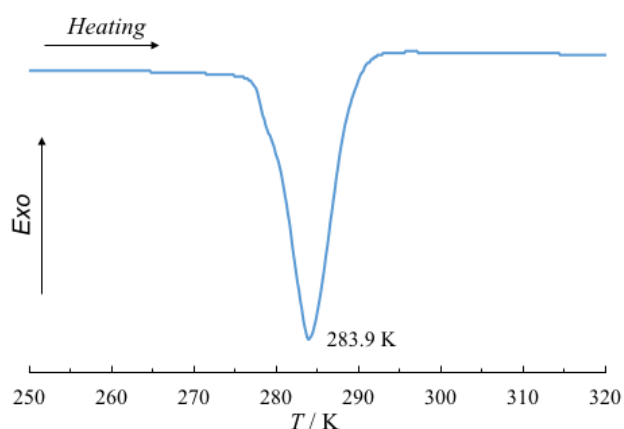


Figure 2-9. DSC measurement of **6CN** (heating rate: 10 K min⁻¹).

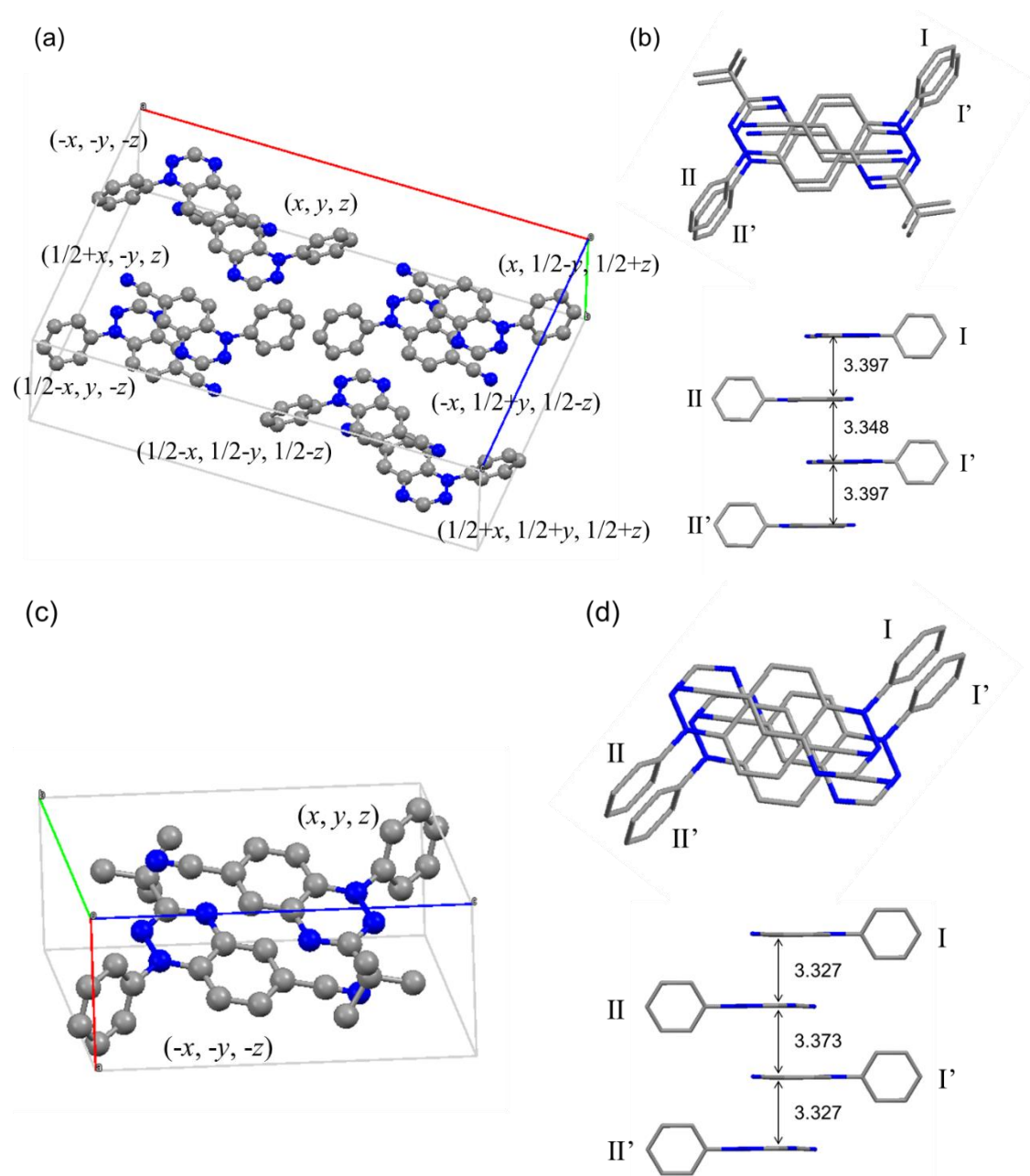


Figure 2-10. (a) Crystal structure and (b) columnar structure of **6CN_HT**. (c) Crystal structure and (d) columnar structure of **6CN_LT**. *tert*-Butyl group and hydrogen atoms are omitted for clarity.

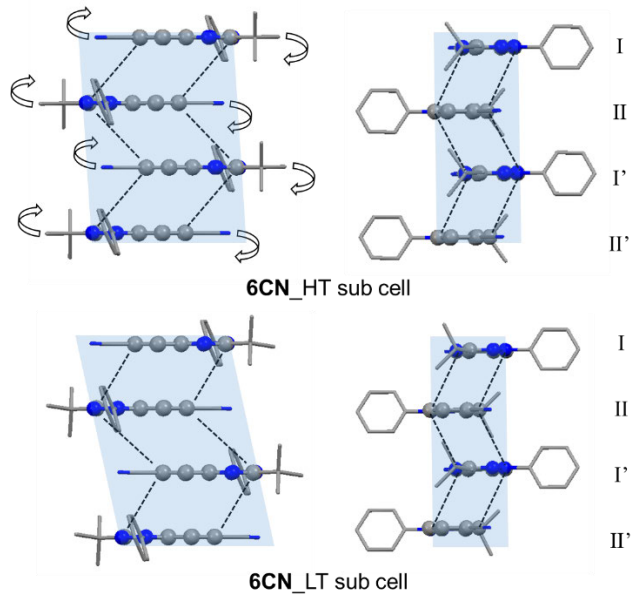


Figure 2-11. Proposed mechanism of structural phase transition for **6CN**.

Table 2-3. The longitudinal and latitudinal slippage of **6CN**.

T / K(phase)	Pair	$\phi_1 / ^\circ$	$\phi_2 / ^\circ$	$d / \text{\AA}$
300 (HT)	I-II	50.8	66.0	3.397
	II-I'	47.2	64.5	3.348
263 (LT)	I-II	57.2	65.2	3.327
	II-I'	43.2	67.1	3.373

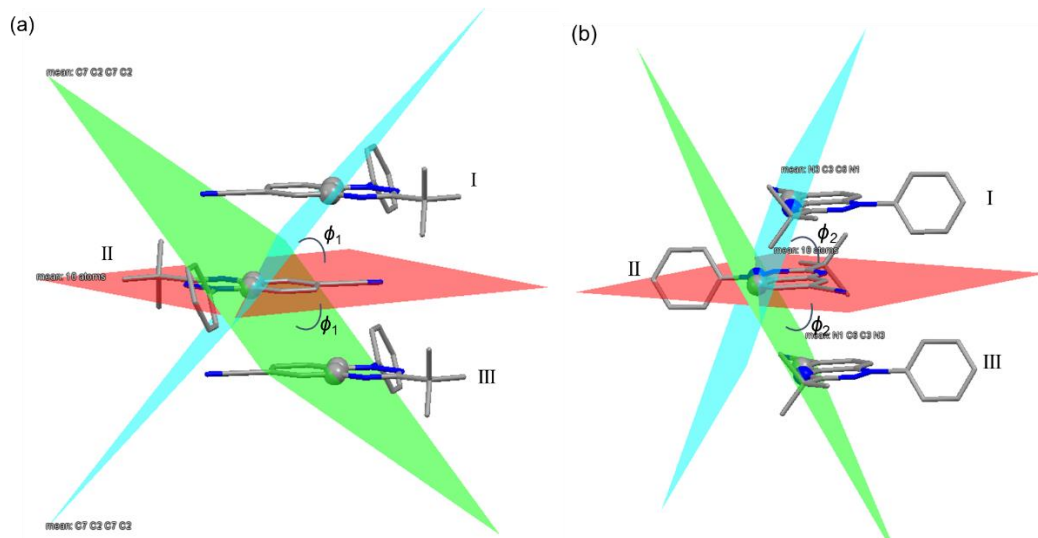


Figure 2-12. The definition of (a) longitudinal slippage ϕ_1 and (b) latitudinal slippage ϕ_2 .

2.4. Magnetic Property

The magnetic susceptibility measurements of polycrystalline samples of benzotriazinyl radical derivatives were carried out using a Quantum Design MPMS-XL SQUID magnetometer. The diamagnetic susceptibility χ_{dia} was estimated by Pacault method²⁴ (**1**: -1.68×10^{-4} emu mol⁻¹, **7CF3**: -1.90×10^{-4} emu mol⁻¹, **7CN** and **6CN**: -1.82×10^{-4} emu mol⁻¹).

The thermal behavior of χ_m for **1** is shown in Figure 2-13. The magnetic susceptibility followed the Curie-Weiss law with $\theta = -3.5$ K, which suggested that antiferromagnetic interaction is dominant in solid state. The $\chi_m T$ value at ambient temperature is 0.389 emu K mol⁻¹, which is slightly larger value than that of isolated doublet spin (0.375 emu K mol⁻¹), and was almost constant above 2.0 K then slightly decreased below 2.0 K. It implied that radical **1** behave as isolated doublet spin in the measured temperature range.

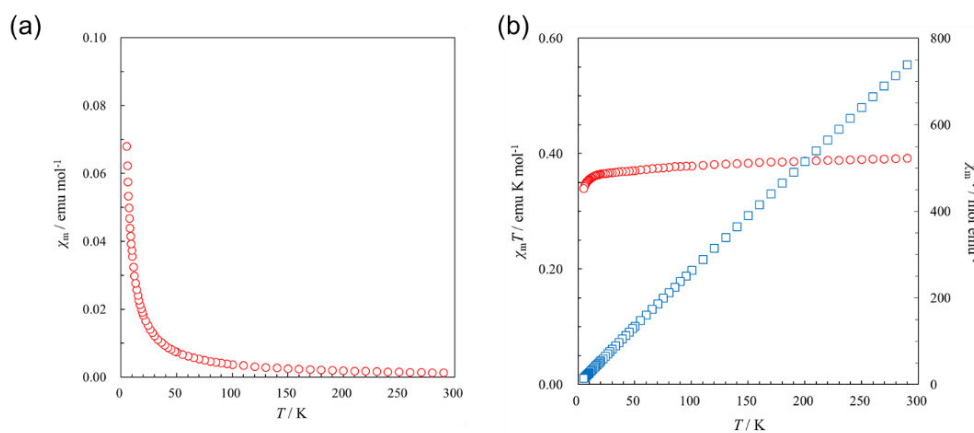


Figure 2-13. The temperature dependence of (a) χ_m and (b) $\chi_m T$ (\circ) and χ_m^{-1} (\square) for **1**.

The thermal behavior of χ_m for **7CF3** is shown in Figure 2-14. The magnetic susceptibility followed the Curie-Weiss law above 50 K with $\theta = +0.7$ K, which suggested that ferromagnetic interaction is dominant in solid state. The $\chi_m T$ value at ambient temperature is 0.374 emu K mol⁻¹, which is close to the value of isolated doublet spin (0.375 emu K mol⁻¹), and was almost constant above 40 K and increased with decreasing temperature, which strongly insisted that ferromagnetic

interaction in polycrystalline sample. Thermal behavior of χ_m can be described using the Heisenberg 1D ferromagnetic chain model and analyzed using approximation equation with $J = +0.63 \text{ cm}^{-1}$. Magnetization measurement was carried out at 1.9 K and 3.0 K. According to the Brillouin function, there is ferromagnetic interaction with $S = 1$ on average along the column of **7CF3** (Figure 2-15).

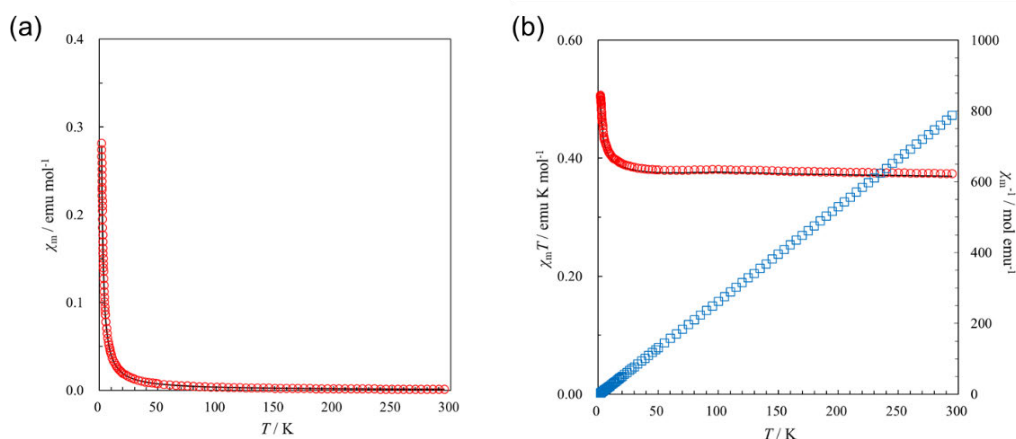


Figure 2-14. The temperature dependence of (a) χ_m and (b) $\chi_m T$ (\circ) and χ_m^{-1} (\square) for **7CF3**. The solid line represented the best-fit result of Heisenberg 1D ferromagnetic chain model. [*New J. Chem.*, **2015**, *39*, 4783] - Reproduced by permission of The Royal Society of Chemistry (RSC) on behalf of the Centre National de la Recherche Scientifique (CNRS) and the RSC.

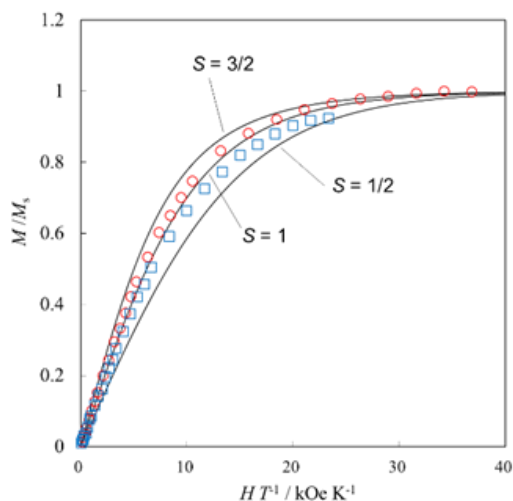


Figure 2-15. Magnetization isotherm of **7CF3** at 1.9 K (\circ) and 3.0 K (\square). The solid lines are the theoretical Brillouin functions for $S = 1/2$, 1, and $3/2$, respectively. [*New J. Chem.*, **2015**, *39*, 4783] - Reproduced by permission of The Royal Society of Chemistry (RSC) on behalf of the Centre National de la Recherche Scientifique (CNRS) and the RSC.

The thermal behavior of χ_m for **7CN** is shown in Figure 2-16. The χ_m value was gradually increased and reached maximal value at 15 K then decreased with decreasing temperature. The $\chi_m T$ value at ambient temperature is 0.388 emu K mol⁻¹, which is slightly larger value than that of isolated doublet spin (0.375 emu K mol⁻¹). This behavior can be well described using the Heisenberg 1D antiferromagnetic chain model taking account with mean field parameter and the best-fit parameters are $J = -15.8$ cm⁻¹ and $\theta = -1.3$ K.

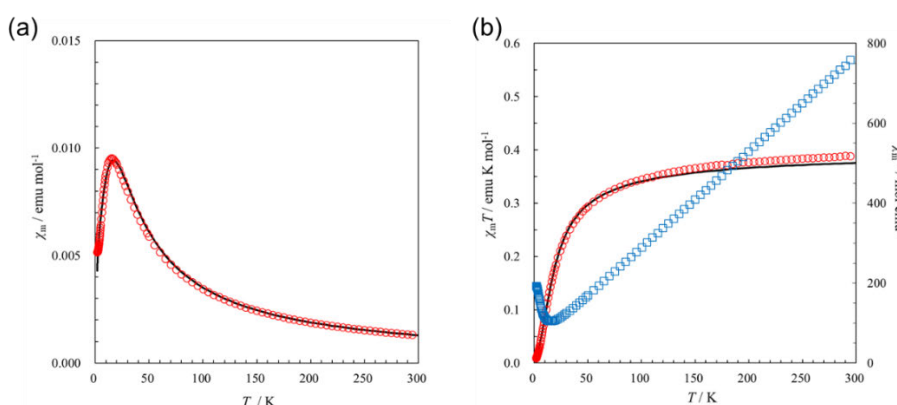


Figure 2-16. The temperature dependence of (a) χ_m and (b) $\chi_m T$ (\circ) and χ_m^{-1} (\square) for **7CN**. The solid line represented the best-fit result of the Heisenberg 1D antiferromagnetic chain model.

The thermal behavior of χ_m for **6CN** is shown in Figure 2-17. The $\chi_m T$ value at 300 K was 0.313 emu K mol⁻¹, which was smaller value than that of the estimated value of isolated $S = 1/2$ spin (0.375 emu K mol⁻¹). It implied the existence of the intermolecular antiferromagnetic interaction. With decreasing temperature, the $\chi_m T$ value was decreased abruptly at 284 K and it is almost plateau below 280 K. In heating process, the thermal behavior of χ_m also abruptly increased at 278 K like cooling process with small hysteresis in the small thermal range. This fully reversible transition was completed in the range of 6 K and was occurred in the corresponding temperature with the structure transition determined from the DSC measurement. The temperature dependence of $\chi_m T$ value in the range of 284-320 K can be described using the Bleaney-Bowers dimer model with $2J = -122.8$ cm⁻¹ and $\theta = -0.71$ K.

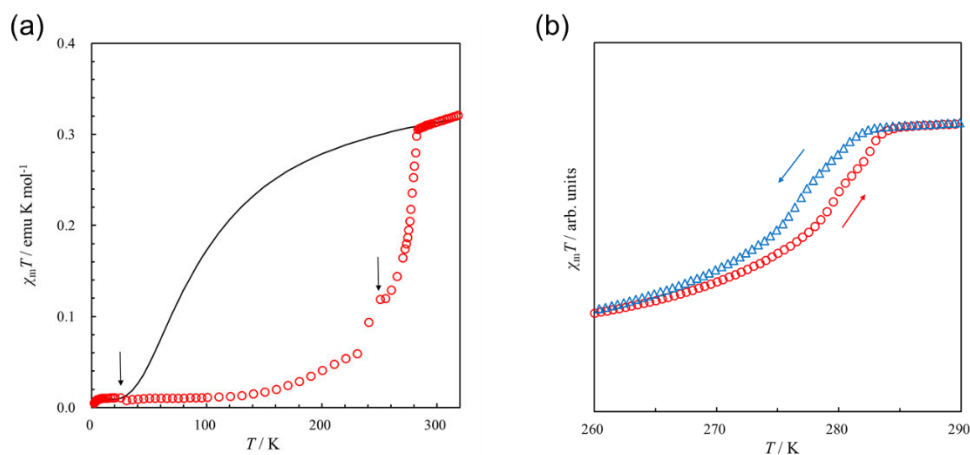


Figure 2-17. The temperature dependence of $\chi_m T$ for **6CN**: (a) Temperature range of 1.8-320 K under the applied field of 50 kOe. Two arrows indicate the temperatures changing sign of observed magnetization in raw data. The solid line represents the best-fit result of the Bleaney-Bowers model in the temperature range of 284-320 K. (b) Temperature range of 260-290 K under the applied field of 50 kOe. Measurement was carried out for the sample wrapped in paramagnetic Al foil to avoid discontinuity as shown in (a). Red circle and blue triangle represent heating and cooling processes, respectively.

2.5. Origin of Magnetic Interaction

2.5.1. DFT Calculation

To estimate the SOMO and spin density distributions, single point calculation using crystallographic coordinate were carried out with DFT calculation at UB3LYP/6-31G(d) level in Gaussian program²⁵.

The SOMO and spin density distribution of **1**, **7CF3**, **7CN** and **6CN** are shown in Figure 2-18 and spin density on π -conjugation system are shown in Table 2-4. SOMO and spin density distribute over the molecule except for *tert*-butyl group. Regarding the phenyl group, the SOMO and spin density distribution depend on the dihedral angle because larger dihedral angle makes phenyl group free from π -conjugated system.

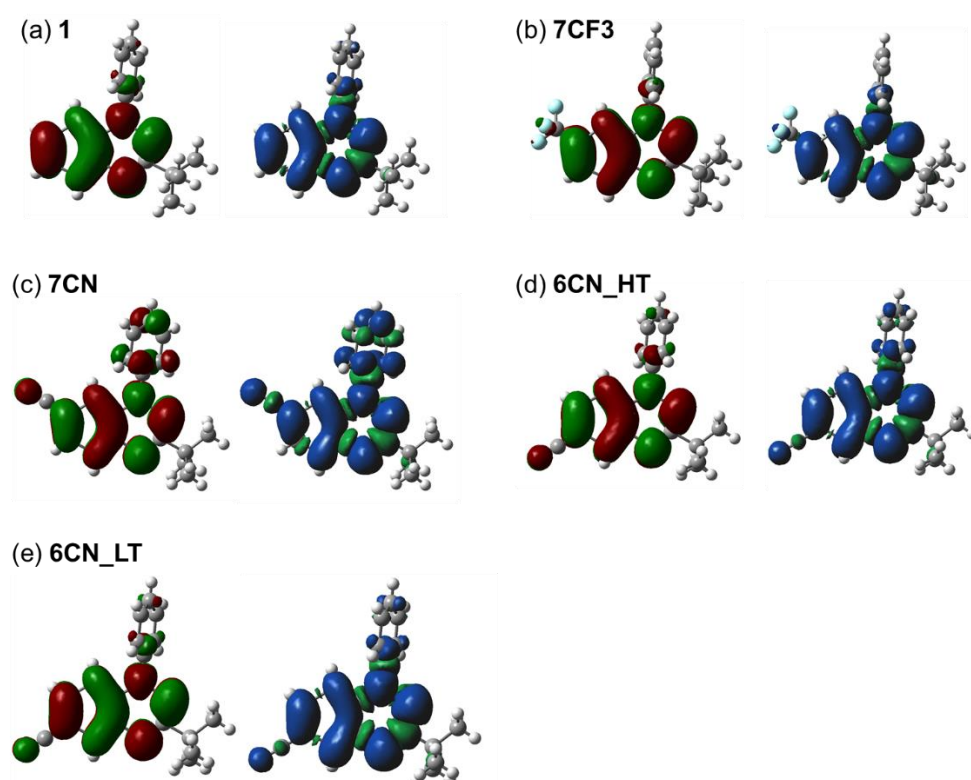


Figure 2-18. SOMO (left) and spin density (right) distributions of 3-*tert*-butyl benzotriazinyl radicals at UB3LYP/6-31G(d) level. [*New J. Chem.*, **2015**, *39*, 4783] - Reproduced by permission of The Royal Society of Chemistry (RSC) on behalf of the Centre National de la Recherche Scientifique (CNRS) and the RSC.

Table 2-4. Selected spin density populations of 3-*tert*-butyl benzotriazinyl radicals at UB3LYP/6-31G(d) level. The labels of atom are shown in Figure 2-5.

Atoms	1	7CF3	7CN	6CN	
				HT (300 K)	LT (263 K)
N1	0.276693	0.283905	0.268135	0.258282	0.259320
N2	0.312905	0.310687	0.277445	0.298421	0.294856
N3	0.314169	0.313087	0.313741	0.330836	0.337312
C1	-0.112259	-0.105888	-0.099088	-0.107663	-0.109259
C2	0.001385	-0.009027	-0.030516	-0.011234	-0.014688
C3	0.058519	0.063385	0.078749	0.092486	0.097946
C4	0.030631	0.022625	-0.006848	0.031249	0.026775
C5	0.070277	0.057495	0.081108	0.050618	0.053232
C6	0.027338	0.054608	0.037634	0.038677	0.038931
C7	0.023651	0.010438	0.028282	0.006886	0.007452
C18	-	0.000312	-0.021213	-0.011144	-0.010190
F1	-	0.002132	-	-	-
F2	-	0.001002	-	-	-
F3	-	0.000333	-	-	-
N4	-	-	0.037546	0.020993	0.019270

2.5.2. Magneto-Structural Correlation Based on Computation

To evaluate effective magnetic coupling of benzotriazinyl radicals, the magnitude of magnetic interaction J of radical pair based on crystal coordinate were estimated using DFT calculation. J values were calculated using equation 2-1 reported by Yamaguchi *et al.*²⁶ E and S^2 represent the total energy and total spin angular momentum, respectively.

$$J = \frac{E_{BS} - E_T}{\langle S^2 \rangle_T - \langle S^2 \rangle_{BS}} \quad (\text{eq. 2-1})$$

For radical **1**, there is negligible magnetic interaction according to the magnetic susceptibility measurement. The radical pair in columnar structure shown in Figure 2-19, *tert*-butyl group is contact with π -conjugation system. Due to the very small spin density population on *tert*-butyl group, the J value is almost zero. The computational result is consistent with the experimental result (Table 2-5).

Table 2-5. Calculation result of **1**.

Function / Basis Set	Energy(BS/T) / a.u.	$\langle S^2 \rangle$ (BS/T)	J / cm^{-1}
UB3LYP/6-31G(d)	-1645.3732996 / -1645.3732997	1.026936 / 2.026934	+0.02

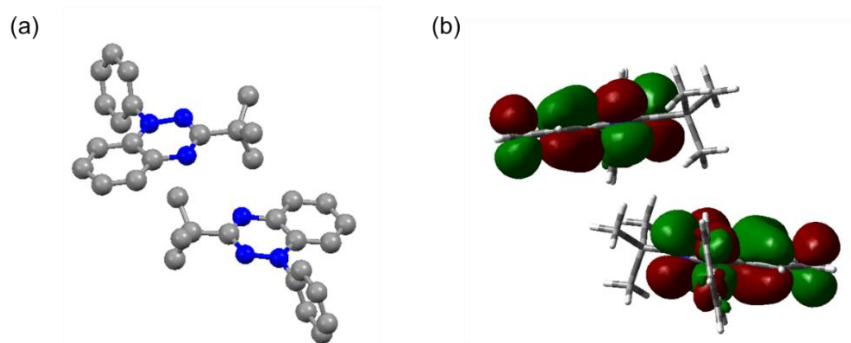


Figure 2-19. (a) Molecular contact and (b) the contact of SOMOs of **1** within the column. Hydrogen atoms are omitted for clarity.

For radical **7CF3**, there is ferromagnetic interaction in the column with $J = +0.63 \text{ cm}^{-1}$ according to the magnetic susceptibility measurement. The radical pair in columnar structure is shown in Figure 2-20, π -conjugation systems are contacted with reduced overlap of SOMO, which suggest the

reduction of overlap integral. Due to the long distance between π -conjugation systems, smaller J value was estimated in experiment. The J value of computation is $+0.42 \text{ cm}^{-1}$, which is consistent with the experimental result (Table 2-6).

Table 2-6. Calculation result of **7CF3**.

Function / Basis Set	Energy(BS/T) / a.u.	$\langle S^2 \rangle$ (BS/T)	J / cm^{-1}
UB3LYP/6-31G(d)	-2319.1453862 / -2319.1453881	1.026865 / 2.02689	+0.42

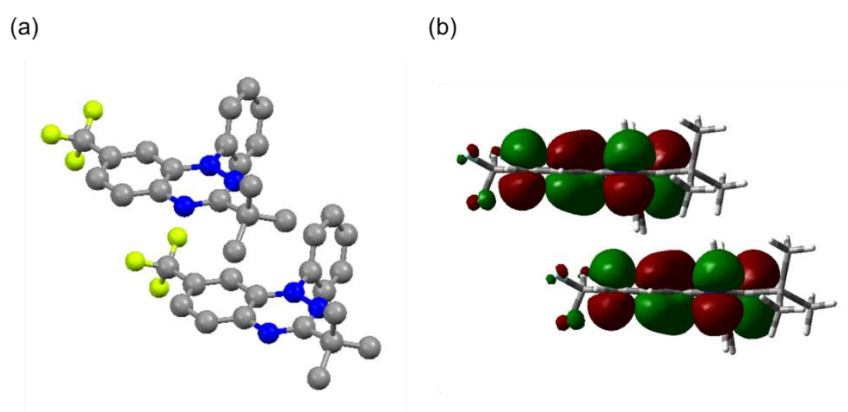


Figure 2-20. (a) Molecular contact and (b) the contact of SOMOs of **7CF3** within the column. Hydrogen atoms are omitted for clarity. [*New J. Chem.*, **2015**, 39, 4783] - Reproduced by permission of The Royal Society of Chemistry (RSC) on behalf of the Centre National de la Recherche Scientifique (CNRS) and the RSC.

For radical **7CN**, there is antiferromagnetic interaction in the column with $J = -16.5 \text{ cm}^{-1}$ according to the magnetic susceptibility measurement. Regarding the contact in the column, there is large overlap of SOMO, leading antiferromagnetic interaction (Figure 2-21). The computation was carried out using both UB3LYP and UBLYP function. The estimated J values of both function were negative, implying the existence of antiferromagnetic coupling in the radical pair, which is consistent with the experimental result. The computational value at UBLYP/6-31G(d) level was reproduced experimental value; antiferromagnetic one-dimensional column with the existence of weak intercolumnar antiferromagnetic interaction (Table 2-7).

Table 2-7. Calculation result of 7CN.

Pair	Function / Basis Set	Energy(<i>BS/T</i>) / a.u.	$\langle S^2 \rangle$ (<i>BS/T</i>)	<i>J</i> / cm ⁻¹
Pair A	UB3LYP/6-31G(d)	-1829.6052263 / -1829.6052110	1.027120 / 2.027955	-3.4
	UBLYP / 6-31G(d)	-1828.7856173 / -1828.7855779	1.003589 / 2.008456	-8.7
Pair B	UB3LYP/6-31G(d)	-1829.6155189 / -1829.6155196	1.027472 / 2.027491	+0.2
	UBLYP / 6-31G(d)	-1828.7979382 / -1828.7979380	1.008204 / 2.008332	-0.04
Pair C	UB3LYP/6-31G(d)	-1829.6079463 / -1829.6079461	1.027894 / 2.027898	-0.04
	UBLYP / 6-31G(d)	-1828.7908988 / -1828.7908983	1.008365 / 2.008430	-0.11

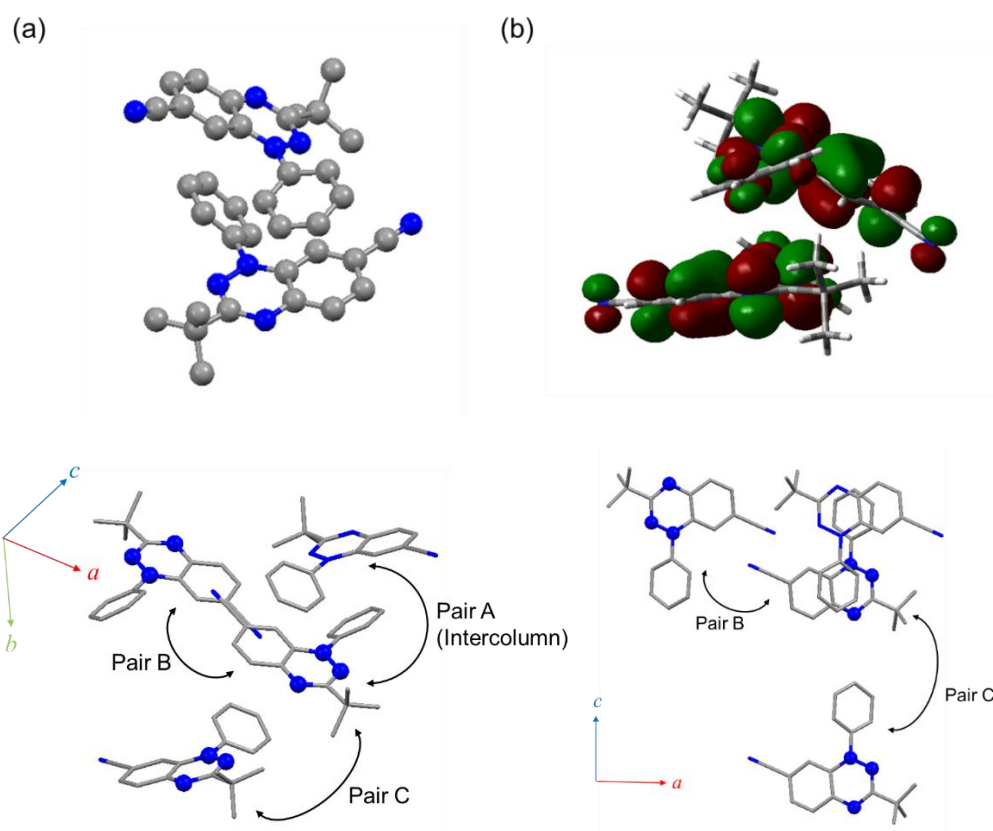


Figure 2-21. (a) Molecular contact and (b) the contact between SOMOs of 7CN in the column (Hydrogen atoms are omitted for clarity).

For radical **6CN**, two kinds of contacts were observed in both HT and LT phases (Figure 2-22). In HT phase, the negative $2J$ value at UBLYP/6-31G(d) level indicated the existence of intermolecular magnetic interaction, which is consistent with the magnetic susceptibility measurement (Table 2-8). In LT phase, the overlap of SOMOs are significantly changed compared to that of HT phase and interaction between the SOMOs are enhanced, leading strong antiferromagnetic interaction and abrupt decrease of magnetic susceptibility in experiment. The estimated $2J$ values of both functions were negative, implying antiferromagnetic interaction. The computation at UBLYP/6-31G(d) level well reproduced the intermolecular magnetic interaction of both HT and LT phases.

Table 2-8. Calculation result of **6CN**.

Pair(Phase)	Function / Basis Set	Energy(BS/T) / a.u.	$\langle S^2 \rangle$ (BS/T)	$2J / \text{cm}^{-1}$
Pair I-II (HT)	UB3LYP/6-31G(d)	-1829.5998682 / -1829.5998784	1.025442 / 2.027256	+4.5
	UBLYP / 6-31G(d)	-1828.7783900 / -1828.7782979	0.996173 / 2.008510	-40.9
Pair I-II (LT)	UB3LYP/6-31G(d)	-1829.6097942 / -1829.6085162	0.980403 / 2.027684	-587.5
	UBLYP / 6-31G(d)	-1828.7934835 / -1828.7906151	0.737716 / 2.008629	-1600
Pair II-I' (HT)	UB3LYP/6-31G(d)	-1829.5974589 / -1829.5974837	1.026153 / 2.027356	+10.9
	UBLYP / 6-31G(d)	-1828.7760002 / -1828.7759894	1.003631 / 2.008553	-4.8
Pair II-I' (LT)	UB3LYP/6-31G(d)	-1829.6107765 / -1829.6104445	1.025442 / 2.027256	-147.5
	UBLYP / 6-31G(d)	-1828.7940379 / -1828.7932765	0.934801 / 2.008723	-358.9

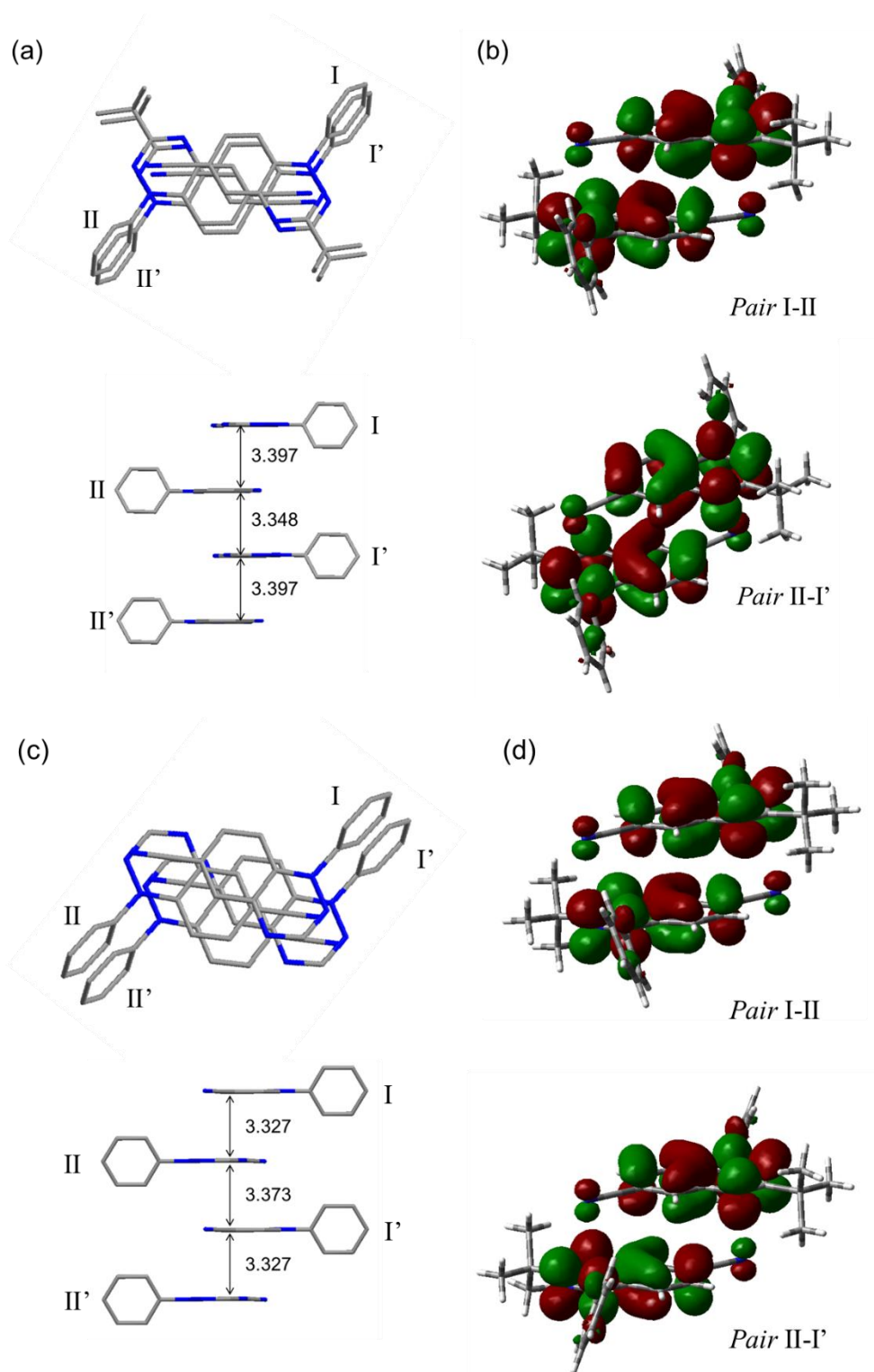


Figure 2-22. Molecular contact and the contact between SOMOs of 6CN (a, b: HT phase, c, d: LT phase) within the column. Hydrogen atoms are omitted for clarity.

2.6. ESR Measurement

The ESR spectra of **1**, **7CF3**, **7CN** and **6CN** in toluene at room temperature are shown in Figure 2-23. All spectra exhibited complex patterns arising from non-equivalent nitrogen nuclei, hydrogen nuclei and functional group. The hyperfine coupling constants (hfcc) were estimated using *Winsim* program²⁷ and were assigned according to the ENDOR measurement^{20b}. The result of assignment (Table 2-9) suggested that spin density delocalizes over the molecule except for *tert*-butyl group, which is accordance with the computational result. Comparing the hfccs of nitrogen nuclei on amidrazonyl ring, a_{N2} and a_{N3} of 7-substituted radicals were decreased, whereas the decrease of a_{N1} in 6-substituted radical. It revealed that functional group contribute to the delocalization of unpaired electron and mainly affect to the spin density of nitrogen for the *para*-position of the substituent.

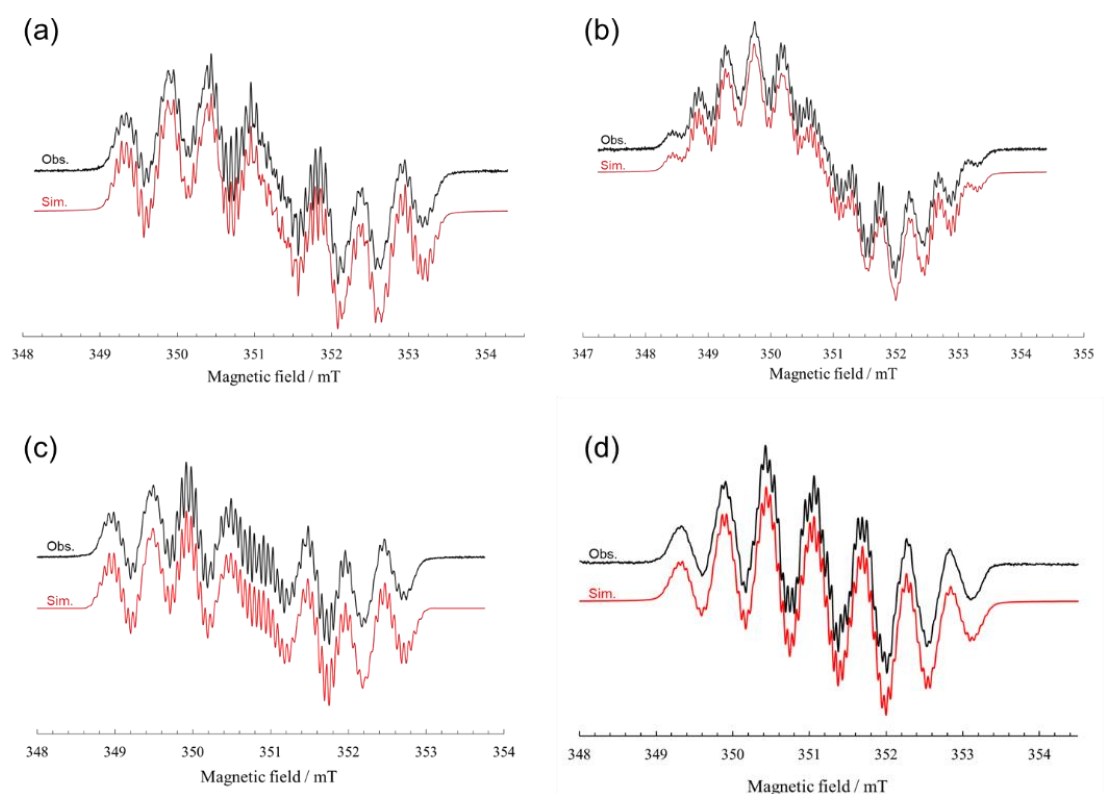
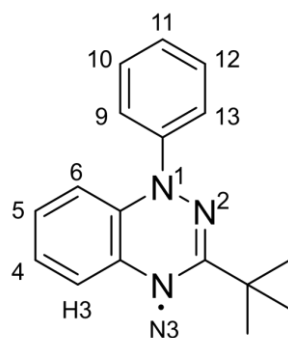


Figure 2-23. ESR spectra of (a) **1** (b) **7CF3** (c) **7CN** and (d) **6CN** in toluene at room temperature. [*New J. Chem.*, **2015**, *39*, 4783] - Reproduced by permission of The Royal Society of Chemistry (RSC) on behalf of the Centre National de la Recherche Scientifique (CNRS) and the RSC.

Table 2-9. The hfccs of 3-*tert*-butyl benzotriazinyl radicals.

nuclei	hfcc / mT			
	1	7CF3	7CN	6CN
N1	0.742	0.749	0.752	0.687
N2	0.486	0.477	0.462	0.516
N3	0.516	0.506	0.495	0.517
CF ₃	-	0.358		
CN	-	-	0.113	0.800
H3	0.141	0.167	0.125	0.120
H4	0.107	0.117	0.117	-
H5	0.190	-	-	0.169
H6	0.080	0.072	0.113	0.101
H9,13	0.077	0.070	0.061	0.066
H10, 12	0.052	0.057	0.060	0.053
H11	0.066	0.065	0.061	0.048
<i>g</i> -factor	2.0039	2.0042	2.0039	2.0040



References in Chapter 2

- (a) P. M. Allemand, G. Srdanov, F. Wudl, *J. Am. Chem. Soc.*, **1990**, *112*, 9391.
 - (b) M. Yao, S. Asakura, M. Abe, H. Inoue, N. Yoshioka, *Cryst. Growth Des.*, **2005**, *5*, 413.
 - (c) M. Yao, H. Inoue, N. Yoshioka, *Chem. Phys. Lett.*, **2005**, *402*, 11.
 - (d) N. Yoshioka, in *Advances in Organic Crystal Chemistry*, ch. 34 (Eds. R. Tamura, M. Miyata), Springer Japan, Tokyo, Japan, 2015,
- R. Kuhn, H. Trischmann, *Angew. Chem. Int. Ed. Engl.*, **1963**, *2*, 155.
- (a) M. Jasiński, J. S. Gerding, A. Jankowiak, K. ębicki, J. Romański, K. Jastrzębska, A. Sivaramamoorthy, K. Mason, D. H. Evans, M. Celeda, P. Kaszyński, *J. Org. Chem.*, **2013**, *78*, 7445.
 - (b) T. N. Le, T. Trevisan, E. Lieu, D. J. R. Brook, *Eur. J. Org. Chem.*, **2017**, *7*, 1125.
- F. A. Neugebauer, *Angew. Chem. Int. Ed.*, **1973**, *12*, 455.
- R. G. Hicks, in *Stable Radicals: Fundamentals and Applied Aspects of Odd-Electron Compounds*, ch. 7 (Eds. R. G. Hicks), Wiley, Chichester, UK, **2010**
- (a) K. Mukai, N. Wada, J. B. Jamali, N. Achiwa, Y. Narumi, K. Kindo, T. Kobayashi, K. Amaya, *Chem. Phys. Lett.*, *1996*, *257*, 538.
 - (b) K. Mukai, Y. Shimobe, T. Hamamoto, K. Kindo, *Physica B*, **2000**, *284-288*, 1647.
- (a) A. Jankowiak, D. Pocięcha, H. Monobe, J. Szczytko, Ź. Dębska, J. Romański, P. Kaszyński, *Phosphorus Sulfur Relat. Elem.*, **2013**, *188*, 418.
 - (b) P. Kaszyński, M. Jasiński, S. Ciastek, S. Kapuscinski, K. Gebicki, *ARKIVOC*, **2017**, *2*, 345.
- H. M. Blatter, H. Lukaszewski, *Tetrahedron Lett.*, **1968**, *9*, 2701.
- P. A. Koutentis, D. Lo Re, *Synthesis*, **2010**, *12*, 2075.
- (a) A. A. Berezin, G. Zissimou, C. P. Constantinides, Y. Beldjoudi, J. M. Rawson, P. A. Koutentis, *J. Org. Chem.*, **2014**, *79*, 314.
 - (b) C. P. Constantinides, E. Obijalska, P. Kaszyński, *Org. Lett.*, **2016**, *18*, 916.
 - (c) J. A. Grant, Z. Lu, D. E. Tucker, B. M. Hockin., D. S. Yufit, M. A. Fox, R. Katakya, V. Chechik, A. C. O'Donoghue, *Nat. Commun.*, **2017**, *8*, 15088.
 - (d) A. C. Savva, S. I. Mirallai, G. A. Zissimou, A. A. Berezin, M. Demetriades, A. Kourtellaris, C. P. Constantinides, C. Nicolaidis, T. Trypiniotis, P. A. Koutentis, *J. Org. Chem.*, **2017**, *82*, 7564.
- (a) C. P. Constantinides, P. A. Koutentis, G. Loizou, *Org. Biomol. Chem.*, **2011**, *9*, 3122.
 - (b) Y. Takahashi, Y. Miura, N. Yoshioka, *Chem. Lett.*, **2014**, *43*, 1236.
 - (c) A. Bodzioch, M. Zheng, P. Kaszyński, G. Utecht, *J. Org. Chem.*, **2014**, *79*, 7294.
- (a) M. Fumanal, S. Vela, J. Ribas-arinõ, J. J. Novoa, *Chem. –Asian J.*, **2014**, *9*, 3612.
 - (b) M. Fumanal, S. Vela, J. J. Novoa, J. Ribas-Arino, *Chem. Commun.*, **2015**, *51*, 15776.
- F. A. Neugebauer, I. Umminger, *Chem. Ber.*, **1980**, *113*, 1205.
- C. P. Constantinides, E. Carter, D. M. Murphy, M. Manoli, G. M. Leitius, M. Bendikov, J. M.

- Rawson, P. A. Koutentis, *Chem. Commun.*, **2013**, 49, 8662.
15. C. P. Constantinides, A. A. Berezin, G. A. Zissimou, M. Manoli, G. M. Leitus, M. Bendikov, M. R. Probert, J. M. Rawson, P. A. Koutentis, *J. Am. Chem. Soc.*, **2014**, 136, 11906.
16. (a) I. S. Morgan, A. Peuronen, M. M. Hänninen, R. W. Reed, R. Clérac, H. M. Tuononen, *Inorg. Chem.* **2014**, 53, 33.
(b) I. S. Morgan, A. Mansikkamäki, G. A. Zissimou, P. A. Koutentis, M. Rouzières, R. Clérac, H. M. Tuononen, *Chem. Eur. J.* **2015**, 21, 15843.
(c) I. S. Morgan, A. Mansikkamäki, M. Rouzières, R. Clérac, H. M. Tuononen, *Dalton Trans.* **2017**, 46, 12790.
17. B. Yan, J. Cramer, R. McDonald, N. L. Frank, *Chem. Commun.*, **2011**, 47, 3201.
18. K. A. Hutchison, K. Hasharoni, F. Wudl, A. Berg, Z. Shuali, H. Levanon, *J. Am. Chem. Soc.*, **1998**, 120, 6362.
19. P. Kaszyński, C. P. Constantinides, V. G. Young Jr., *Angew. Chem. Int. Ed.*, **2016**, 55, 11149.
20. (a) F. A. Neugebauer, I. Umminger, *Chem. Ber.*, **1981**, 114, 2423.
(b) F. A. Neugebauer, G. Rimmler, *Magn. Reson. Chem.*, **1988**, 26, 595.
21. K. Mukai, K. Inoue, N. Achiwa, J. B. Jamali, C. Krieger, F. A. Neugebauer, *Chem. Phys. Lett.*, **1994**, 224, 569.
22. X. Xiong, Y. Jiang, D. Ma, *Org. Lett.*, **2012**, 14, 2552.
23. Bruker, *TWINABS Ver. 2012/1*, Bruker AXS Inc., Madison, Wisconsin, USA, 2001.
24. R. Gupta, in *Landolt-Börnstein New Series Group II* (Eds. K. -H. Hellwege and A. M. Hellwege), Springer, Berlin, Germany, 1986, Vol. 16, ch. 1.2.
25. Gaussian 03: Revision B.04, M. J. Frisch, G. W. Trucks, H. B. Schlegel, G. E. Scuseria, M. A. Robb, J. R. Cheeseman, J. A. Montgomery Jr., T. Vreven, K. N. Kudin, J. C. Burant, J. M. Millam, S. S. Iyengar, J. Tomasi, V. Barone, B. Mennucci, M. Cossi, G. Scalmani, N. Rega, G. A. Petersson, H. Nakatsuji, M. Hada, M. Ehara, K. Toyota, R. Fukuda, J. Hasegawa, M. Ishida, T. Nakajima, Y. Honda, O. Kitao, H. Nakai, M. Klene, X. Li, J. E. Knox, H. P. Hratchian, J. B. Cross, C. Adamo, J. Jaramillo, R. Gomperts, R. E. Stratmann, O. Yazyev, A. J. Austin, R. Cammi, C. Pomelli, J. W. Ochterski, P. Y. Ayala, K. Morokuma, G. A. Voth, P. Salvador, J. J. Dannenberg, V. G. Zakrzewski, S. Dapprich, A. D. Daniels, M. C. Strain, O. Farkas, D. K. Malick, A. D. Rabuck, K. Raghavachari, J. B. Foresman, J. V. Ortiz, Q. Cui, A. G. Baboul, S. Clifford, J. Cioslowski, B. B. Stefanov, G. Liu, A. Liashenko, P. Piskorz, I. Komaromi, R. L. Martin, D. J. Fox, T. Keith, M. A. Al-Laham, C. Y. Peng, A. Nanayakkara, M. Challacombe, P. M. W. Gill, B. Johnson, W. Chen, M. W. Wong, C. Gonzalez, J. A. Pople, Gaussian, Inc, Pittsburgh PA, 2003.
- Gaussian 09: Revision D.01, M. J. Frisch, G. W. Trucks, H. B. Schlegel, G. E. Scuseria, M. A. Robb, J. R. Cheeseman, G. Scalmani, V. Barone, B. Mennucci, G. A. Petersson, H. Nakatsuji, M. Caricato, X. Li, H. P. Hratchian, A. F. Izmaylov, J. Bloino, G. Zheng, J. L. Sonnenberg, M. Hada,

- M. Ehara, K. Toyota, R. Fukuda, J. Hasegawa, M. Ishida, T. Nakajima, Y. Honda, O. Kitao, H. Nakai, T. Vreven, J. A. Montgomery, Jr., J. E. Peralta, F. Ogliaro, M. Bearpark, J. J. Heyd, E. Brothers, K. N. Kudin, V. N. Staroverov, R. Kobayashi, J. Normand, K. Raghavachari, A. Rendell, J. C. Burant, S. S. Iyengar, J. Tomasi, M. Cossi, N. Rega, J. M. Millam, M. Klene, J. E. Knox, J. B. Cross, V. Bakken, C. Adamo, J. Jaramillo, R. Gomperts, R. E. Stratmann, O. Yazyev, A. J. Austin, R. Cammi, C. Pomelli, J. W. Ochterski, R. L. Martin, K. Morokuma, V. G. Zakrzewski, G. A. Voth, P. Salvador, J. J. Dannenberg, S. Dapprich, A. D. Daniels, Ö. Farkas, J. B. Foresman, J. V. Ortiz, J. Cioslowski, D. J. Fox, Gaussian, Inc., Wallingford CT, 2009.
26. K. Yamaguchi, H. Fukui, T. Fueno, *Chem. Lett.*, **1986**, 625.
27. D. A. O'Brien, D. R. Duling, Y. C. Fann, *Public EPR Software Tools: Winsim Spectral Simulation for MS- Windows 9x, NT v0.98*, NIEHS, National Institute of Health, Bethesda, MD.

Chapter 3: Magneto-Structural Correlation in Nitroxyl-Triazinyl Hetero Biradicals

3.1. Introduction

Nitroxide radical is a kind of localized radical and widely recognized in the various fields not only molecule-based magnet but also redox active component of polymer rechargeable battery,¹ spin probe in biological study,² radical-mediated polymerization³ and co-catalyst of oxidation in organic synthesis.⁴ Since the first nitroxide was reported,⁵ a lot of radical derivatives have been reported and they are classified in two kinds, aliphatic and aryl nitroxides. The molecular structure of pyrroline *N*-oxyl, which is well known aliphatic nitroxides, is shown in Figure 3-1. The unpaired electron localizes on nitroxyl group and it extends to adjacent methyl groups, which may be attributed to hyperconjugation of π^* -orbital of nitroxyl group.⁶ On the other hand, aryl nitroxides have been also investigated and their unpaired electron distributes not only nitroxyl moiety but also aryl groups attached to nitrogen atom of nitroxyl moiety (Figure 3-2). However, high population of unpaired electron at *para*-position of nitroxyl group cause disproportionation. In general, functional group is introduced at *para*-position to stabilize radical.

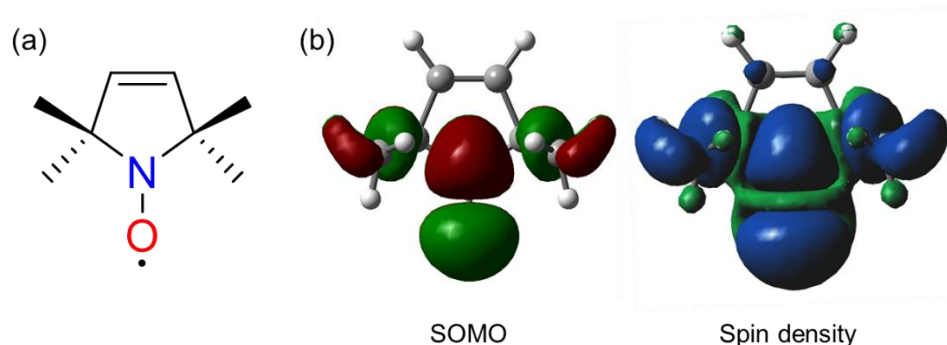


Figure 3-1. (a) Molecular structure and (b) SOMO (isovalue 0.02) and spin density (isovalue 0.00013) distribution of pyrroline *N*-oxyl. [*ChemPhysChem*, **2018**, *19*, 175.] - Copyright 2018, Wiley-VCH Verlag GmbH and Co. KGaA. Reproduced with permission.

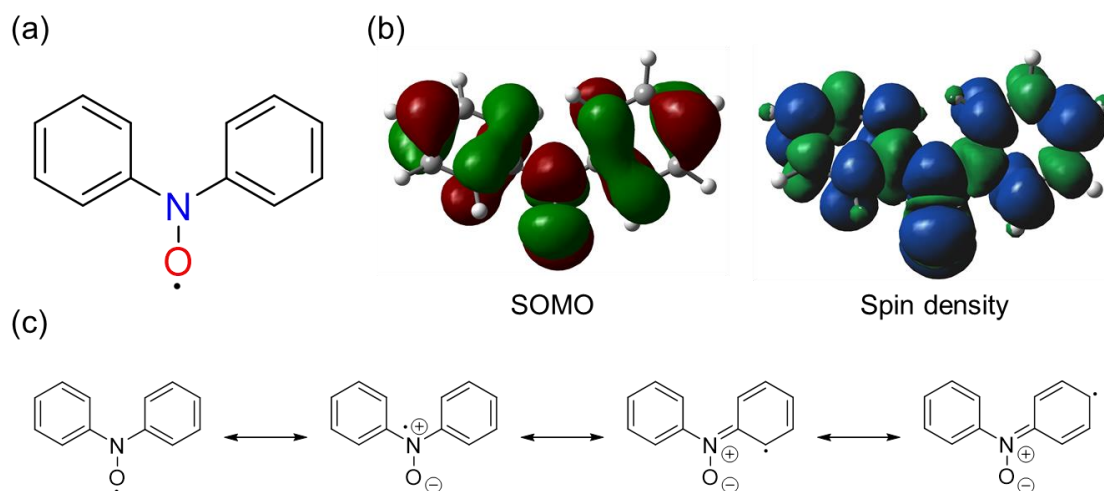


Figure 3-2. (a) Chemical structure, (b) SOMO and spin density distribution, and (c) the resonance structure of diphenyl nitroxide radical.

Thanks to the high stability, transformation of functional group on aliphatic nitroxide can be proceeded without the protection of radical moiety⁷ including organometallic reaction such as Suzuki-Miyaura⁸ coupling and Sonogashira⁹ coupling, whereas other radicals have to protect their spin site. The electronic state of aryl nitroxide can be controlled by introducing substituents to aromatic ring.

In the meantime, construction of radical polymer for magnetic material is still challenging. To exhibit strong magnetic interaction, the methodologies of controlling magnetic interaction have been discussed using π -conjugated biradical, as shown in chapter 1. Actually, radical polymers exhibiting ferromagnetic interaction with $S > 5000$ have been reported,¹⁰ however, their intramolecular magnetic interaction is weakened due to the lack of unpaired electron derived from decomposition and disproportionation (Figure 3-3(a)). In consequence, it is difficult to increase the magnetic transition temperature and spin concentration. On the other hand, Tyutyulkov *et al.* proposed the magnetic interaction mechanism between localized partially occupied molecular orbital (LPOMO) for the polyradical.¹¹ They suggested that the spin centers having LPOMO interact each other through fulfilled π -orbital like superexchange interaction (Figure 3-3(b)). From this theory, organic radicals having localized SOMO can be candidate for spin center of LPOMO.

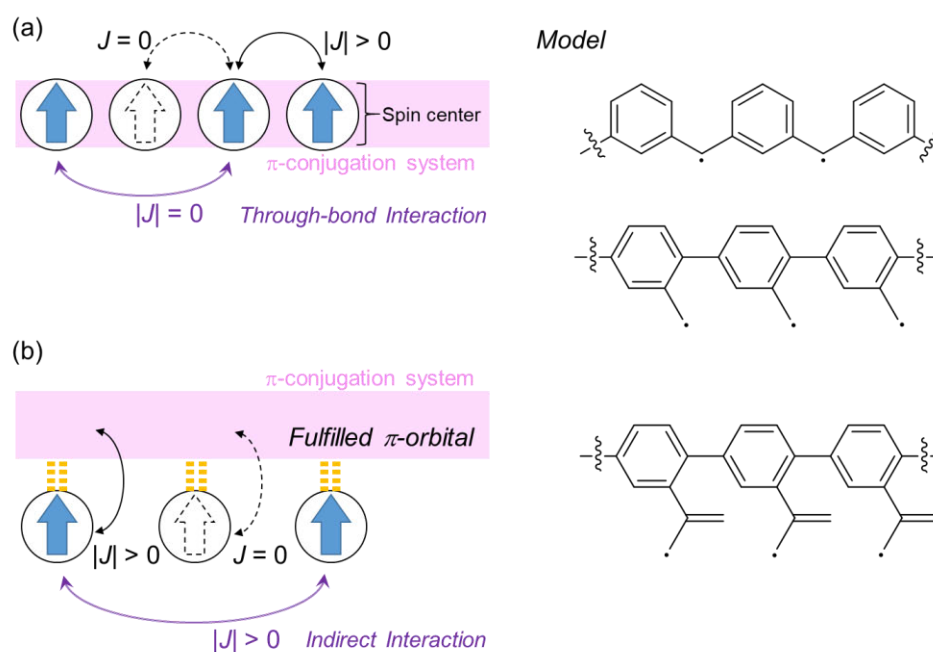


Figure 3-3. Schematic illustrations and molecular structure of model polymer for (a) direct (Through-bond) interaction and (b) indirect (superexchange-like) interaction.

Aliphatic nitroxide like **TEMPO** usually have not been utilized for spin center due to their high localization nature of unpaired electron. Therefore, localized nitroxide have been studied for spin probe as well as co-catalyst for oxidation. Regarding the spin density of tetramethylisindoline *N*-oxyl (**TMIO**), which benzo ring-fused pyrroline *N*-oxyl, there is weak but not negligible spin density on the benzo ring estimated by the spectroscopic study,¹² implying that cyclic nitroxide can be promising candidate for spin center of LPOMO. Regarding the magnitude of magnetic interaction, the interaction through π -conjugation system is stronger than that of through non-conjugated framework due to the spin polarization effect. Because of the weak magnetic interaction, the methodology of controlling interaction through non-conjugated framework has not been discussed well. However, the stability of cyclic nitroxide derivatives may contribute to improve the stability of polyradical. In the point of these view, it is important to investigate the magnetic interaction through non-conjugated framework.

In chapter 3, pyrroline *N*-oxyl fused benzotriazinyl radicals **3PPO** and **3BPO**, whose benzo ring is shared with **TMIO** and benzotriazinyl radical, are designed (Figure 3-4). As shown in chapter 2,

spin density of benzotriazinyl radicals distributes on benzo ring and positive spins are populated on carbon atoms at 6 and 7 positions. There is few report of magneto-structural correlation in biradicals composed of localized and delocalized radicals. In terms of spin arrangement, the spins of nitroxide site and benzotriazinyl radical site are parallelly aligned, which insisted ferromagnetic coupling through non-conjugated framework and ground triplet state will be predicted (Figure 3-5).

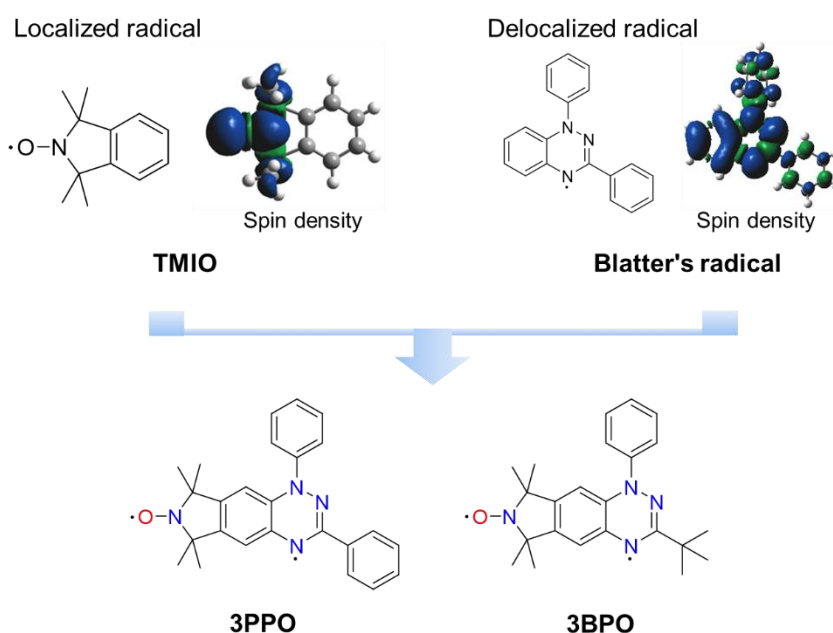


Figure 3-4. Molecular structure of **TMIO**, Blatter's radical and pyrroline *N*-oxyl fused benzotriazinyl radicals.

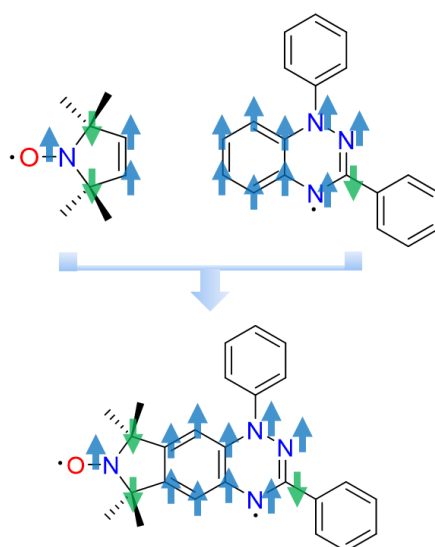
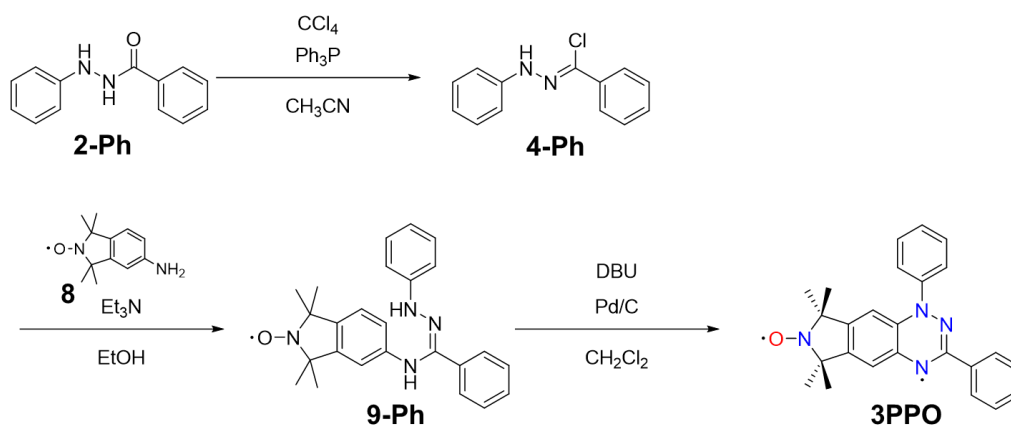


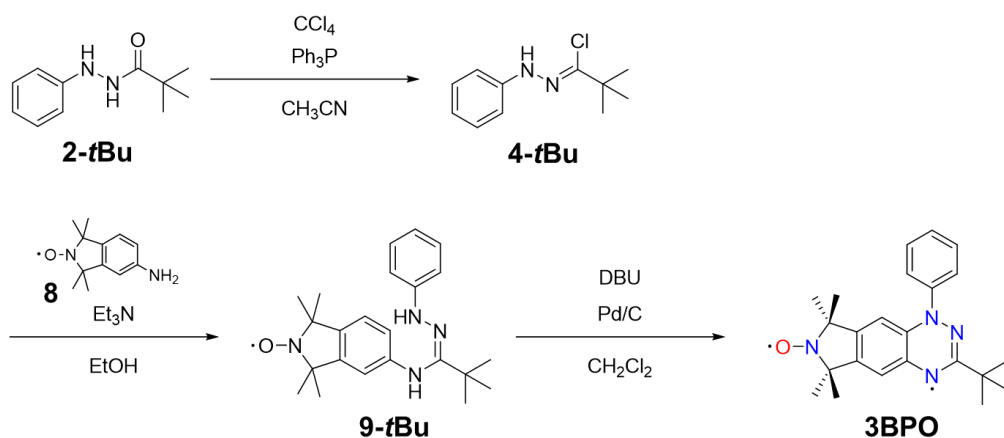
Figure 3-5. Predicted spin alignment of **3PPO**.

3.2. Synthesis

Pyrroline *N*-oxyl fused benzotriazinyl radicals **3PPO** and **3BPO** were synthesized according to Schemes 3-1 and 3-2. Hydrazide **2-Ph** and **2-*t*Bu** were obtained by condensation of phenylhydrazine and benzoyl chloride or pivaloyl chloride. After chlorination of **2**, condensation between **4** and **8** gave radical precursors **9-Ph** and **9-*t*Bu** with moderate yield. Oxidative cyclization was proceeded under the presence of DBU and catalytic amount of Pd/C to afford **3PPO** and **3BPO**. Amino-substituted **TMIO** radical **6** was prepared from phthalic anhydride via several steps in the same manner according to the literature.¹³



Scheme 3-1. Synthetic route of **3PPO**.



Scheme 3-2. Synthetic route of **3BPO**.

3.3. Crystallographic Analysis

Single crystals of **3PPO** and **3BPO** suitable for X-ray analysis were obtained by slow evaporation in mix solvent of CH_2Cl_2 / *n*-hexane. The ORTEP drawings are shown in Figure 3-6 and selected bond lengths and dihedral angle between phenyl ring and amidorazonyl ring are shown in Table 3-1. Crystallographic data are shown in Table 3-2. The bond lengths of π -conjugation system are similar values and suggested delocalization of unpaired electron of benzotriazinyl site. The bond lengths of nitroxide are typical of **TMIO** radicals. The π -conjugation system of **3PPO** is slightly twisted due to the packing effect, whereas planar structure of five-membered ring on **3BPO**.

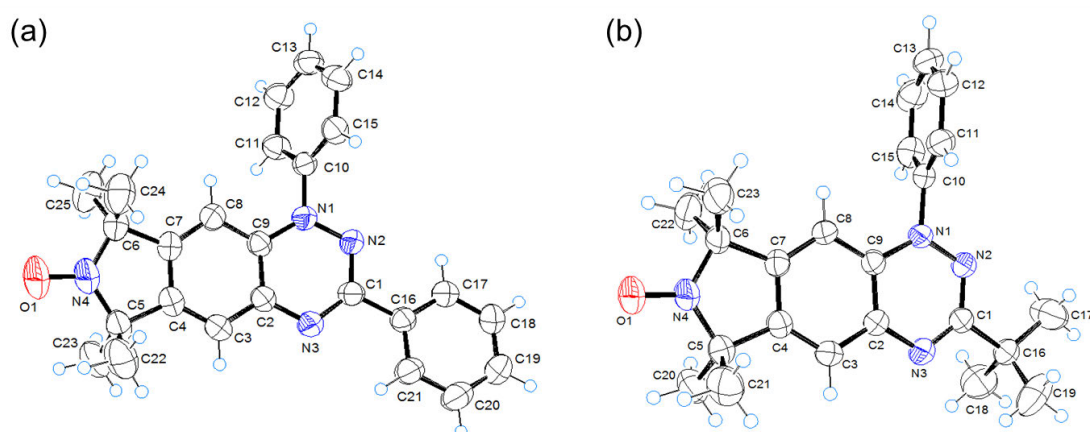


Figure 3-6. ORTEP drawings of (a) **3PPO** and (b) **3BPO** with 50% thermal ellipsoids.

Table 3-1. Selected bond lengths and dihedral angle of **3PPO** and **3BPO**.

Compound	3PPO	3BPO
$d_{\text{N1-N2}} / \text{\AA}$	1.373(2)	1.370(2)
$d_{\text{N2-C1}} / \text{\AA}$	1.333(2)	1.324(2)
$d_{\text{C1-N3}} / \text{\AA}$	1.332(2)	1.336(3)
$d_{\text{N3-C2}} / \text{\AA}$	1.373(2)	1.370(3)
$d_{\text{C2-C3}} / \text{\AA}$	1.396(3)	1.401(3)
$d_{\text{C3-C4}} / \text{\AA}$	1.382(3)	1.376(3)
$d_{\text{C4-C5}} / \text{\AA}$	1.500(3)	1.507(3)
$d_{\text{C5-N4}} / \text{\AA}$	1.486(3)	1.481(3)
$d_{\text{N4-C6}} / \text{\AA}$	1.470(3)	1.471(3)
$d_{\text{C6-C7}} / \text{\AA}$	1.505(3)	1.502(3)
$d_{\text{C7-C4}} / \text{\AA}$	1.388(3)	1.394(3)
$d_{\text{C7-C8}} / \text{\AA}$	1.376(3)	1.381(3)
$d_{\text{C8-C9}} / \text{\AA}$	1.401(3)	1.386(3)
$d_{\text{C9-N1}} / \text{\AA}$	1.380(2)	1.384(2)
$d_{\text{C2-C9}} / \text{\AA}$	1.413(3)	1.415(3)
$d_{\text{N4-O1}} / \text{\AA}$	1.266(2)	1.273(2)
dihedral angle / °	62.357(50) [N1-Ph] 12.17(11) [C1-Ph]	78.645(58)

Table 3-2. Crystallographic data of **3PPO** and **3BPO**.

	3PPO	3BPO
Chemical formula	C ₂₅ H ₂₄ N ₄ O	C ₂₃ H ₂₈ N ₄ O
Formula weight	396.48	376.49
Temperature / K	296	296
Crystal size / mm ³	0.46 × 0.23 × 0.24	0.89 × 0.32 × 0.15
Space group	<i>P</i> 2 ₁ / <i>c</i> (No. 14)	<i>P</i> 2 ₁ / <i>c</i> (No. 14)
<i>a</i> / Å	5.9298(8)	15.4810(11)
<i>b</i> / Å	22.301(3)	5.9080(5)
<i>c</i> / Å	16.060(2)	23.3520(16)
β / °	92.685(5)	95.564(2)
<i>V</i> / Å ³	2121.5(5)	2125.8(3)
<i>Z</i>	4	4
<i>d</i> _{calc} / g cm ⁻³	1.241	1.176
μ / mm ⁻¹	0.078	0.074
F(000)	840	808
θ (min, max) / °	2.22, 27.12	2.29, 25.86
	$-7 \leq h \leq 7$	$-18 \leq h \leq 17$
Index ranges	$-7 \leq k \leq 6$	$-7 \leq k \leq 6$
	$-27 \leq l \leq 28$	$-27 \leq l \leq 28$
Measured reflection	19117	16789
Independent reflection (<i>R</i> _{int})	4692 (0.0482)	4075 (0.0527)
Obs. reflection ($I \geq 2\sigma(I)$)	2618	2540
Goodness of fit on <i>F</i> ²	0.800	0.994
<i>R</i> , <i>R</i> _w ($I \geq 2\sigma(I)$)	0.0507, 0.1769	0.0521, 0.1443
<i>R</i> , <i>R</i> _w (all data)	0.1072, 0.2329	0.0991, 0.1755
Resd density (min, max) / e Å ⁻³	-0.323, 0.243	-0.259, 0.240

Radical **3PPO** belongs to monoclinic crystal system and $P2_1/c$ space group. In the crystal structure, **3PPO** form slipped 1D columnar structure along a axis due to π - π interaction between C1-phenyl ring and amidrazonyl ring (Figure 3-7). In spite of bulky methyl groups, the molecules stacked in parallel with 3.83 Å separation. Nitroxyl moiety directs to the N1-phenyl ring, which is not effective contact to magnetic coupling.

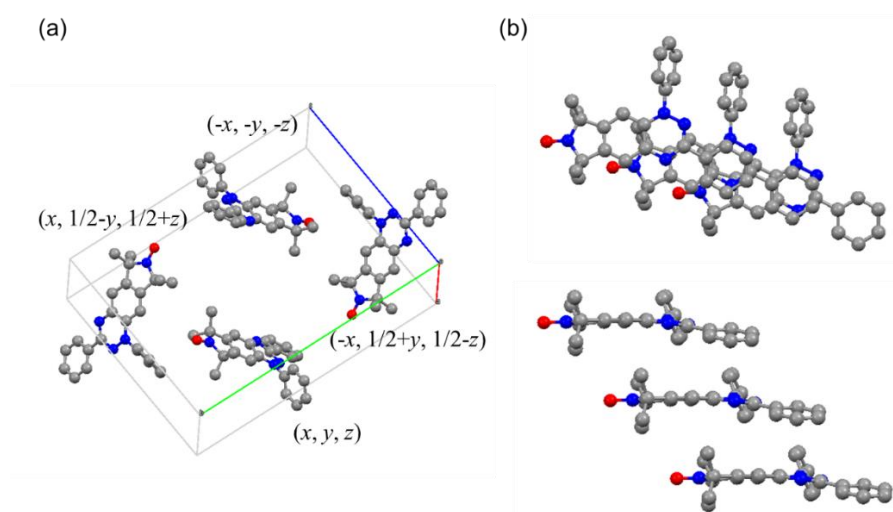


Figure 3-7. (a) Crystal structure and (b) columnar structure of **3PPO**. Hydrogen atoms are omitted for clarity.

Radical **3BPO** also belongs to monoclinic crystal system and $P2_1/c$ space group. **3BPO** form slipped 1D columnar structure along b axis with $ca.$ 4.7 Å separation (Figure 3-8). In column, the molecules parallelly stack to avoid the contact of *tert*-butyl group and CH- π interaction between heterocyclic ring and H 15 atom of N1-phenyl ring with 3.22 Å distance is existed. Therefore CH- π interaction work to construct columnar structure as driving force. There is no close contact around nitroxyl moiety.

The longitudinal slippage ϕ_1 and latitudinal slippage ϕ_2 are shown in Table 3-3 (The definition of ϕ_1 and ϕ_2 are shown in Figure 2-12). It insists that there are small overlaps between π -conjugation systems for **3PPO** and **3BPO**. It suggests that there are weak magnetic interactions between the molecules.

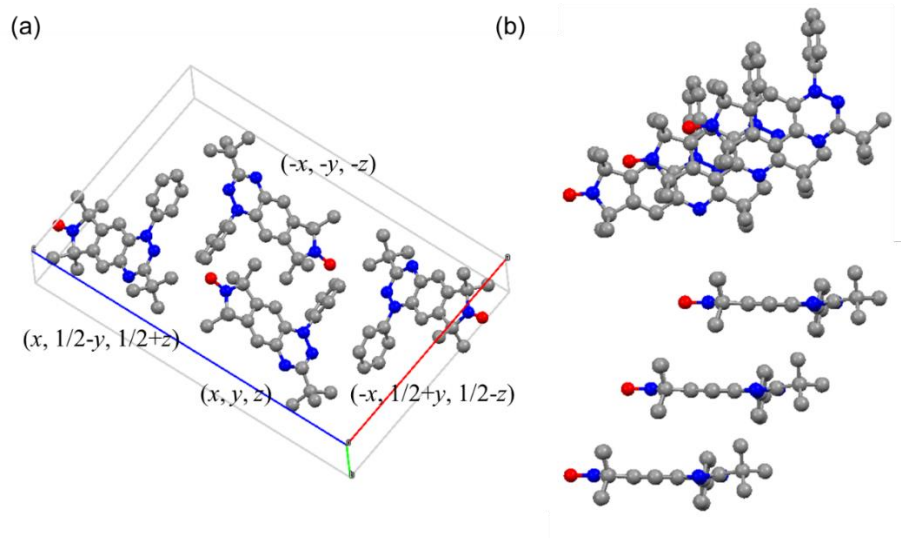


Figure 3-8. (a) Crystal structure and (b) columnar structure of **3BPO**. Hydrogen atoms are omitted for clarity.

Table 3-3. The longitudinal and latitudinal slippage of **3PPO** and **3BPO**.

Compound	$\phi_1 / ^\circ$	$\phi_2 / ^\circ$
3PPO	75.3	46.8
3BPO	70.5	55.8

3.4. Magnetic Property

The magnetic susceptibility measurement of polycrystalline samples for **3PPO** and **3BPO** were carried out with Quantum Design MPMS-XL SQUID magnetometer. The diamagnetic susceptibility χ_{dia} was estimated by Pacault method¹⁴ (**3PPO**: -2.49×10^{-4} emu mol⁻¹, **3BPO**: -2.47×10^{-4} emu mol⁻¹).

The thermal dependence of χ_{m} for **3PPO** is shown in Figure 3-9(a). The χ_{m} value was increased and reached maxima at 70 K, then converged to zero with decreasing temperature. The $\chi_{\text{m}}T$ value at ambient temperature was 0.669 emu K mol⁻¹, which is smaller value than that of isolated doublet spins ($S = 1/2 \times 2$, 0.750 emu K mol⁻¹), and was decreased to almost zero with cooling. Thermal behavior of magnetic susceptibility is well described with the Bleaney-Bowers dimer model¹⁵ with best-fit parameter $2J = -77.1$ cm⁻¹ including 0.26% of monoradical fraction. To get rid of the attribution for intermolecular interaction, the polystyrene diluted sample of **3PPO** was prepared (Figure 3-9(c)). The χ_{m} of diluted sample exhibited similar behavior to that of polycrystalline sample. It suggested the existence of intramolecular strong antiferromagnetic interaction.

The thermal dependence of χ_{m} for **3BPO** is shown in Figure 3-9(b). The χ_{m} value was increased and reached maxima at 73 K, then converged to zero with decreasing temperature. The $\chi_{\text{m}}T$ value at ambient temperature was 0.673 emu K mol⁻¹, which is slightly smaller value than that of isolated doublet spins ($S = 1/2 \times 2$, 0.750 emu K mol⁻¹), and was decreased to almost zero with cooling. The increase of χ_{m} was attribution of paramagnetic impurity. Thermal behavior of magnetic susceptibility is well described with the Bleaney-Bowers dimer model with best-fit parameter $2J = -80.0$ cm⁻¹ including 1.7% of monoradical fraction. As shown, strong intramolecular antiferromagnetic interaction is dominant in **3BPO**, which is the same as **3PPO**. The polystyrene diluted sample exhibited similar thermal behavior to that of polycrystalline sample, suggesting the existence of intramolecular strong antiferromagnetic interaction (Figure 3-9(c)).

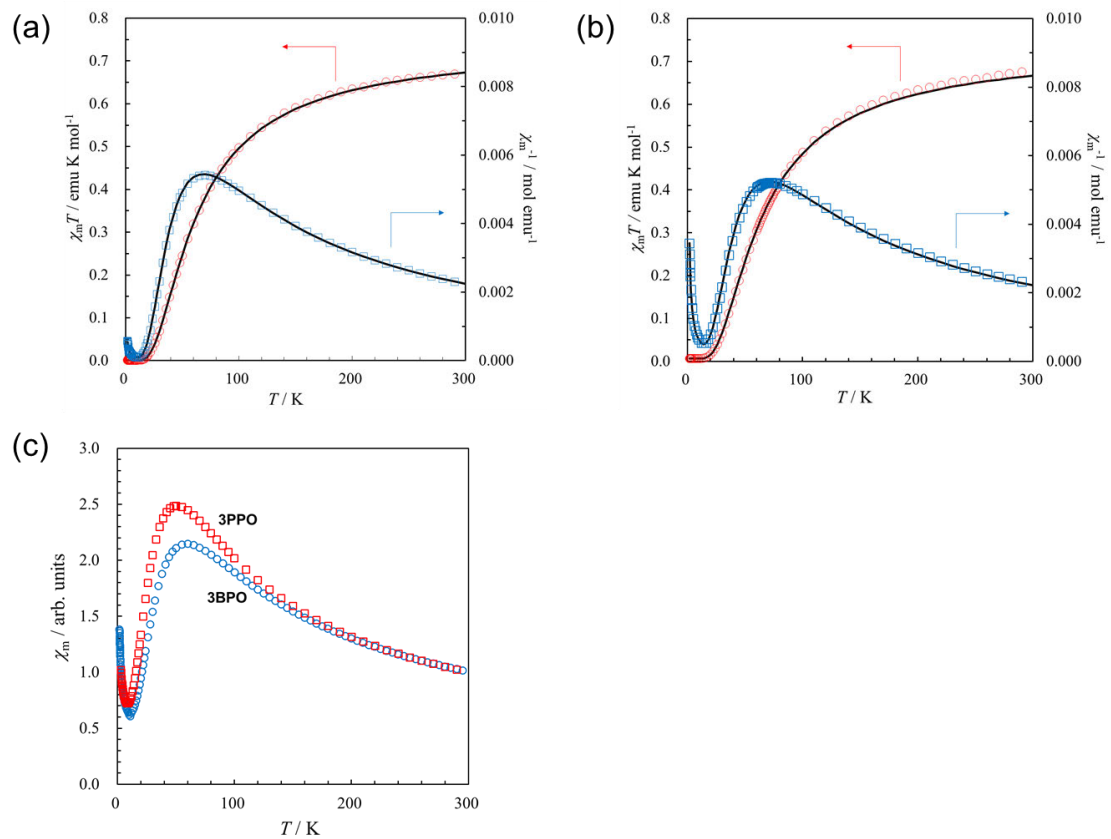


Figure 3-9. The temperature dependence of χ_m (\square) and $\chi_m T$ (\circ) for polycrystalline sample of (a) **3PPO** and (b) **3BPO**. Solid lines are best-fit result of the Bleaney-Bowers dimer model. (c) The temperature dependence of χ_m for polystyrene diluted-sample of **3PPO** (\square) and **3BPO** (\circ).

3.5. Evaluation of Magnetic Interaction Based on Computation

To estimate the SOMO distribution, single point calculation using crystallographic coordinate were carried out with DFT method (UB3LYP/6-31G(d) level) in Gaussian 09 program.¹⁶ The SOMO of **3PPO** and **3BPO** are shown in Figure 3-10. Notably, the SOMO derived from benzotriazinyl site distribute not only the parent skeleton but also nitroxyl group through sp^3 carbon, this phenomenon is observed in nitroxyl site. It suggested that the existence of interaction between SOMOs through sp^3 carbon. The magnitude of intramolecular interaction was estimated by Yamaguchi's equation (equation 2-1).¹⁷ The estimated $2J$ values were -116.0 cm^{-1} for **3PPO** and -100.1 cm^{-1} for **3BPO** (Table 3-5). Although the overestimation due to the spin contamination was observed, the negative J values indicated the existence of antiferromagnetic interaction, which is consistent with the experimental results. The computation also revealed that there are no effective intermolecular magnetic interactions.

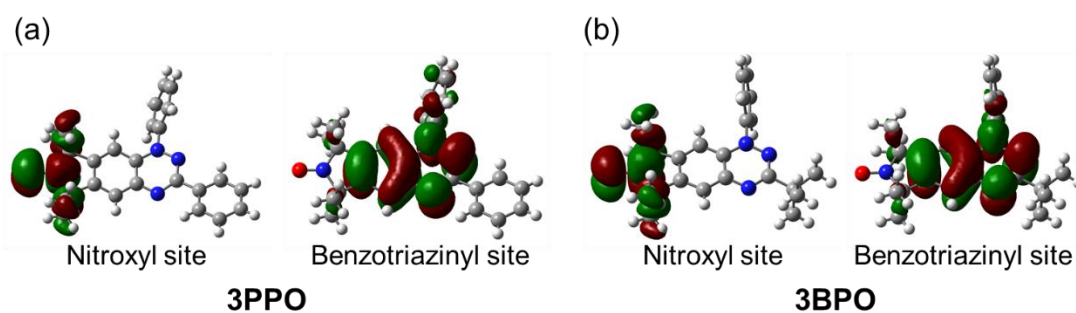


Figure 3-10. The SOMO distribution of (a) **3PPO** and (b) **3BPO** at UB3LYP/6-31G(d) level.

Table 3-5. Calculation result of **3PPO** and **3BPO**.

Compound	Energy(BS/T) / a.u.	$\langle S^2 \rangle$ (BS/T)	$2J / \text{cm}^{-1}$
3PPO	-1186.9936126 / -1260.8162309	1.010282 / 2.019077	-116.0
3BPO	-1187.3263150 / -1186.9933840	1.009595 / 2.017708	-100.1

The mechanism of intramolecular magnetic interaction can be explained in the viewpoint of the spin density distribution. When the spin center exhibits the intramolecular magnetic interaction against the other spin center, the spin density has to distribute on the cross-linking moiety of each spin centers. Then, the spin density of each spin centers was calculated at UB3LYP/6-31G(d) level. The spin density of pyrroline *N*-oxyl mainly distribute on nitroxyl and tetramethyl groups and slightly polarized to vinylic moiety as shown in Figure 3-1, which is consistent with the spectroscopic studies of the pyrroline *N*-oxyl analogue¹². There are negative spins on the sp^3 carbon atoms of adjacent N atom and positive spin on vinylic C atoms, respectively. The spin density of pyrroline ring fused benzotriazinyl radicals **3PPO'** and **3BPO'** was also calculated (Figure 3-11). There are negative spins on sp^3 carbons and is positive spin on the N atom of pyrroline ring. Considering the spin alignment, the predicted intramolecular magnetic interaction based on through-bond consideration will be ferromagnetic (Figure 3-12), which was conflict with the experimental results due to the weak spin polarization through σ -bond.

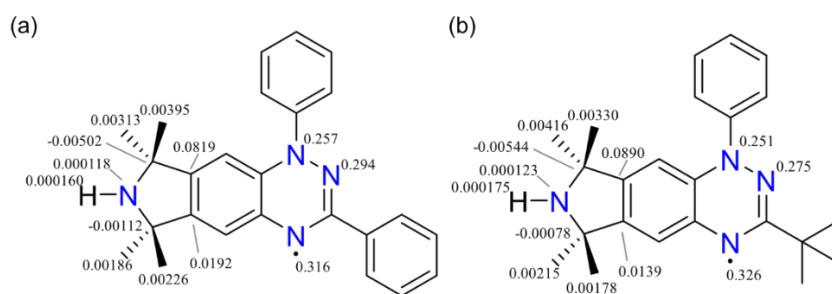


Figure 3-11. Spin density of (a) **3PPO'** and (b) **3BPO** at UB3LYP/6-31G(d) level.

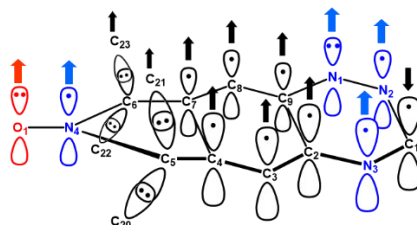


Figure 3-12. Schematic illustration of spin density of **3PPO** and **3BPO**. Phenyl ring and *tert*-butyl group were omitted for clarity.

The intermolecular antiferromagnetic interaction also can be interpreted by considering SOMO-SOMO interaction through-space and through-bond. According to the mechanism proposed by Dougherty,¹⁸ NBMOs of cyclobutanediyl are degenerate due to the through-bond and through-space interactions as described in chapter 1. In our system, the energy level of MO with the same phase of SOMOs for nitroxyl and benzotriazinyl radicals (denoted as MO_A in Figure 3-13) is lower than that of the opposite phase (denoted as MO_B in Figure 3-13) due to the through-space interaction. Considering the through-bond interaction, there are pseudo π orbitals on sp^3 carbons, which contribute to raise the energy level of MO_A. However, MO_A and MO_B are not degenerate and antiferromagnetic interaction was preferred.

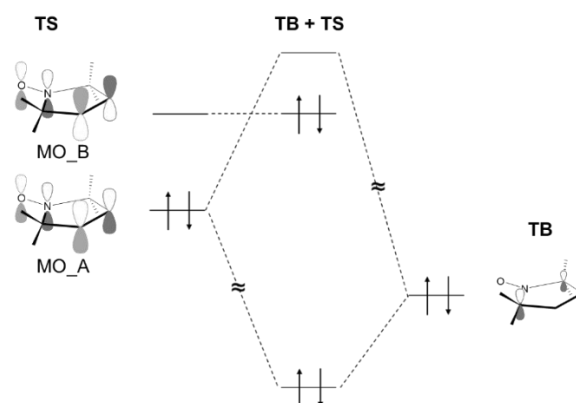


Figure 3-13. The energy diagram of **3PPO** and **3BPO**. TS and TB represent through-space and through-bond interaction.

3.6. ESR Measurement

The ESR spectra of **3PPO** and **3BPO** in toluene at room temperature are shown in Figures 3-14(a) and 3-15(a). The broad spectra were observed due to the interaction of unpaired electrons and sharp signals were attributed to nitroxide monoradical impurity. The spectra in toluene glass matrix at 4 K are shown in Figures 3-14(b) and 3-15(b). In $g = 2$ region, the spectra exhibited fine structure because of zero field splitting. The signal observed at center was attributed to the corresponding monoradical impurities. The D values were estimated from the most outer signal ($2D = 44.3$ mT for **3PPO** and 44.0 mT for **3BPO**) and the point-dipole approximation gave the spin-spin distance (**3PPO**: 5.01 Å, **3BPO**: 5.02 Å), which is shorter than the distance between the center of nitroxyl moiety and nitrogen atoms of amidrazonyl ring due to the delocalization of unpaired electron. In addition, half field signals of $\Delta m_s = \pm 2$ were observed in $g = 4$ region (inset of Figures 3-14(b) and 3-15(b)). The Curie plots of **3PPO** and **3BPO** are shown in Figures 3-14(c) and 3-15(c). The non-linear relationship between intensity of $g = 4$ and reciprocal temperature suggest that **3PPO** and **3BPO** have ground singlet state.

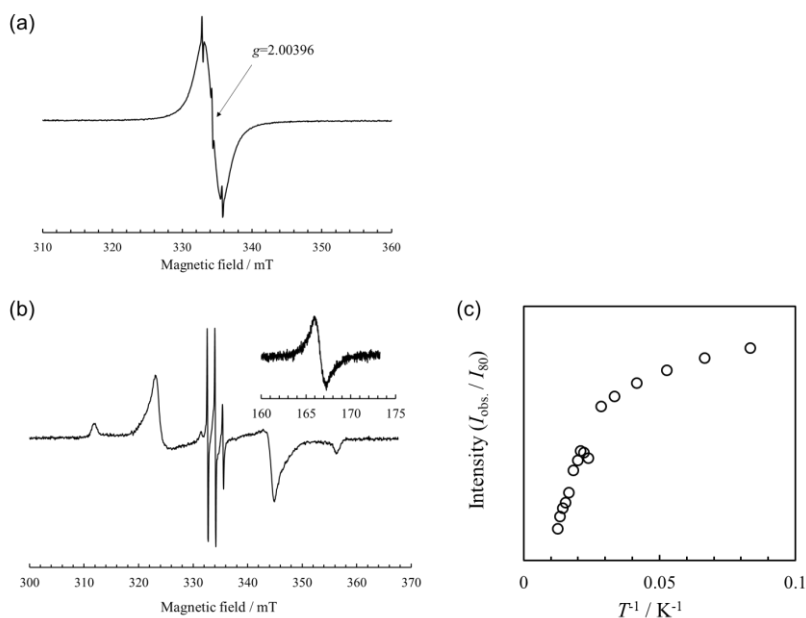


Figure 3-14. The ESR spectra of **3PPO**. (a) $\Delta m_s = \pm 1$ signal at room temperature. (b) $\Delta m_s = \pm 1$ signal at 4 K. Inset represents the half field signal of $\Delta m_s = \pm 2$. (c) Curie plot of $\Delta m_s = \pm 2$ signal.

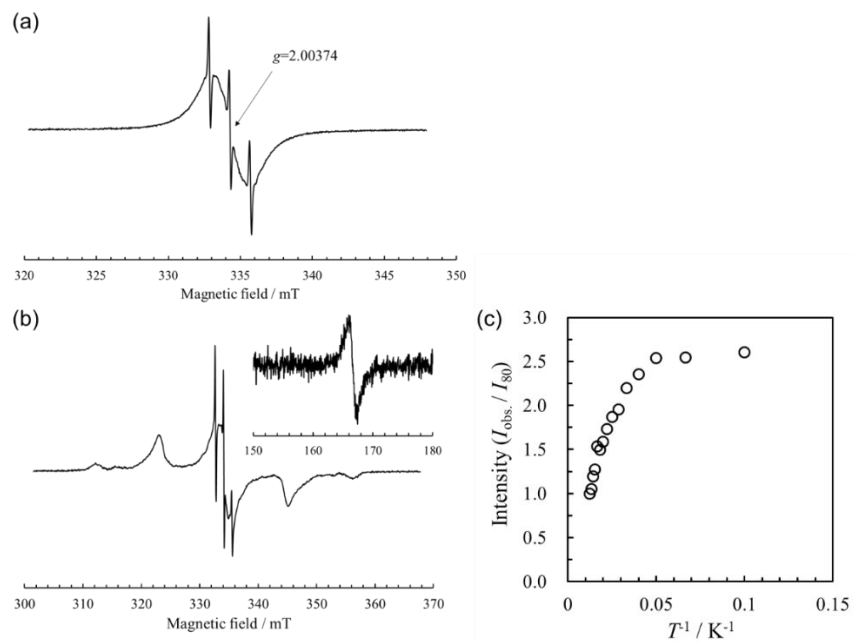


Figure 3-15. The ESR spectra of **3BPO**. (a) $\Delta m_s = \pm 1$ signal at room temperature. (b) $\Delta m_s = \pm 1$ signal at 4 K. Inset represents the half field signal of $\Delta m_s = \pm 2$. (c) Curie plot of $\Delta m_s = \pm 2$ signal.

References in Chapter 3

- (a) T. Suga, H. Konishi, H. Nishide, *Chem. Commun.*, **2007**, 1730.
 - (b) W. Choi, S. Endo, K. Oyaizu, H. Nishide, K. E. Geckeler, *J. Mater. Chem. A*, **2013**, *1*, 2999.
- (a) J. F. W. Keana, *Chem. Rev.*, **1978**, *78*, 37.
 - (b) G.-P. Yan, D. Bischa, S. E. Bottle, *Free Radical Biol. Med.*, **2007**, *43*, 111.
 - (c) M. Sajid, G. Jeschke, M. Wiebcke, A. Godt, *Chem.–Eur J.*, **2009**, *15*, 12960.
 - (d) E. G. Bagryanskaya, O. A. Krumkacheva, M. V. Fedin, S. R. A. Marque, *Method Enzymol.* **2015**, *563*, 365.
- (a) T. Fukuda, T. Terauchi, A. Goto, K. Ohno, Y. Tsujii, T. Miyamoto, S. Kobatake, B. Yamada, *Macromolecules*, **1996**, *29*, 6393.
 - (b) D. Benoit, V. Chaplinski, R. Braslau, C. J. Hawker, *J. Am. Chem. Soc.*, **1999**, *121*, 3904.
 - (c) C. J. Hawker, A. W. Bosman, E. Harth, *Chem. Rev.*, **2001**, *101*, 3661.
- (a) R. A. Sheldon, I. W. C. E. Arends, *Adv. Synth. Catal.*, **2004**, *346*, 1051.
 - (b) T. Vogler, A. Studer, *Synthesis*, **2008**, *13*, 1979.
 - (c) S. D. McCann, S. S. Stahl, *Acc. Chem. Res.*, **2015**, *48*, 1756.
- O. Piloty, B. G. Schwerin, *Berichte der Deutschen Chemischen Gesellschaft*, **1901**, *34*, 1870.
- G. Murata, S. Takeda, R. Imachi, T. Ishida, T. Nogami, K. Yamaguchi, *J. Am. Chem. Soc.* **1999**, *121*, 424.
- (a) L. B. Volodarsky, V. A. Reznikov, V. I. Ovcharenko, *Synthetic Chemistry of Stable Nitroxides*; Boca Raton, FL, CRC Press, 1994.
 - (b) D. J. Keddie, K. E. Fairfull-Smith, S. E. Bottle, *Org. Biomol. Chem.*, **2008**, *6*, 3135.
 - (c) J. P. Blinco, J. L. Hodgson, B. J. Morrow, J. R. Walker, G. D. Will, M. L. Coote, S. E. Bottle, *J. Org. Chem.* **2008**, *73*, 6763.
 - (d) K. E. Fairfull-Smith, F. Brackmann, S. E. Bottle, *Eur. J. Org. Chem.* **2009**, 1902.
- T. Kálai, M. Balog, J. Jekő, W. L. Hubbell, K. Hideg, *Synthesis*, **2002**, 2365.
- T. Kálai, J. Schindler, M. Balog, E. Fogassy, K. Hideg, *Tetrahedron*, **2008**, *64*, 1094.
- (a) A. Rajca, S. Rajca, J. Wongsriratanakul, *J. Am. Chem. Soc.*, **1999**, *121*, 6308.
 - (b) A. Rajca, J. Wongsriratanakul, S. Rajca, *Science*, **2001**, *294*, 1503.
- (a) N. N. Tyutyulkov, S. H. Karabunarliev, *Chem. Phys.*, **1987**, *112*, 293.
 - (b) N. Tyutyulkov, S. H. Karabunarliev, K. Müllen; M. Baumgarten, *Synth. Met.*, **1992**, *52*, 71.
 - (c) F. Dietz, N. Tyutyulkov, *Chem. Phys.*, **2001**, *264*, 37.
- R. Bolton, D. G. Gillies, L. H. Sutcliffe, X. Wu, *J. Chem. Soc., Perkin Trans. 2* **1993**, 2049.
- (a) M.-C. Frantz, E. M. Skoda, J. R. Sacher, M. W. Epperly, J. P. Goff, J. S. Greenberger, P. Wipf, *Org. Biomol. Chem.*, **2013**, *11*, 4147.
 - (b) E. Mileo, E. Etienne, M. Martinho, R. Lebrun, V. Roubaud, P. Tordo, B. Gontero, B. Guigliarelli, S. R. A. Marque, V. Belle, *Bioconjugate Chem.*, **2013**, *24*, 1110.

14. R. Gupta, in *Landolt-Börnstein New Series Group II* (Eds. K. -H. Hellwege and A. M. Hellwege), Springer, Berlin, Germany, 1986, Vol. 16, ch. 1.2.
15. B. Bleaney, K. D. Bowers, *Proc. R. Soc. London, Ser. A*, **1952**, 214, 451.
16. Gaussian 09: Revision D.01, M. J. Frisch, G. W. Trucks, H. B. Schlegel, G. E. Scuseria, M. A. Robb, J. R. Cheeseman, G. Scalmani, V. Barone, B. Mennucci, G. A. Petersson, H. Nakatsuji, M. Caricato, X. Li, H. P. Hratchian, A. F. Izmaylov, J. Bloino, G. Zheng, J. L. Sonnenberg, M. Hada, M. Ehara, K. Toyota, R. Fukuda, J. Hasegawa, M. Ishida, T. Nakajima, Y. Honda, O. Kitao, H. Nakai, T. Vreven, J. A. Montgomery, Jr., J. E. Peralta, F. Ogliaro, M. Bearpark, J. J. Heyd, E. Brothers, K. N. Kudin, V. N. Staroverov, R. Kobayashi, J. Normand, K. Raghavachari, A. Rendell, J. C. Burant, S. S. Iyengar, J. Tomasi, M. Cossi, N. Rega, J. M. Millam, M. Klene, J. E. Knox, J. B. Cross, V. Bakken, C. Adamo, J. Jaramillo, R. Gomperts, R. E. Stratmann, O. Yazyev, A. J. Austin, R. Cammi, C. Pomelli, J. W. Ochterski, R. L. Martin, K. Morokuma, V. G. Zakrzewski, G. A. Voth, P. Salvador, J. J. Dannenberg, S. Dapprich, A. D. Daniels, Ö. Farkas, J. B. Foresman, J. V. Ortiz, J. Cioslowski, D. J. Fox, Gaussian, Inc., Wallingford CT, 2009.
17. K. Yamaguchi, H. Fukui, T. Fueno, *Chem. Lett.*, **1986**, 625.
18. D. A. Dougherty, *Acc. Chem. Res.*, **1991**, 24, 88.

Chapter 4: Magneto-Structural Correlation in Nitroxyl-Verdazyl/Nitronyl Nitroxide Hetero Biradicals

4.1. Introduction

As described in chapter 3, the antiferromagnetic interaction through non-conjugated framework was observed in nitroxyl-triazinyl hetero biradical system, which was mainly attributed to through-space interaction. To explore the magnetic interaction through non-conjugated framework, the computational study of allyl radical attached and embedded hetero biradicals **POA1** and **POA2** were carried out to estimate the contribution of SOMO for intramolecular interaction (Figure 4-1). The calculated J value $2J = +7.1$ and -109.8 cm^{-1} for **POA1** and **POA2** implied intramolecular ferromagnetic and antiferromagnetic interaction, respectively. For **POA1**, there was larger β spin density on vinylic moiety than α spin and the SOMO of allyl radical site distributed on allyl moiety. On the other hand, for **POA2**, there was larger α spin on vinylic moiety and the SOMO of allyl radical distributed not only allyl group but also $\text{C}(\text{CH}_3)_2$ moiety (Figures 4-1 and 4-2). Thus, the distribution of the spin density of vinylic moiety without SOMO derived from attached radical may be essential to exhibit intramolecular ferromagnetic interaction. The computation also suggested that the spin-spin interaction is preferred in pyrroline *N*-oxyl hetero biradical system. Based on this condition, the hetero biradicals **POVZ** and **PONN** are designed, whose spin density is similar to **POA1** and intramolecular ferromagnetic interaction can be expected (Figure 4-3).

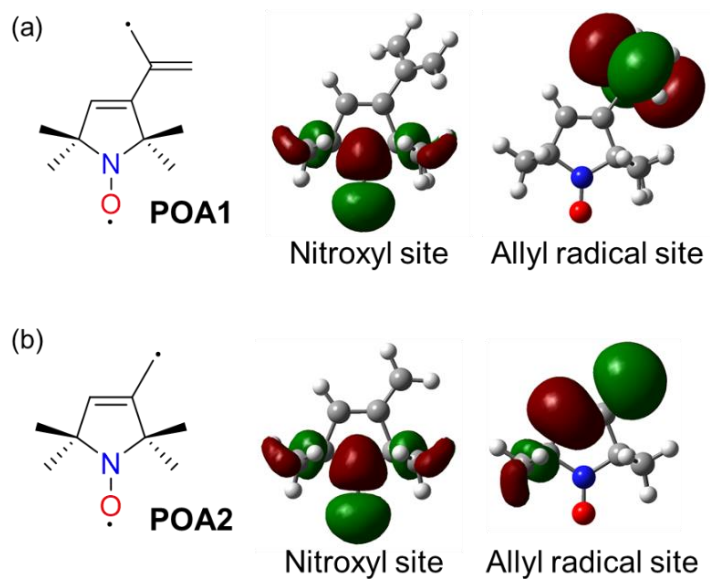


Figure 4-1. The molecular structures and SOMO distributions of the optimized geometry for (a) **POA1** and (b) **POA2**. The calculations were carried out at UB3LYP/6-31G(d) level. [*ChemPhysChem*, **2018**, *19*, 175.] - Copyright 2018, Wiley-VCH Verlag GmbH and Co. KGaA. Reproduced with permission.

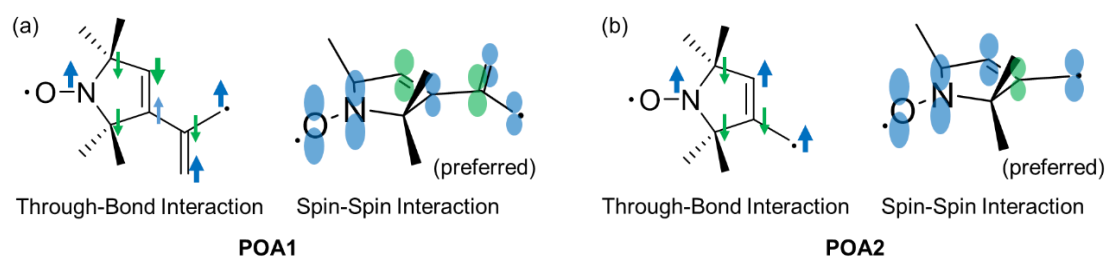


Figure 4-2. The possible pathway of intramolecular magnetic interaction for (a) **POA1** and (b) **POA2**.

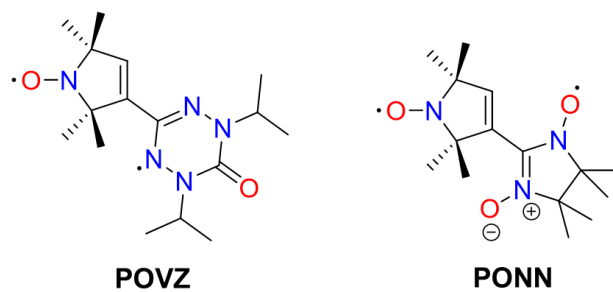
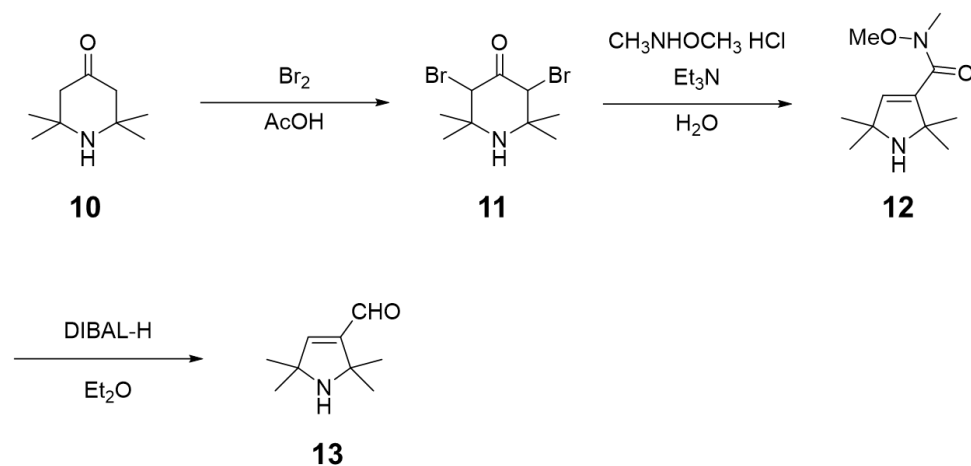


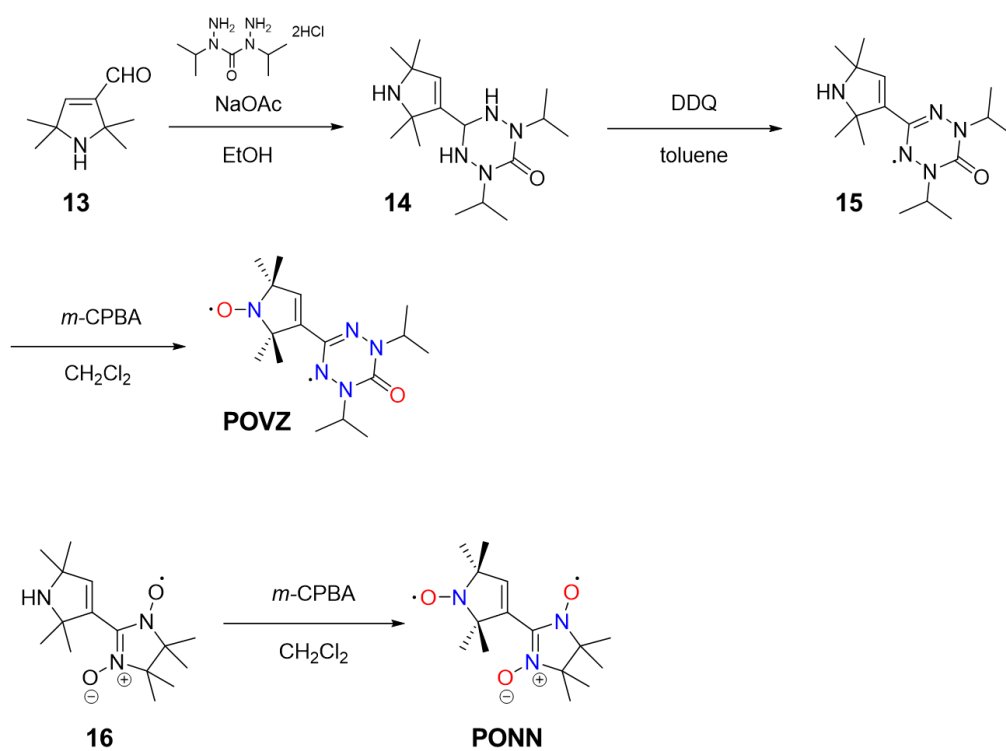
Figure 4-3. The molecular structures of **POVZ** and **PONN**.

4.2. Synthesis

Pyrroline *N*-oxyl attached biradicals **POVZ** and **PONN** were synthesized according to Schemes 4-1 and 4-2. Aldehyde **13** and compound **16** were prepared via several steps in the similar manner according to the literature.^{1,2}



Scheme 4-1. Synthetic route of aldehyde **13**.



Scheme 4-2. Synthetic routes of **POVZ** and **PONN**.

4.3. Crystallographic Analysis

Single crystals of **POVZ** and **PONN** suitable for X-ray analysis were obtained by slow evaporation in mixed solvent of $\text{CH}_2\text{Cl}_2/\text{MeOH}$ and MeOH . Crystal structure of **PONN** was already reported by Hideg *et al.*², denoted as **PONN- α** (CSD Refcode: ROQWUP), however, different crystal structure was found, denoted as **PONN- β** . Crystallographic data are shown in Table 4-1. The ORTEP drawings are shown in Figure 4-4 and selected bond lengths and dihedral angle between pyrroline ring and verdazyl ring / O-N-C-N-O plane are shown in Table 4-2. The bond lengths of radical moieties are within typical values of corresponding parent radicals.

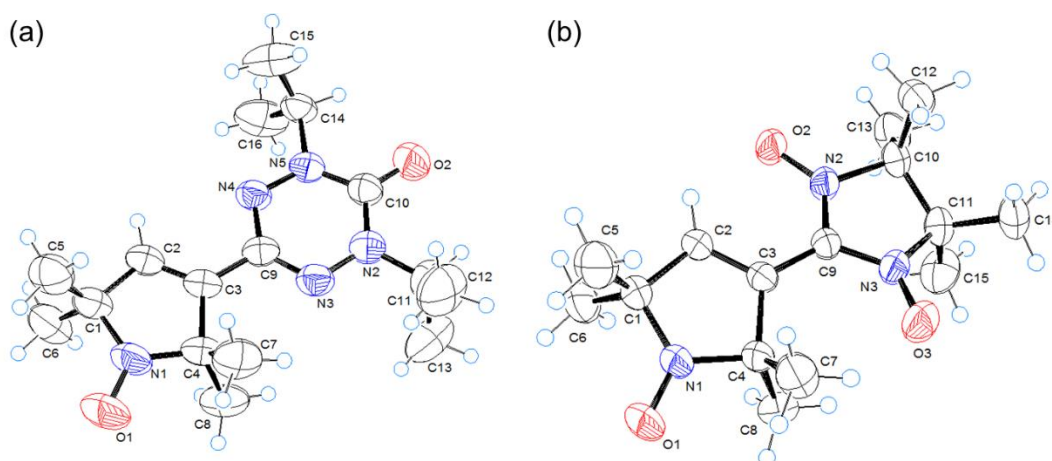


Figure 4-4. ORTEP drawings of (a) **POVZ** and (b) **PONN- β** with 50% thermal ellipsoids. [ChemPhysChem, 2018, 19, 175.] - Copyright 2018, Wiley-VCH Verlag GmbH and Co. KGaA. Reproduced with permission.

Table 4-1. Crystallographic data of **POVZ** and **PONN-β**.

	POVZ	PONN-β
Chemical formula	C ₁₆ H ₂₇ N ₅ O ₂	C ₁₅ H ₂₅ N ₃ O ₃
Formula weight	321.41	295.38
Temperature / K	300	296
Crystal size / mm ³	1.21 × 0.12 × 0.7	0.82 × 0.22 × 0.16
Space group	<i>P</i> 2 ₁ / <i>c</i> (No. 14)	<i>P</i> -1 (No. 2)
<i>a</i> / Å	5.8987(7)	6.2200(5)
<i>b</i> / Å	16.0757(17)	10.5421(8)
<i>c</i> / Å	19.3901(19)	13.0568(10)
α / °	90	88.669(2)
β / °	90.677(3)	89.884(3)
γ / °	90	76.790(2)
<i>V</i> / Å ³	1838.6(3)	833.27(11)
<i>Z</i>	4	2
<i>d</i> _{calc} / g cm ⁻³	1.161	1.177
μ / mm ⁻¹	0.079	0.083
F(000)	696	320
θ (min, max) / °	2.45, 24.76	2.50, 26.40
	-6 ≤ <i>h</i> ≤ 6	-7 ≤ <i>h</i> ≤ 7
Index ranges	-18 ≤ <i>k</i> ≤ 16	-12 ≤ <i>k</i> ≤ 13
	-22 ≤ <i>l</i> ≤ 22	-11 ≤ <i>l</i> ≤ 16
Measured reflection	15927	7899
Independent reflection (<i>R</i> _{int})	3107 (0.0511)	3224 (0.0217)
Obs. Reflection (<i>I</i> ≥ 2σ(<i>I</i>))	1731	2404
Goodness of fit on <i>F</i> ²	0.977	1.072
<i>R</i> , <i>R</i> _w (<i>I</i> ≥ 2σ(<i>I</i>))	0.0615, 0.1195	0.0518, 0.1407
<i>R</i> , <i>R</i> _w (all data)	0.2097, 0.2832	0.0742, 0.1809
Resd density (min, max) / e Å ⁻³	-0.257, 0.187	-0.307, 0.216

Table 4-2. Selected bond lengths and dihedral angle of **POVZ** and **PONN-β**.

Compound	POVZ	PONN-β
$d_{\text{N1-C1}} / \text{Å}$	1.474(4)	1.466(3)
$d_{\text{C1-C2}} / \text{Å}$	1.491(4)	1.486(3)
$d_{\text{C2-C3}} / \text{Å}$	1.322(4)	1.336(3)
$d_{\text{C3-C4}} / \text{Å}$	1.525(4)	1.527(3)
$d_{\text{C4-N1}} / \text{Å}$	1.472(4)	1.489(3)
$d_{\text{N1-O1}} / \text{Å}$	1.278(4)	1.269(2)
$d_{\text{C1-C5}} / \text{Å}$	1.516(5)	1.522(4)
$d_{\text{C1-C6}} / \text{Å}$	1.541(5)	1.526(3)
$d_{\text{C4-C7}} / \text{Å}$	1.517(5)	1.523(3)
$d_{\text{C4-C8}} / \text{Å}$	1.526(5)	1.524(3)
$d_{\text{C3-C9}} / \text{Å}$	1.458(4)	1.448(3)
$d_{\text{N2-O2}} / \text{Å}$	-	1.274(2)
$d_{\text{N2-C9}} / \text{Å}$	-	1.359(3)
$d_{\text{C9-N3}} / \text{Å}$	-	1.350(3)
$d_{\text{N3-O3}} / \text{Å}$	-	1.267(2)
$d_{\text{N2-N3}} / \text{Å}$	1.366(4)	-
$d_{\text{N3-C9}} / \text{Å}$	1.322(4)	-
$d_{\text{C9-N4}} / \text{Å}$	1.347(4)	-
$d_{\text{N4-N5}} / \text{Å}$	1.362(4)	-
$d_{\text{C10-O2}} / \text{Å}$	1.220(4)	-
dihedral angle / °	5.085(179)	14.828(189)

Radical **POVZ** belongs to monoclinic crystal system and $P2_1/c$ space group. **POVZ** form slipped 1D columnar structure along a axis with 4.84 Å separation (Figure 4-5). In the columnar structure, the molecules parallelly stack to avoid methyl group. Due to long distance between verdazyl rings, there is no effective contact for magnetic coupling between verdazyl moieties. Regarding nitroxyl site, there is no close contact of other molecules.

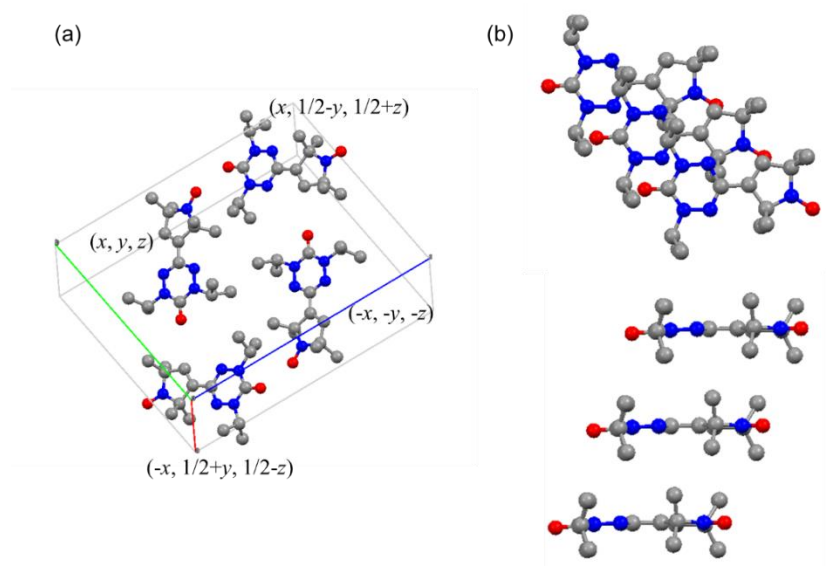


Figure 4-5. (a) Crystal structure and (b) columnar structure of **POVZ**. Hydrogen atoms are omitted for clarity. [*ChemPhysChem*, **2018**, *19*, 175.] - Copyright 2018, Wiley-VCH Verlag GmbH and Co. KGaA. Reproduced with permission.

Radical **PONN-β** belongs to triclinic crystal system and $P-1$ space group. In the crystal structure, **PONN-β** form 2D sheet structure due to hydrogen bonding between nitroxyl group and methyl group (Figure 4-6). Steric effect of methyl groups separates the distance of sheet structures with 4.94 Å. In the sheet structure, the molecules are antiparallely aligned along b axis. On the other hand, in crystal **PONN-α** (Figure 4-7), molecules also form 2D sheet structure due to the hydrogen bonding and antiparallely aligned along a axis.

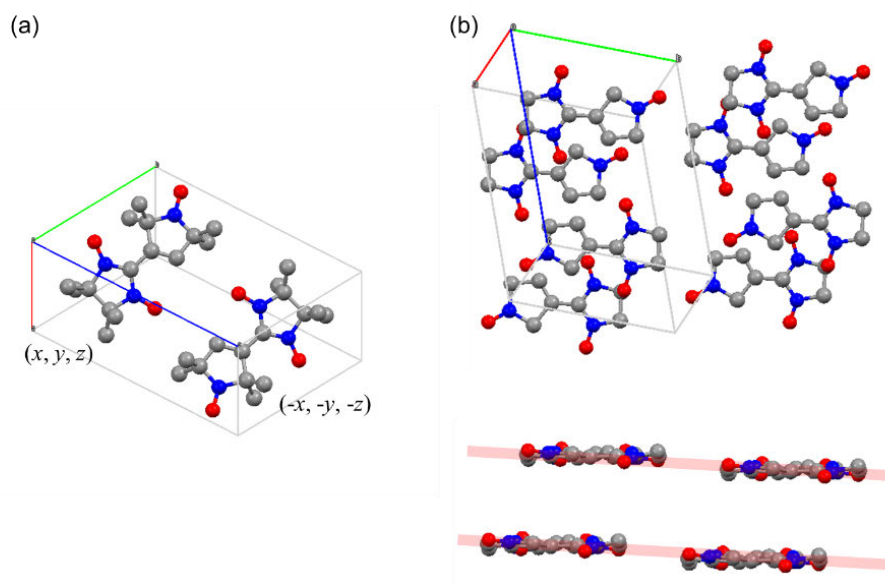


Figure 4-6. (a) Crystal structure and (b) 2D sheet structure of **PONN-β**. Selected methyl groups and hydrogen atoms are omitted for clarity. [*ChemPhysChem*, **2018**, *19*, 175.] - Copyright 2018, Wiley-VCH Verlag GmbH and Co. KGaA. Reproduced with permission.

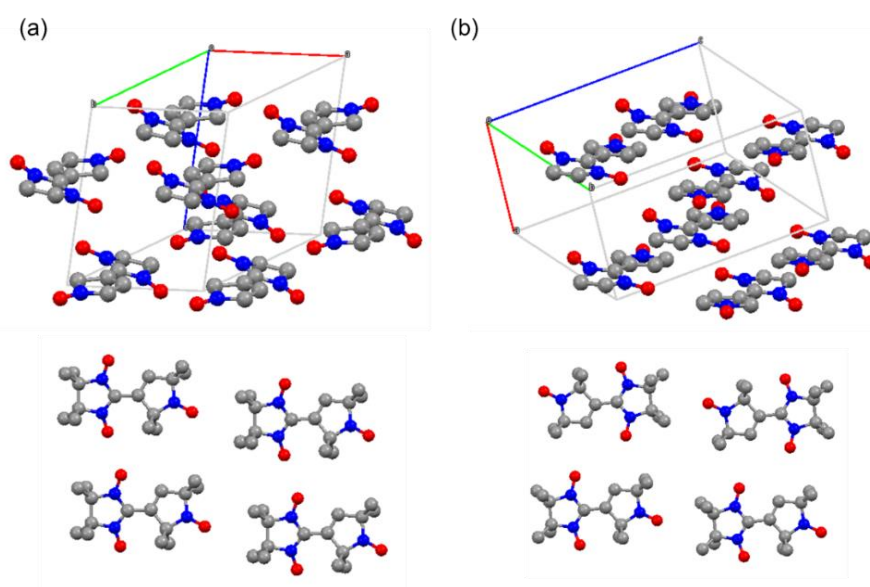


Figure 4-7. Comparison of molecular arrangement in crystal structure (upper) and sheet structure (lower). (a) **PONN-α**. (b) **PONN-β**. [*ChemPhysChem*, **2018**, *19*, 175.] - Copyright 2018, Wiley-VCH Verlag GmbH and Co. KGaA. Reproduced with permission.

4.4. Magnetic Property

The magnetic susceptibility measurement of polycrystalline samples for **POVZ** and **PONN- β** were carried out with a Quantum Design MPMS-XL SQUID magnetometer. The diamagnetic susceptibility χ_{dia} was estimated by the Pacault method³ (**POVZ**: -2.04×10^{-4} emu mol⁻¹, **PONN**: -1.90×10^{-4} emu mol⁻¹).

The temperature dependence of $\chi_{\text{m}}T$ for **POVZ** is shown in Figure 4-8. The magnetic susceptibility followed the Curie-Weiss law with $\theta = +9.41$ K above 200 K, which suggested that ferromagnetic interaction is dominant in solid state. The $\chi_{\text{m}}T$ value at ambient temperature was 0.759 emu K mol⁻¹, which is slightly larger value than that of isolated doublet spins ($S = 1/2 \times 2$, 0.750 emu K mol⁻¹). The increase of $\chi_{\text{m}}T$ was observed with decreasing temperature and it reached at maximum value 0.844 emu K mol⁻¹ at 13 K then, decreased. The behavior of the magnetic susceptibility can be reproduced by the Bleaney-Bowers dimer model⁴ taking account of mean field term θ with $2J = +14.9$ cm⁻¹ and $\theta = -1.40$ K.

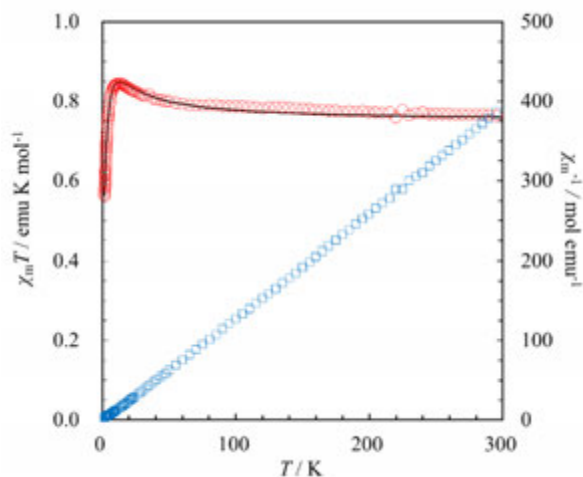


Figure 4-8. The temperature dependence of $\chi_{\text{m}}T$ (\circ) and χ_{m}^{-1} (\square) for polycrystalline sample of **POVZ**. The solid line is best-fit result of the Bleaney-Bowers dimer model. [*ChemPhysChem*, **2018**, *19*, 175.] - Copyright 2018, Wiley-VCH Verlag GmbH and Co. KGaA. Reproduced with permission.

The temperature dependence of $\chi_m T$ for **PONN- β** is shown in Figure 4-9. The magnetic susceptibility followed the Curie-Weiss law with Weiss temperature $\theta = -4.86$ K. The negative Weiss temperature suggested that antiferromagnetic interaction is dominant in solid state. The $\chi_m T$ value at ambient temperature was $0.750 \text{ emu K mol}^{-1}$, which is the same value of that of isolated doublet spins ($S = 1/2 \times 2$, $0.750 \text{ emu K mol}^{-1}$), and was plateau above 100 K then, decreased to $0.248 \text{ emu K mol}^{-1}$ at 1.8 K with cooling. This thermal behavior also suggested antiferromagnetic interaction.

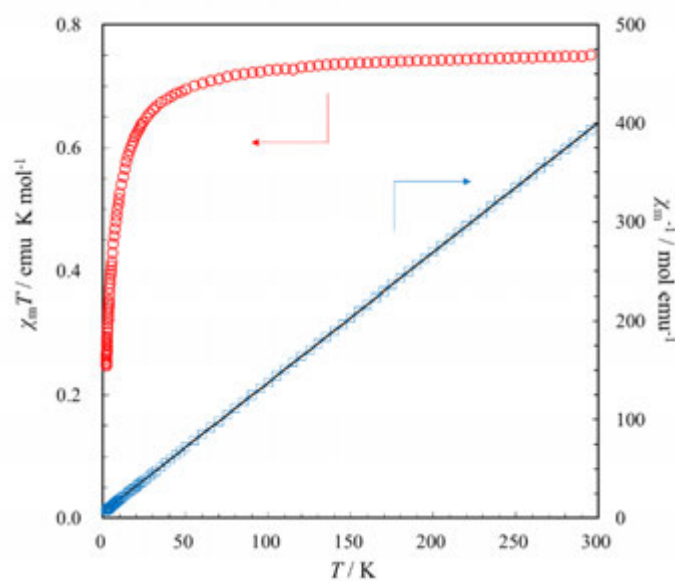


Figure 4-9. The temperature dependence of $\chi_m T$ (\circ) and χ_m^{-1} (\square) for polycrystalline sample of **PONN- β** . The solid line is best-fit result of the Curie-Weiss law. [*ChemPhysChem*, **2018**, *19*, 175.] - Copyright 2018, Wiley-VCH Verlag GmbH and Co. KGaA. Reproduced with permission.

4.5. Evaluation of Magnetic Interaction Based on Computation

To estimate the SOMO and spin density distributions, single point calculation using crystallographic coordinate were carried out with DFT method (UB3LYP/6-31G(d) level) in Gaussian 09 program.⁵

The SOMO and spin density of **POVZ** and **PONN- β** are shown in Figure 4-10. The SOMO of both spin centers distributed on each radical site like parent radicals. It suggested that intramolecular magnetic interaction was not derived from orbital-orbital interaction. In contrast, spin density of both biradical distributed over the molecule. The magnitude of intramolecular interaction was estimated by Yamaguchi's equation (equation 2-1).⁶ The estimated $2J$ values were $+19.5 \text{ cm}^{-1}$ for **POVZ** and $+20.6 \text{ cm}^{-1}$ for **PONN- β** , suggesting intramolecular ferromagnetic interaction (Tables 4-3, 4-4, Figures 4-11, 12). For **PONN- α** , the $2J = +21.2 \text{ cm}^{-1}$ for intramolecular magnetic interaction and -9.5 cm^{-1} for intermolecular magnetic interaction were estimated, whereas small intermolecular interaction in **PONN- β** (Table 4-5, Figure 4-13).

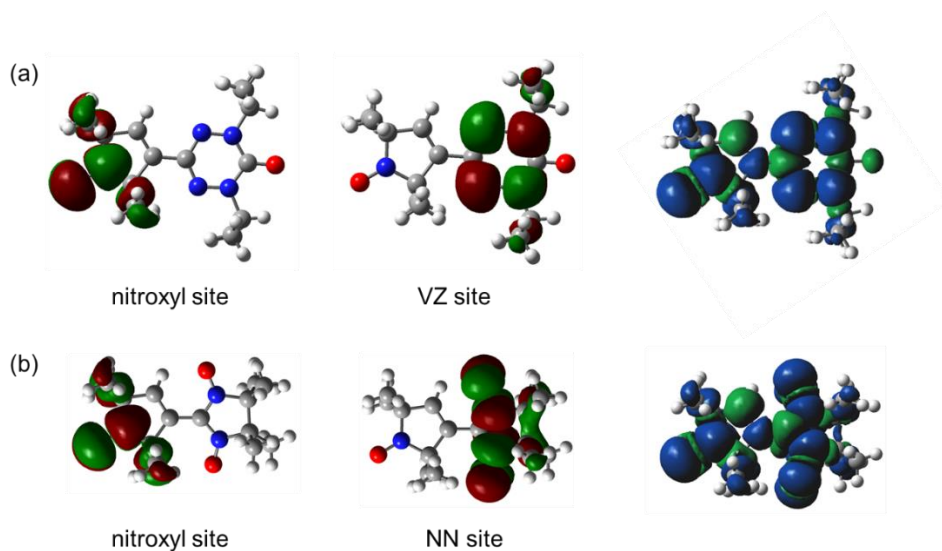


Figure 4-10. The SOMO and spin density of (a) **POVZ** and (b) **PONN** at UB3LYP/6-31G(d) level. [*ChemPhysChem*, **2018**, *19*, 175.] - Copyright 2018, Wiley-VCH Verlag GmbH and Co. KGaA. Reproduced with permission.

Table 4-3. Calculation results of magnetic interaction of **POVZ** at UB3LYP/6-31G(d) level.

Contacts	Energy(BS/T) / a.u.	$\langle S^2 \rangle$ (BS/T)	$2J/\text{cm}^{-1}$
Intramolecular	-1049.6640311 / -1049.6640756	1.028461 / 2.028268	+19.5
Intramolecular(UBLYP/6-31G(d))	-1049.1726874 / -1049.1727314	1.009559 / 2.010015	+19.3
Pair A	-1950.1841788 / -1950.1841784	1.049290 / 2.049309	-0.17
Pair B	-2025.3318676 / -2025.3318700	1.028511 / 2.028534	+1.06
Pair C	-2100.4787029 / -2100.4787007	1.007524 / 2.028534	-0.96

Calculation condition: The calculations of intermolecular magnetic interaction were carried out with the replacement of O atom of the selected nitroxide with H atom (pink circles in Figure 4-11).

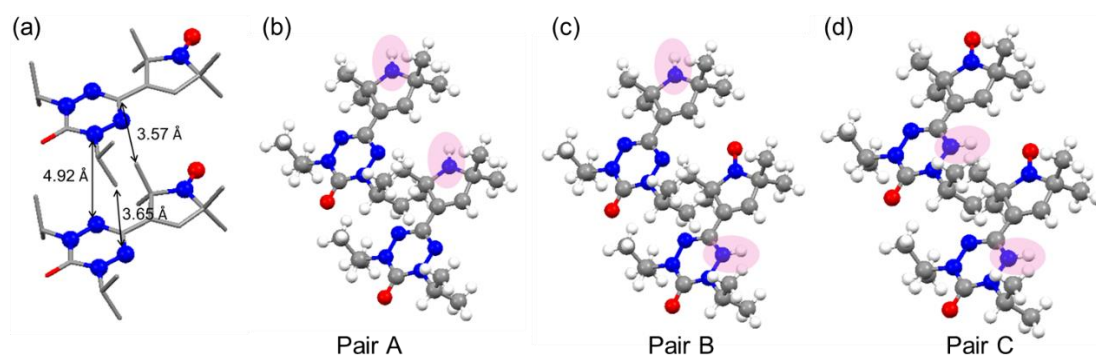


Figure 4-11. (a) The selected distances between the atoms within the column of **POVZ**. (b)(c)(d) The molecular contacts in columnar structure of **POVZ** for the computational study. [*ChemPhysChem*, **2018**, *19*, 175.] - Copyright 2018, Wiley-VCH Verlag GmbH and Co. KGaA. Reproduced with permission.

Table 4-4. Calculation results of magnetic interaction of **PONN- β** at UB3LYP/6-31G(d) level.

Contacts	Energy(BS/T) / a.u.	$\langle S^2 \rangle$ (BS/T)	$2J / \text{cm}^{-1}$
Intramolecular	-976.0169505 / -976.0169973	1.069356 / 2.069048	+20.6
Intramolecular(UBLYP/6-31G(d))	-975.5734909 / -975.5735148	1.013850 / 2.017240	+10.5
Pair A(a)	-1802.8929095 / -1802.8929106	1.125190 / 2.125214	+0.48
Pair A(b)	-1727.7169168 / -1727.7169139	1.066054 / 2.066153	-1.28
Pair B(a)	-1727.7171811 / -1727.7171810	1.068070 / 2.068080	-0.04
Pair B(b)	-1802.8882670 / -1802.8882669	1.128691 / 2.128688	-0.04

Calculation condition: The calculations of intermolecular magnetic interaction were carried out with the replacement of O atom of the selected nitroxide with H atom (pink circles in Figure 4-12).

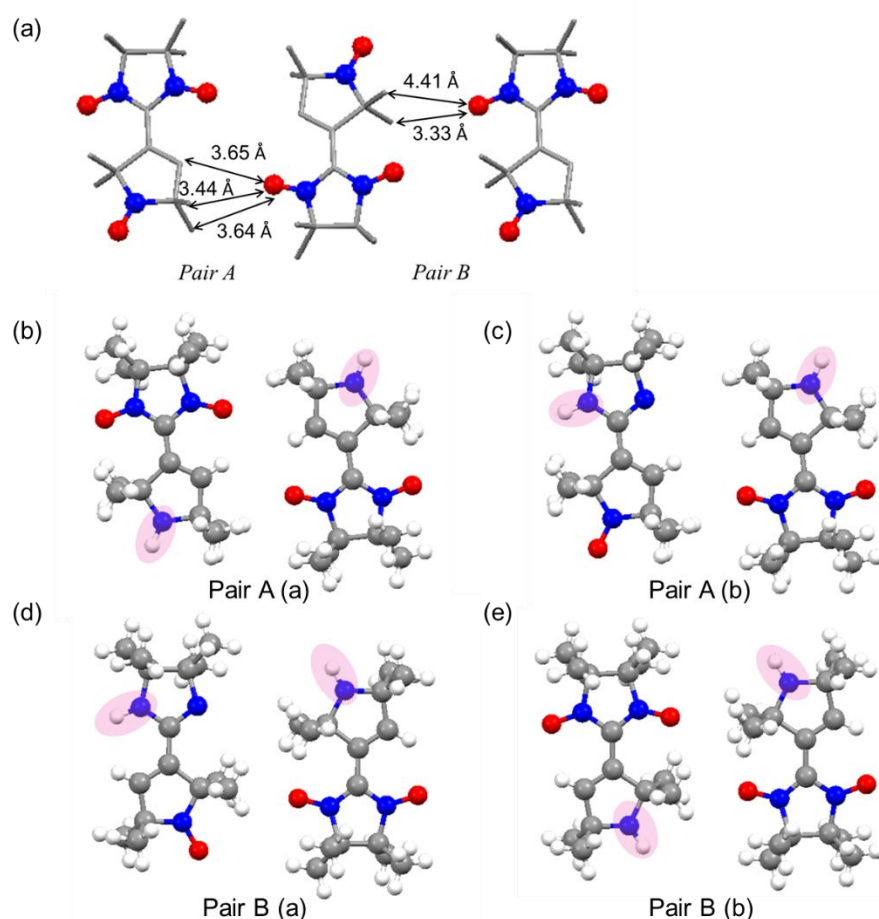


Figure 4-12. (a) The selected distances between the atoms within the column of **PONN- β** . (b)(c)(d)(e) The molecular contacts in columnar structure of **PONN- β** for the computational study. [ChemPhysChem, 2018, 19, 175.] - Copyright 2018, Wiley-VCH Verlag GmbH and Co. KGaA. Reproduced with permission.

Table 4-5. Calculation result of magnetic interaction of **PONN- α** at UB3LYP/6-31G(d) level.

Contacts	Energy(BS/T) / a.u.	$\langle S^2 \rangle$ (BS/T)	$2J/\text{cm}^{-1}$
Intramolecular	-976.0166071 / -976.0166553	1.066614 / 2.066317	+21.2
Intramolecular(UBLYP/6-31G(d))	-975.5734239 / -975.5734641	1.015709 / 2.016699	+17.7
Pair A	-1802.8880976 / -1802.8880759	1.123240 / 2.123848	-9.5
Pair B	-1802.8970846 / -1802.8970771	1.120138 / 2.120310	-3.29

Calculation condition: The calculations of intermolecular magnetic interaction were carried out with the replacement of O atom of the pyrroline *N*-oxyl by H atom.

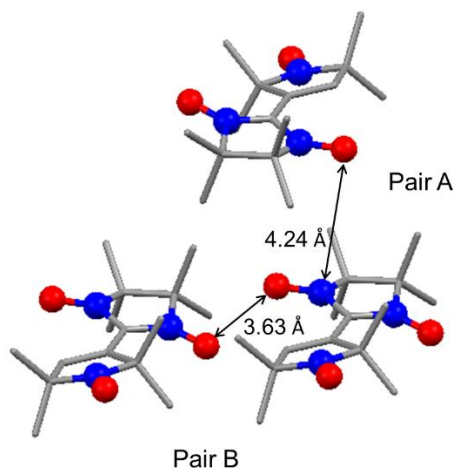


Figure 4-13. The molecular contacts of **PONN- α** . [*ChemPhysChem*, **2018**, *19*, 175.] - Copyright 2018, Wiley-VCH Verlag GmbH and Co. KGaA. Reproduced with permission.

To reveal the mechanism of intramolecular interaction in the viewpoint of spin density, the spin density of pyrroline *N*-oxyl attached verdazyl and nitronyl nitroxide radical **POVZ'** and **PONN'** were calculated at UB3LYP/6-31G(d) level (Figure 4-14). Regarding the $\text{C}(\text{CH}_3)_2$ moiety, the sign of spin density alternates $\text{C3}(\uparrow)\text{-C4}(\downarrow)\text{-C7}$ and $\text{C8}(\uparrow)$, and $\text{C2}(\downarrow)\text{-C1}(\uparrow)\text{-C5}$ and $\text{C6}(\downarrow)$. There is larger β spin on C2 than α spin on C3 of vinylic moiety. Considering spin density of pyrroline *N*-oxyl, the sign of spin density alternates O1 and $\text{N1}(\uparrow)\text{-C1}$ and $\text{C4}(\downarrow)\text{-C2}$ and $\text{C3}(\uparrow)$. For **POVZ**, there is similar spin density $\text{C3}(\uparrow)\text{-C2}(\downarrow)$ on vinylic moiety due to small spin polarization from pyrroline *N*-oxyl site (Figure 4-15(c)). Because of larger β spin on C2, intramolecular antiferromagnetic interaction was preferred, which is conflict with the experimental result. Therefore, spin-spin interaction dominant

their intramolecular magnetic interaction and ferromagnetic interaction was preferred due to the contact of different sign of spin density. Regarding **PONN**, intramolecular ferromagnetic interaction will be expected in the same mechanism, however, intermolecular antiferromagnetic interaction may prevent the observation of ferromagnetic interaction.

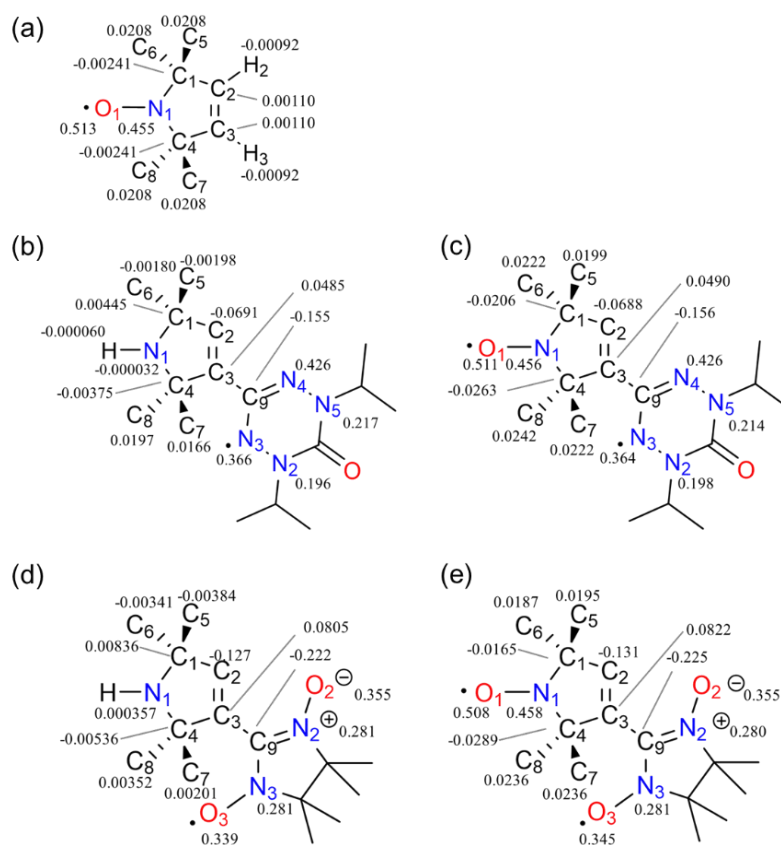


Figure 4-14. Spin density of (a) pyrroline *N*-oxyl, (b) **POVZ'**, (c) **POVZ**, (d) **PONN'** and (e) **PONN** at UB3LYP/6-31G(d) level. The computations were carried out using the optimized geometry. [ChemPhysChem, 2018, 19, 175.] - Copyright 2018, Wiley-VCH Verlag GmbH and Co. KGaA. Reproduced with permission.

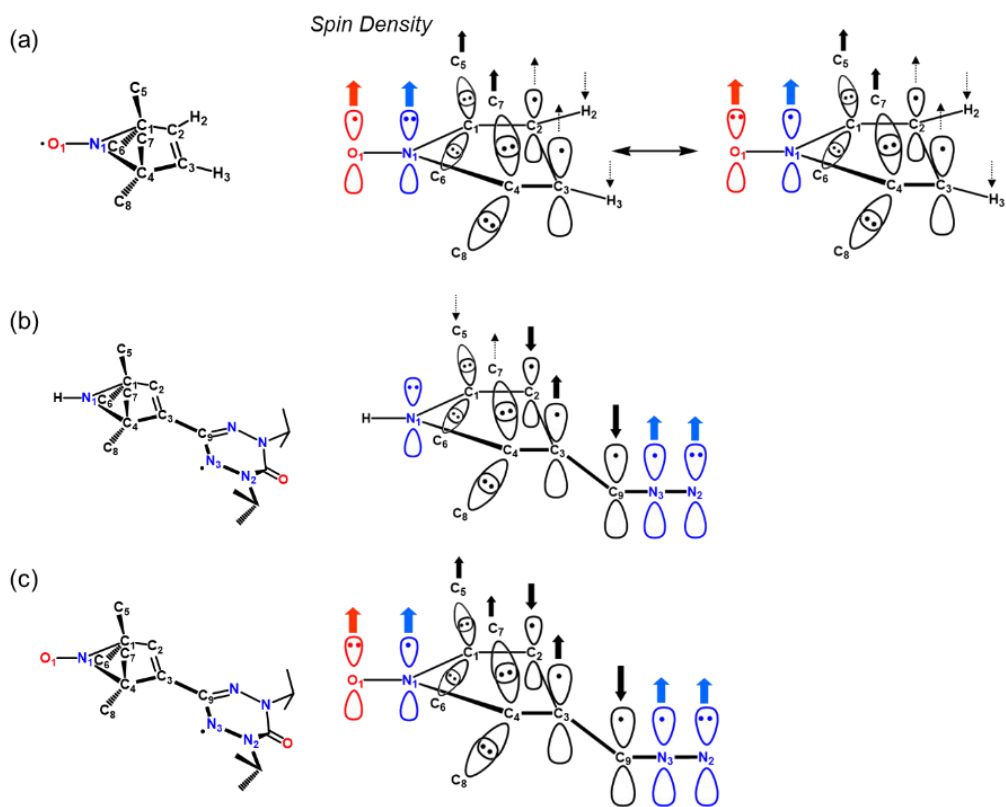


Figure 4-15. Schematic illustration of spin density of (a) pyrroline *N*-oxyl, (b) **POVZ'**, (c) **POVZ**. [*ChemPhysChem*, **2018**, *19*, 175.] - Copyright 2018, Wiley-VCH Verlag GmbH and Co. KGaA. Reproduced with permission.

4.6. ESR Measurement

The ESR spectra of **POVZ** and **PONN** in toluene at room temperature are shown in Figure 4-16. The broad spectra were observed due to the non-averaged dipole-dipole interaction of whole molecules and slow rotation of radical moieties. The spectra in toluene glass matrix at 3.5 K are shown in Figure 4-17. In $g = 2$ region, the spectra exhibited fine structure because of zero field splitting. The signal observed at center is attributed to the corresponding monoradical impurities. The D values are estimated from the most outer signal ($2D = 33.1$ mT for **POVZ** and 31.7 mT for **PONN**) and E value of **PONN** is estimated from second outer split signal (0.29 mT), however E value of **POVZ** cannot be estimated due to complex splits. The point-dipole approximation gave the spin-spin distance (**POVZ**: 5.52 Å, **PONN**: 5.61 Å), which is shorter than the distance between the pyrroline nitroxide site and attached radical site due to the delocalization of unpaired electron. In addition, half field signals of $\Delta m_s = \pm 2$ were observed in $g = 4$ region. The curie plots of **POVZ** and **PONN** are shown in Figure 4-18. The linear relationship between intensity of $g = 4$ and reciprocal temperature are observed, revealing that **POVZ** and **PONN** have ground triplet state (Figure 4-18).

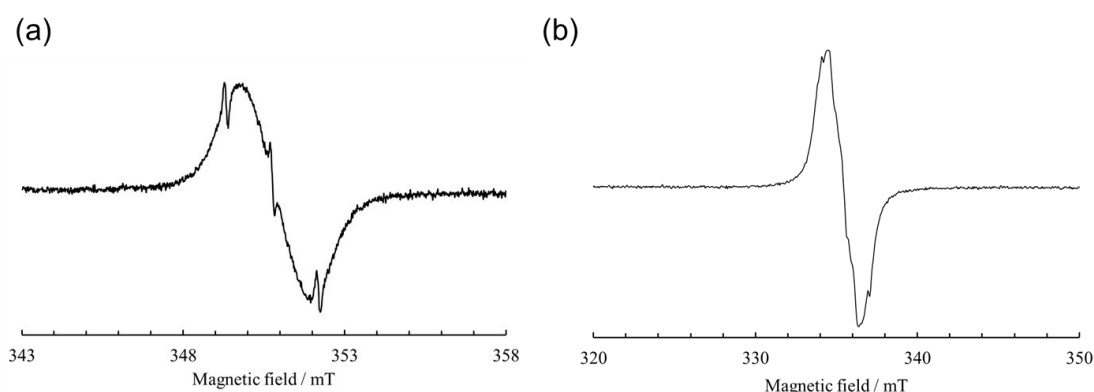


Figure 4-16. ESR spectra of $\Delta m_s = \pm 1$ signal for (a) **POVZ** and (b) **PONN** in toluene at room temperature. [*ChemPhysChem*, **2018**, *19*, 175.] - Copyright 2018, Wiley-VCH Verlag GmbH and Co. KGaA. Reproduced with permission.

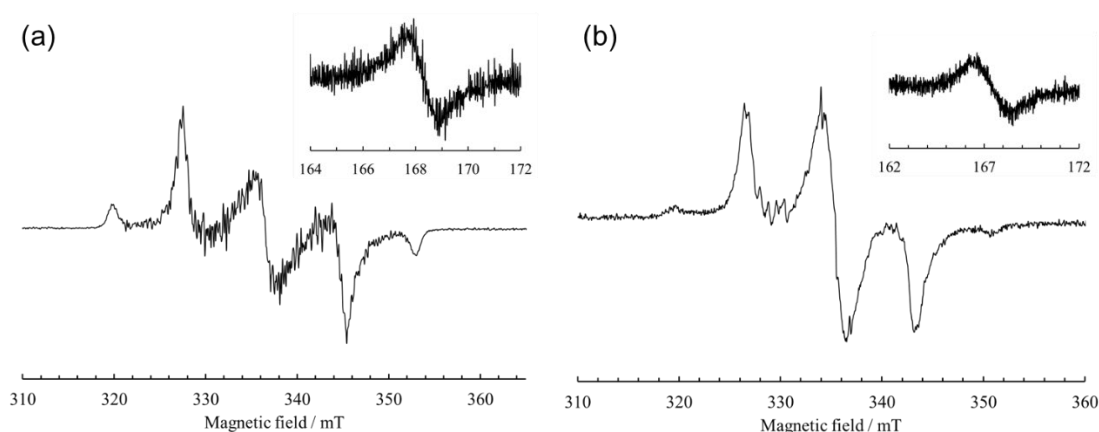


Figure 4-17. ESR spectra of $\Delta m_s = \pm 1$ signal for (a) **POVZ** and (b) **PONN** in toluene glass matrix at 3.5 K. Inset represents the half field signal of $\Delta m_s = \pm 2$. [*ChemPhysChem*, **2018**, *19*, 175.] - Copyright 2018, Wiley-VCH Verlag GmbH and Co. KGaA. Reproduced with permission.

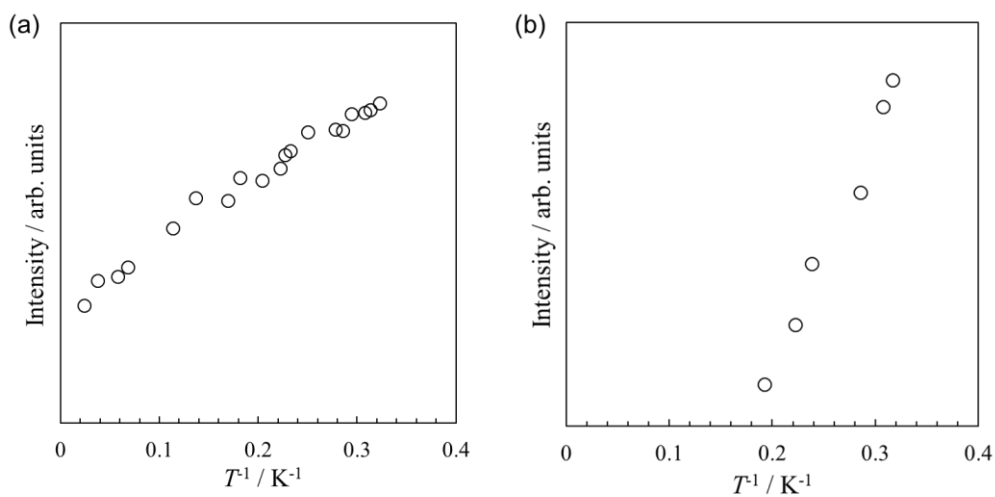


Figure 4-18. Temperature dependence of signal intensity of $\Delta m_s = \pm 2$ signal for $g = 4$ region. (a) **POVZ** and (b) **PONN** in toluene glass matrix. [*ChemPhysChem*, **2018**, *19*, 175.] - Copyright 2018, Wiley-VCH Verlag GmbH and Co. KGaA. Reproduced with permission.

References in Chapter 4

1. (a) M.-C. Frantz, E. M. Skoda, J. R. Sacher, M. W. Epperly, J. P. Goff, J. S. Greenberger, P. Wipf, *Org. Biomol. Chem.*, **2013**, *11*, 4147.
(b) E. Mileo, E. Etienne, M. Martinho, R. Lebrun, V. Roubaud, P. Tordo, B. Gontero, B. Guigliarelli, S. R. A. Marque, V. Belle, *Bioconjugate Chem.*, **2013**, *24*, 1110.
2. T. Kálai, J. Jekő, Z. Szabó, L. Párkányi, K. Hideg, *Synthesis*, **1997**, 1049.
3. R. Gupta, in *Landolt-Börnstein New Series Group II* (Eds. K. -H. Hellwege and A. M. Hellwege), Springer, Berlin, Germany, 1986, Vol. 16, ch. 1.2.
4. B. Bleaney, K. D. Bowers, *Proc. R. Soc. London, Ser. A*, **1952**, *214*, 451.
5. Gaussian 09: Revision D.01, M. J. Frisch, G. W. Trucks, H. B. Schlegel, G. E. Scuseria, M. A. Robb, J. R. Cheeseman, G. Scalmani, V. Barone, B. Mennucci, G. A. Petersson, H. Nakatsuji, M. Caricato, X. Li, H. P. Hratchian, A. F. Izmaylov, J. Bloino, G. Zheng, J. L. Sonnenberg, M. Hada, M. Ehara, K. Toyota, R. Fukuda, J. Hasegawa, M. Ishida, T. Nakajima, Y. Honda, O. Kitao, H. Nakai, T. Vreven, J. A. Montgomery, Jr., J. E. Peralta, F. Ogliaro, M. Bearpark, J. J. Heyd, E. Brothers, K. N. Kudin, V. N. Staroverov, R. Kobayashi, J. Normand, K. Raghavachari, A. Rendell, J. C. Burant, S. S. Iyengar, J. Tomasi, M. Cossi, N. Rega, J. M. Millam, M. Klene, J. E. Knox, J. B. Cross, V. Bakken, C. Adamo, J. Jaramillo, R. Gomperts, R. E. Stratmann, O. Yazyev, A. J. Austin, R. Cammi, C. Pomelli, J. W. Ochterski, R. L. Martin, K. Morokuma, V. G. Zakrzewski, G. A. Voth, P. Salvador, J. J. Dannenberg, S. Dapprich, A. D. Daniels, Ö. Farkas, J. B. Foresman, J. V. Ortiz, J. Cioslowski, D. J. Fox, Gaussian, Inc., Wallingford CT, 2009.
6. K. Yamaguchi, H. Fukui, T. Fueno, *Chem. Lett.*, **1986**, 625.

Chapter 5: Computational Study of Magnetic Interaction through Non-Conjugated Framework

5.1. Introduction

As described in chapter 3 and 4, the magnetic interaction through non-conjugated framework attributed to intramolecular SOMO-SOMO and spin-spin interaction was observed in hetero biradicals carrying pyrroline *N*-oxyl skeleton. In chapter 5, to estimate the magnetic interaction through pyrroline skeleton, several computations were carried out and improved molecular design for construction of ground triplet biradical carrying cyclic nitroxyl radical was described. Calculations were carried out using Gaussian 09 program.¹

5.2. Correlation between the Spin Density on Vinylic Moiety and Magnetic Interaction

As described in chapter 4, the DFT calculation of model compounds **POA1** and **POA2** revealed that the spin density distribution on vinylic carbons affected the sign of magnetic interaction. To estimate the correlation between the spin density on vinylic moiety and the magnitude of intramolecular magnetic interaction, the computations using optimized geometry of **POA1** were carried out with changing every 15 degrees of the dihedral angle between pyrroline ring and attached radical (Figure 5-1(a), Table 5-1). The magnitude of magnetic interaction of **POA1** was $2J = +27.4$ cm⁻¹ at 0° and was decreased with enlarge the dihedral angle. When there was larger β spin density on vinylic carbon, intramolecular ferromagnetic interaction was estimated, whereas antiferromagnetic interaction in the case of larger α spin. The similar trend was observed in each **POVZ** and **PONN** systems (Figures 5-1(b, c), Tables 5-2, 5-3). Thus, the balance of α and β spin densities on vinylic moiety affected the sign of intramolecular magnetic interaction and the large difference between α and β spin densities produce large $2J$ value.

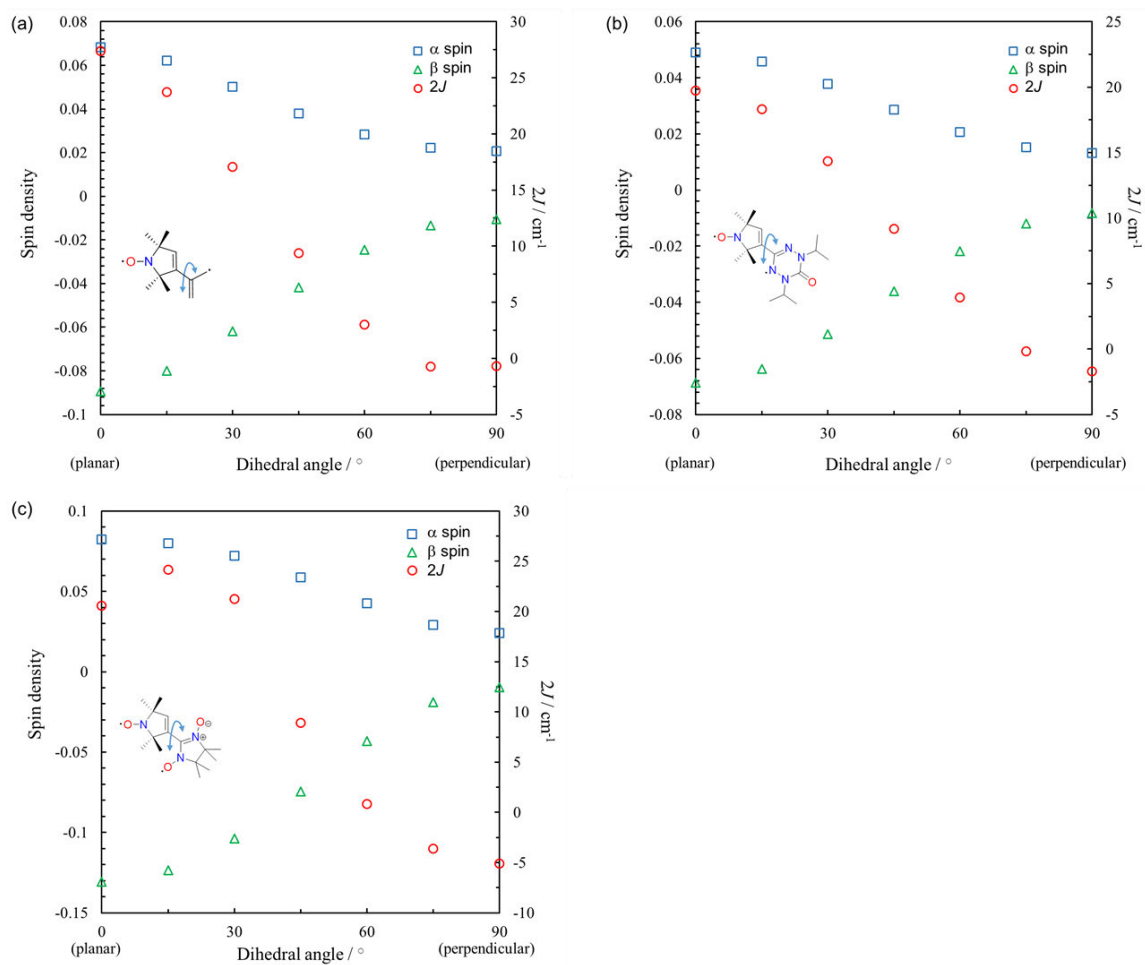


Figure 5-1. The correlation between the dihedral angle and spin density and $2J$ value for (a) **POA1**, (b) **POVZ** and (c) **PONN** at UB3LYP/6-31G(d) level. [*ChemPhysChem*, **2018**, *19*, 175.] - Copyright 2018, Wiley-VCH Verlag GmbH and Co. KGaA. Reproduced with permission.

Table 5-1. The spin density and $2J$ value of **POA1** with several dihedral angles.

Dihedral angle / °	Spin density on vinylic carbons		$2J / \text{cm}^{-1}$
	Positive spin	Negative spin	
0	0.068245	-0.089388	+27.4
15	0.062068	-0.080030	+23.7
30	0.050201	-0.061875	+17.1
45	0.037907	-0.041761	+9.39
60 ^a	0.028219	-0.024538	+3.03
75	0.022185	-0.013389	-0.75
90	0.020627	-0.010614	-0.70

Table 5-2. The spin density and $2J$ value of **POVZ** with several dihedral angles.

Dihedral angle / °	Spin density on vinylic carbons		$2J / \text{cm}^{-1}$
	Positive spin	Negative spin	
0	0.049012	-0.068756	+19.7
15	0.045726	-0.063827	+18.3
30	0.037780	-0.051384	+14.3
45	0.028608	-0.036054	+9.17
60	0.020616	-0.021881	+3.95
75	0.015160	-0.011900	-0.18
90	0.013195	-0.008295	-1.71

Table 5-3. The spin density and $2J$ value of **PONN** with several dihedral angles.

Dihedral angle / °	Spin density on vinylic carbons		$2J / \text{cm}^{-1}$
	Positive spin	Negative spin	
0	0.082229	-0.130769	+20.6
15	0.079842	-0.123518	+24.2
30	0.072020	-0.103703	+21.2
45	0.058662	-0.074524	+8.91
60	0.042555	-0.043138	+0.84
75	0.029268	-0.019058	-3.60
90	0.023934	-0.009740	-5.09

5.3. Distance Dependency on Pyrroline Ring for Magnetic Interaction

The SOMO-SOMO and spin-spin interaction attributed to the intramolecular magnetic interaction in pyrroline *N*-oxyl hetero biradicals. The magnitude of spin-spin interaction depends on the distance between the spin site. In the point of this view, the relationship of the distance between nitrogen atom of nitroxyl moiety and vinylic carbons with the $2J$ value was estimated (Figure 5-2). For **3PPO**, spin-spin interaction was preferred under 2.45 Å and antiferromagnetic interaction was estimated. Over 2.50 Å, the sign of $2J$ value was inverted to positive, suggesting that through-bond interaction was preferred. In the case of **POVZ**, the $2J$ value was decreased with increasing the distance and close to zero. Therefore, for pyrroline *N*-oxyl hetero biradical system, the magnitude of through-space interaction was decreased and through-bond interaction was preferred in the case of large distance.

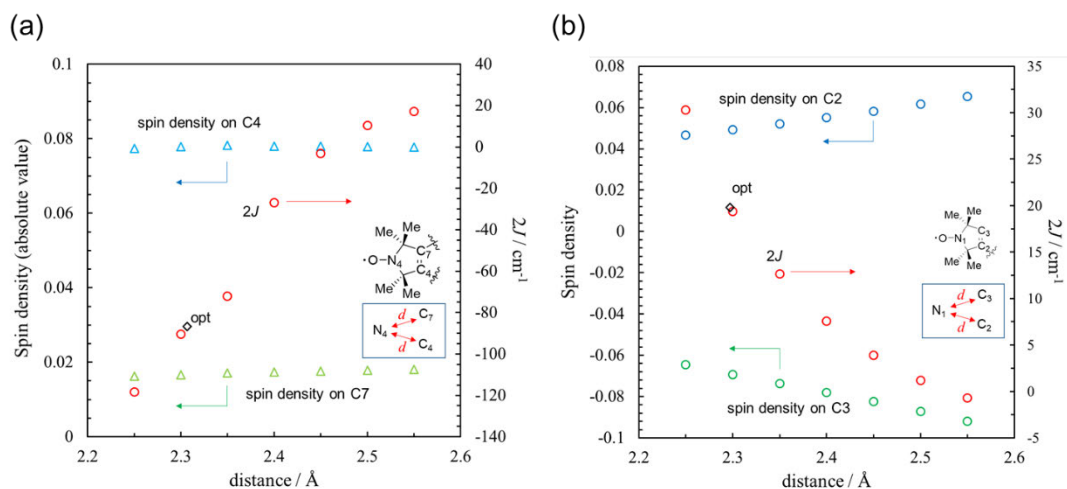


Figure 5-2. The correlation of the distance between nitrogen atom of nitroxyl moiety and vinylic carbons with the $2J$ value for (a) **3PPO** and (b) **POVZ** at UB3LYP/6-31G(d) level.

Table 5-4. The spin density and $2J$ value of **3PPO** with several distances.

Distance / Å	Spin density on vinylic carbons		$2J / \text{cm}^{-1}$
	C7	C4	
2.25	0.077388	0.016257	-118.4
2.30	0.077863	0.016664	-90.4
2.35	0.078272	0.017166	-72.0
2.40	0.077951	0.017392	-26.9
2.45	0.07794	0.017598	-3.08
2.50	0.07784	0.017841	+10.5
2.55	0.077732	0.018039	+17.1

Table 5-5. The spin density and $2J$ value of **POVZ** with several distances.

Distance / Å	Spin density on vinylic carbons		$2J / \text{cm}^{-1}$
	C2	C3	
2.25	0.046652	-0.064451	+30.3
2.30	0.049345	-0.069345	+19.4
2.35	0.052089	-0.073663	+12.6
2.40	0.055033	-0.077971	+7.59
2.45	0.058238	-0.082423	+3.91
2.50	0.061712	-0.087073	+1.18
2.55	0.06546	-0.091955	-0.70

5.4. Substituent Effect on Methyl Group

The spin density on tetramethyl groups was mainly derived from nitroxyl moiety and these methyl groups attributed to intramolecular magnetic interaction. To estimate the contribution of substituent effect, the $2J$ values of several model derivatives carrying H, Ph, *tert*-Bu and F atoms instead of methyl groups were evaluated (Table 5-6). All derivatives exhibited intramolecular antiferromagnetic interaction and the magnitude was in the range of -85 to -160 cm^{-1} except for fluorine introduced compound. In the case of fluorine introduced derivative, the existence of large spin density on fluorine atoms due to their large electron negativity, leading strong intramolecular antiferromagnetic interaction.

Table 5-6. Calculation results of intermolecular magnetic interaction of **3PPO** analogues.

R	Energy(BS/T) / a.u.	$\langle S^2 \rangle$ (BS/T)	$2J / \text{cm}^{-1}$
CH ₃ (3PPO)	-1261.2659061 / -1261.2657097	1.018128 / 2.020440	-86.8
H	-1103.9947988 / -1103.9946052	1.012016 / 2.020081	-85.6
Ph	-1452.9962114 / -1452.9959782	1.012631 / 2.020450	-103.2
<i>tert</i> -Bu	-1732.9074740 / -1732.9071168	1.009644 / 2.020932	-158.6
F	-1500.9429622 / -1500.9403714	0.959632 / 2.018816	-1204.4

5.5. Rotation Effect on Methyl Group

Generally, the methyl group was rotated in solid state and this behavior have been investigated by spectroscopic study.² Considering pyrroline *N*-oxyl hetero biradical system, rotation of methyl group may attribute to intramolecular magnetic interaction. The computation was carried out using the optimized geometry of **3PPO** and **3BPO** as basic skeleton (Tables 5-7, 5-8). The dihedral angle ϕ was defined as the angle of C-H bond of methyl group with N-C bond of pyrroline ring, as shown in Figure 5-3(a). For **3BPO**, when the hydrogen atom was placed at perpendicular position against pyrroline plane ($\phi = 60^\circ$), the $2J$ value was -89.9 cm^{-1} and was decreased with increasing the dihedral angle (Figure 5-3(b)). The $2J$ value was reached -142.3 cm^{-1} at 120° and was increased with increased the dihedral angle and was taken the initial value (-99.2 cm^{-1}) at 180° . Therefore, the rotation of methyl group attribute to the intramolecular magnetic interaction. Without considering the weighting for the place of hydrogen atoms of methyl group, averaged $2J$ value of **3BPO** using optimized structure was -117.5 cm^{-1} . For **3PPO**, it exhibited the same tendency of **3BPO**.

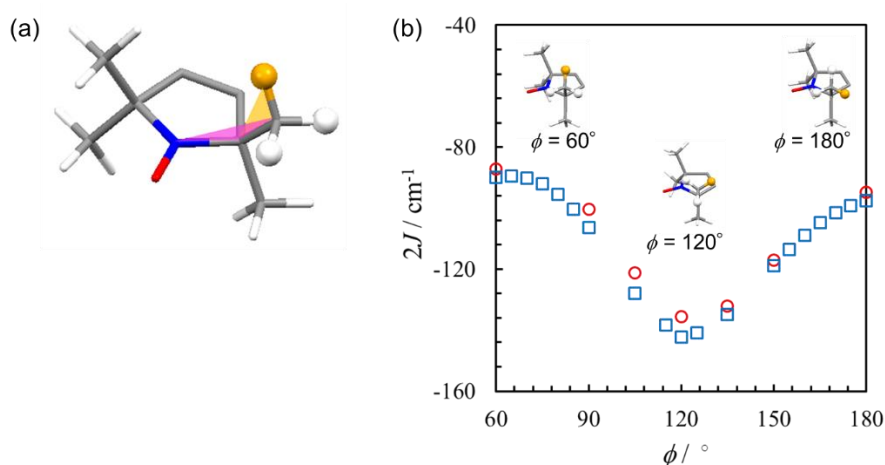


Figure 5-3. (a) The define of dihedral angle ϕ for **3PPO**. (b) The correlation between dihedral angle ϕ and $2J$ value for **3PPO** (\circ) and **3BPO** (\square).

Table 5-7. Calculation results of intermolecular magnetic interaction of **3PPO** with several dihedral angles ϕ .

$\phi / ^\circ$	Energy(BS/T) / a.u.	$\langle S^2 \rangle$ (BS/T)	$2J / \text{cm}^{-1}$
60	-1261.2658508 / -1261.2656535	1.013532 / 2.020438	-87.2
90	-1261.2536105 / -1261.2533837	1.012697 / 2.020540	-100.3
105	-1261.2435383 / -1261.2432649	1.011522 / 2.020622	-121.1
120	-1261.2386775 / -1261.2383716	1.010732 / 2.020649	-135.6
135	-1261.2419926 / -1261.2416945	1.010922 / 2.020587	-132.1
150	-1261.2512894 / -1261.2510250	1.011782 / 2.020490	-117.1
180	-1261.2653730 / -1261.2651584	1.013118 / 2.020418	-94.5

Table 5-8. Calculation results of intermolecular magnetic interaction of **3BPO** with several dihedral angles ϕ .

$\phi / ^\circ$	Energy(BS/T) / a.u.	$\langle S^2 \rangle$ (BS/T)	$2J / \text{cm}^{-1}$
60	-1187.4654599 / -1187.4652565	1.011459 / 2.018558	-89.9
65	-1187.4650026 / -1187.4648003	1.011476 / 2.018563	-89.4
70	-1187.4636614 / -1187.4634576	1.011420 / 2.018573	-90.1
75	-1187.4615225 / -1187.4613142	1.011284 / 2.018589	-92.1
80	-1187.4587177 / -1187.4585019	1.011069 / 2.018609	-95.4
85	-1187.4554318 / -1187.4552052	1.010777 / 2.018635	-100.2
90	-1187.4518841 / -1187.4516440	1.010418 / 2.018663	-106.3
105	-1187.4421243 / -1187.4418359	1.009205 / 2.018745	-127.8
115	-1187.4385899 / -1187.4382777	1.008632 / 2.018769	-138.4
120	-1187.4381740 / -1187.4378531	1.008507 / 2.018767	-142.3
125	-1187.4387072 / -1187.4383897	1.008506 / 2.018753	-140.8
135	-1187.4424056 / -1187.4421012	1.008835 / 2.018702	-134.9
150	-1187.4520760 / -1187.4518075	1.009765 / 2.018610	-118.9
155	-1187.4555151 / -1187.4552584	1.010922 / 2.018586	-113.5
160	-1187.4586744 / -1187.4584284	1.010371 / 2.018568	-108.9
165	-1187.4613488 / -1187.4611119	1.010618 / 2.018555	-104.8
170	-1187.4633673 / -1187.4631377	1.010817 / 2.018547	-101.6
175	-1187.4645986 / -1187.4643744	1.010960 / 2.018543	-99.2
180	-1187.4649634 / -1187.4647426	1.011043 / 2.018544	-97.6

5.6. Improved Molecular Design for Ground Triplet Biradical Carrying Non-Conjugated Framework

As described, intramolecular magnetic interaction of pyrroline *N*-oxyl hetero biradicals was mainly derived from the SOMO-SOMO and the spin-spin interaction, however, through-bond interaction was preferred when there is the distance between nitrogen atom of nitroxyl moiety and vinylic carbons. To utilize the through-bond interaction, the author focused tetramethylazaphenylene *N*-oxyl, denoted as **TMAO**. There is the 6-membered ring around the nitroxyl moiety and this ring was fused in naphthalene ring. Its calculated SOMO and spin density distribution using the optimized structure was shown in Figure 5-4, which are similar to that of pyrroline *N*-oxyl. The SOMO distributed over nitroxyl and tetramethyl moiety. The spin density mainly distributed on nitroxyl and tetramethyl moiety and slightly distribute on naphthalene ring. The distance between nitrogen atom of nitroxyl moiety and naphthalene ring is *ca.* 2.47 Å, which is enough to get rid of through-space interaction and through-bond interaction may be preferred. In addition, the intramolecular magnetic interaction may also be described in the spin polarization mechanism. To evaluate the correlation between the spin density distribution on naphthalene ring and the sign of magnetic interaction, several model compounds were designed and their magnetic interaction was calculated.

For **TMAO** biradicals carrying nitronyl nitroxide at 6- or 7-position, spin density could distribute on naphthalene ring due to spin polarization from nitronyl nitroxide, however, SOMO of nitronyl

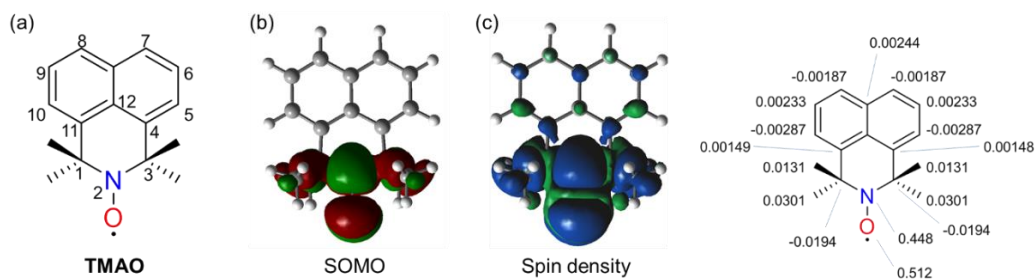


Figure 5-4. (a) Molecular structure, (b) SOMO and (c) spin density (isovalue 0.00013) distributions of **TMAO** at UB3LYP/6-31G(d) level.

nitroxide didn't distribute on naphthalene ring (Figure 5-5). Regarding spin density distribution, spin densities on carbon atoms at 4- and 11 positions were arising from spin polarization of nitronyl nitroxide and there were positive spins for **6NNTMAO** whereas negative spin for **7NNTMAO**. According to the spin polarization, there are ferromagnetic coupling in **6NNTMAO** and antiferromagnetic coupling in **7NNTMAO**, which supported by positive and negative J values, respectively (Table 5-9).

In the case of delocalization of SOMO derived from attached spin center on naphthalene ring, larger magnetic interaction will be estimated. Several examples were shown in Figure 5-6. When odd-alternant carbon type radicals are attached, the sign of spin density distributed on carbon atoms at 4- and 11 positions can be predicted by spin polarization. In particular, phenalenyl and diazaphenalenyl skeletons contained biradicals **TMAOPhe** and **TMAOazaPhe** will display strong ferromagnetic interaction with $2J = ca. +100 \text{ cm}^{-1}$ because those unpaired electrons are delocalized on carbon atoms at 4- and 11 positions (Tables 5-9, 5-10). In contrast, intramolecular small ferromagnetic interaction predicted in **TMAOBT** in spite of positive spin distribution on carbon atoms at 1- and 8 positions of TMAO moiety. Regarding spin density population, large positive spin population on carbon atom at 4 position lead strong ferromagnetic interaction (Table 5-10). Therefore, alternant hydrocarbon type biradical display large population of unpaired electrons on alternately atoms, resulting effective ferromagnetic coupling, whereas delocalization of unpaired electron lead decreasing the magnitude of magnetic interaction (Figure 5-7). In addition, the energy level of SOMOs in **TMAOazaPhe** was degenerated (nitroxyl site: -5.25 eV, phenalenyl site: -5.36 eV), whereas non-degenerated SOMOs in **TMAOBT** (nitroxyl site: -5.22 eV, benzotriazinyl site: -4.35 eV). Therefore, TMAO skeleton can play a role of LPOMO of spin center.

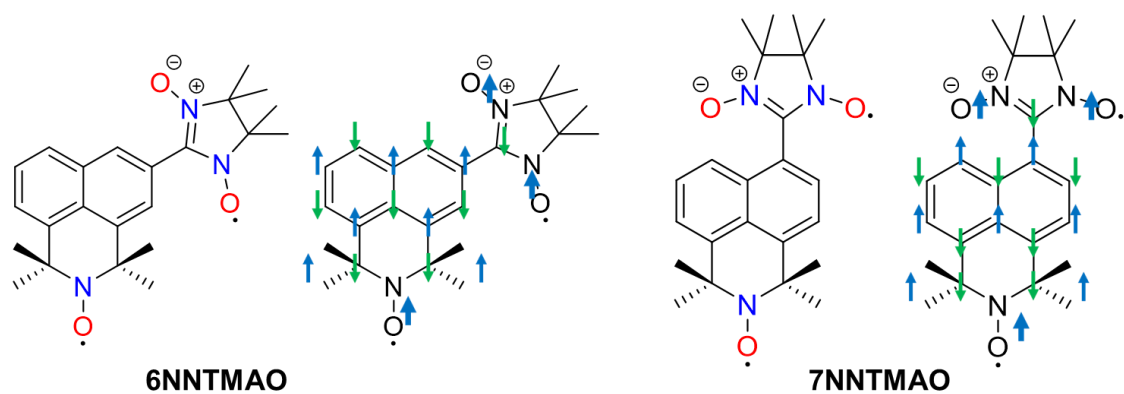


Figure 5-5. Schematic illustration of spin density for **6NNTMAO** and **7NNTMAO**.

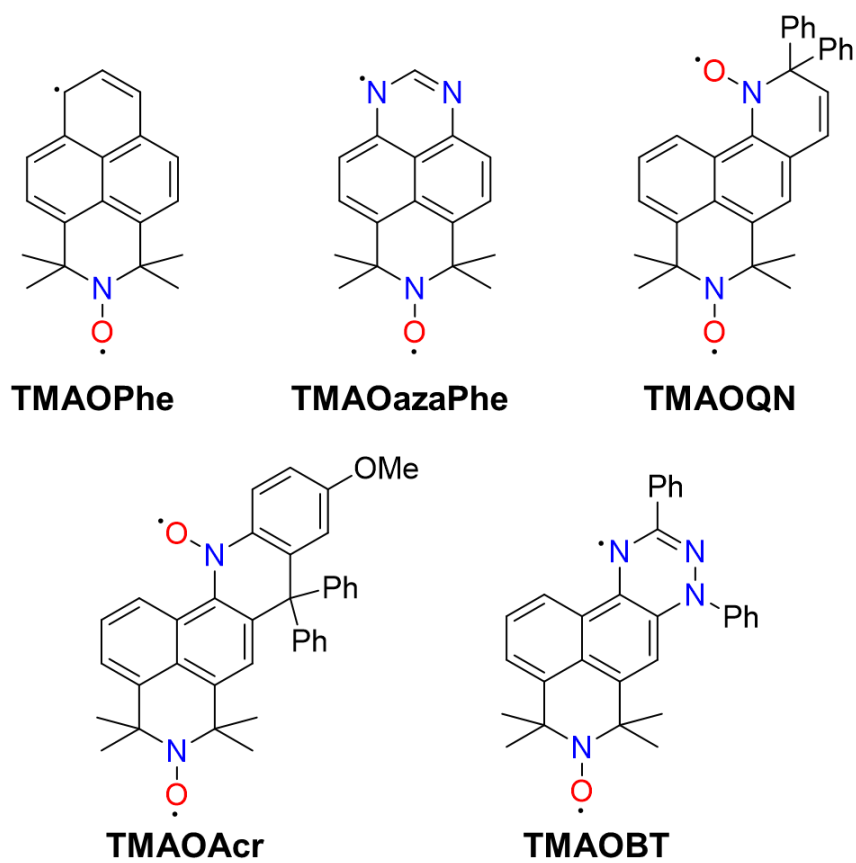


Figure 5-6. Molecular structures of biradicals for computation.

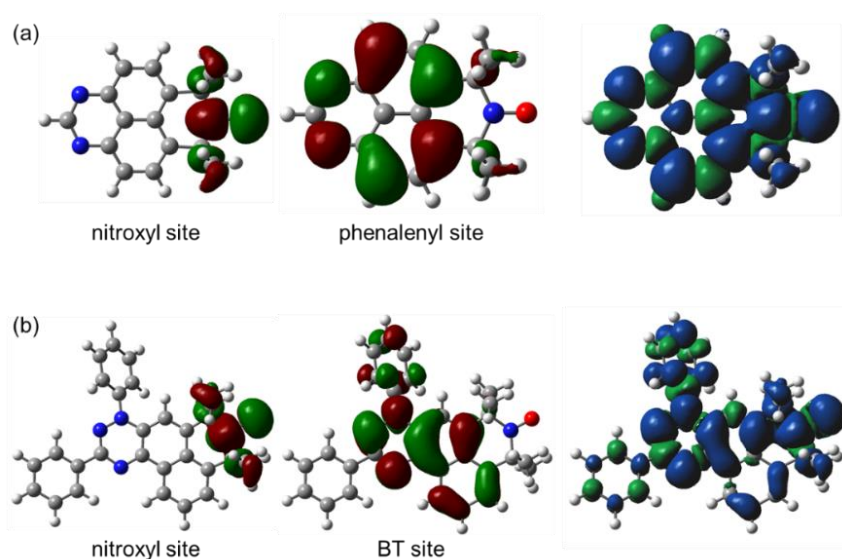


Figure 5-7. SOMO(left) and spin density(right) distributions of (a) **TMAOazaPhe** and (b) **TMAOBT**.

Table 5-9. The calculated J value for **TMAO** biradicals at UB3LYP/6-31G(d) level.

Compounds	Energy(BS/T) / a.u.	$\langle S^2 \rangle$ (BS/T)	$2J / \text{cm}^{-1}$
6NNTMAO	-1283.6830255 / -1283.6830524	1.067910 / 2.069046	+11.8
7NNTMAO	-1283.6734001 / -1283.6733858	1.059919 / 2.059294	-6.2
TMAOPhe	-865.3891314 / -865.3893591	1.052589 / 2.054228	+100.2
TMAOazaPhe	-897.4676360 / -897.4678798	1.045181 / 2.046647	+107.2
TMAOQN	-1457.9800075 / -1457.9801233	1.038389 / 2.040276	+51.0
TMAOAc	-1726.1516141 / -1726.1516899	1.022929 / 2.024229	+33.4
TMAOBT	-1414.9006682 / -1414.9006710	1.019321 / 2.021343	+1.2

Table 5-10. Selected spin density population for **TMAO** biradicals at UB3LYP/6-31G(d) level.

Compounds	N	O	C3	C4	C12	C11	C1	$2J / \text{cm}^{-1}$
6NNTMAO	0.447	0.512	-0.0210	0.0278	-0.0300	0.0200	-0.0203	+11.8
7NNTMAO	0.447	0.512	-0.0176	-0.0255	0.00931	-0.0052	-0.0019	-6.2
TMAOPhe	0.459	0.504	-0.0461	0.320	-0.147	0.321	-0.0462	+100.2
TMAOazaPhe	0.456	0.508	-0.0469	0.339	-0.152	0.339	-0.0469	+107.2
TMAOQN	0.447	0.511	-0.0320	0.201	-0.0759	0.0707	-0.0241	+51.0
TMAOAc	0.447	0.512	-0.0285	0.141	-0.0504	0.0449	-0.0222	+33.4
TMAOBT	0.448	0.513	-0.0263	0.114	-0.0097	0.0130	-0.0200	+1.2

References in Chapter 5

1. Gaussian 09: Revision D.01, M. J. Frisch, G. W. Trucks, H. B. Schlegel, G. E. Scuseria, M. A. Robb, J. R. Cheeseman, G. Scalmani, V. Barone, B. Mennucci, G. A. Petersson, H. Nakatsuji, M. Caricato, X. Li, H. P. Hratchian, A. F. Izmaylov, J. Bloino, G. Zheng, J. L. Sonnenberg, M. Hada, M. Ehara, K. Toyota, R. Fukuda, J. Hasegawa, M. Ishida, T. Nakajima, Y. Honda, O. Kitao, H. Nakai, T. Vreven, J. A. Montgomery, Jr., J. E. Peralta, F. Ogliaro, M. Bearpark, J. J. Heyd, E. Brothers, K. N. Kudin, V. N. Staroverov, R. Kobayashi, J. Normand, K. Raghavachari, A. Rendell, J. C. Burant, S. S. Iyengar, J. Tomasi, M. Cossi, N. Rega, J. M. Millam, M. Klene, J. E. Knox, J. B. Cross, V. Bakken, C. Adamo, J. Jaramillo, R. Gomperts, R. E. Stratmann, O. Yazyev, A. J. Austin, R. Cammi, C. Pomelli, J. W. Ochterski, R. L. Martin, K. Morokuma, V. G. Zakrzewski, G. A. Voth, P. Salvador, J. J. Dannenberg, S. Dapprich, A. D. Daniels, Ö. Farkas, J. B. Foresman, J. V. Ortiz, J. Cioslowski, D. J. Fox, Gaussian, Inc., Wallingford CT, 2009.
2. (a) V. V. Lemanov, L. S. Sochava, *Phys. Solid State*, **2003**, *45*, 1455.
(b) X. Wang, P. A. Beckman, C. W. Mallory, A. L. Rheingold, A. G. DiPasquale, P. J. Carroll, F. B. Mallory, *J. Org. Chem.*, **2011**, *76*, 5170.
(c) B. Rodríguez-Molina, S. Pérez-Estrada, M. A. Garcia-Garibay, *J. Am. Chem. Soc.*, **2013**, *135*, 10388.
(d) A. Kubica-Misztal, P. Rochowski, M. Florek-Wojciechowska, D. Kruk, *J. Chem. Phys.* **2017**, *146*, 164501.

Chapter 6: Conclusion and Future Scope

6.1. Conclusion

Stable organic radicals have been widely applied as spin center in the field of molecule-based magnetism. Their magnetic properties are attributed to the magnetic moment originated from unpaired electron and depend on the configuration of the intra- and intermolecular interaction between the magnetic moments. In the solid state, molecules are assembled by non-covalent intermolecular interaction and their property and function can be modified by the variation of molecular assembly. Therefore, it is important to develop the methodology to control the intra- and intermolecular magnetic interactions to construct the molecule-based magnet. In the present thesis, the author focused on the benzotriazinyl and pyrroline *N*-oxyl skeleton as spin center and their magneto-structural correlation and intramolecular interaction through non-conjugated framework were discussed.

In chapter 2, the magneto-structural correlation and the substituent effect on magnetic property for 3-*tert*-butyl benzotriazinyl derivatives carrying electron withdrawing group at 6- or 7-position were discussed by crystallographic, magnetic, spectroscopic, and computational studies. 7-Trifluoromethyl derivative **7CF3** formed ideal 1D ferromagnetic chain. Interestingly, 6-cyano derivative **6CN** exhibited magnetic phase transition caused by structure phase transition due to the rotation of molecules in solid state.

In chapters 3 and 4, hetero biradicals including pyrroline *N*-oxyl as basic skeleton were synthesized and their intramolecular magnetic interaction through non-conjugated framework was discussed. Their ground spin states of hetero biradicals were evaluated by ESR measurement, crystallographic analysis, magnetic measurement and computational study. Nitroxyl-triazinyl hetero biradicals **3PPO** and **3BPO** exhibited intramolecular antiferromagnetic interaction due to through-space SOMO-SOMO interaction. On the other hand, verdazyl and nitronyl nitroxide attached pyrroline *N*-oxyl hetero biradicals **POVZ** and **PONN** have ground triplet state derived from spin-spin interaction

due to the size of pyrroline ring.

In chapter 5, the electronic structure and intramolecular interaction of prepared hetero biradicals were evaluated by computational study. In addition, the molecular design of ground triplet state using the methodology established throughout the research was described.

In summary, systematic syntheses and evaluation of benzotriazinyl and hetero biradical derivatives revealed their interesting magnetic properties. In consequence, the practical design for construction of molecule-based magnets carrying non-conjugated framework was established.

6.2. Future Scope

The author investigated magnetic property of benzotriazinyl radicals and revealed 6-cyano substituted 3-*tert*-butyl benzotriazinyl derivative displays magnetic phase transition at ambient temperature without hysteresis. This result suggested that 6-cyano derivative can become the promising compound for developing thermal sensors and switching application. 3-*tert*-Butyl benzotriazinyl radicals can form columnar assembly, however, π - π interaction as driving force for construction of columnar structure is weak due to the steric effect of *tert*-butyl group. Therefore, structure phase transition can be observed in other analogues and it is required that evaluation of substituent effect on magneto-structural correlation in benzotriazinyl radicals.

In pyrroline *N*-oxyl based biradical system, its intramolecular interaction is dominant in the spin density distribution on vinylic moiety of pyrroline ring, which is derived from attached radical moiety. The novel mechanism of intramolecular magnetic interaction in pyrroline *N*-oxyl based biradicals can be available for the design guide for construction of high spin molecules. If pyrroline-based biradicals have self-assembly ability, the multidimensional magnetic network using triplet molecules can be constructed. To make molecule-based ferromagnet, at least 2D ferromagnetic interaction is required. In the point of view, proposed biradical skeleton is suitable for composition unit. In addition,

coordination ability of nitroxyl group makes strong intercolumnar interaction through metal (Figure 6-1), however, it is difficult to functionalize five-membered system and to modify their electronic structure. On the other hand, as shown in chapter 5, the computational study revealed strong magnetic intramolecular ferromagnetic interaction in azaphenylene *N*-oxyl biradical system. Therefore, it is important to evaluate their magneto-structural correlation based on experimental results. The computational study suggested that their intramolecular magnetic interaction is arising from through-bond interaction. It has naphthalene ring on the backside of nitroxyl group and functionalization of π -conjugation system can be available, indicating azaphenylene *N*-oxyl analogues are promising candidate for high spin molecules.

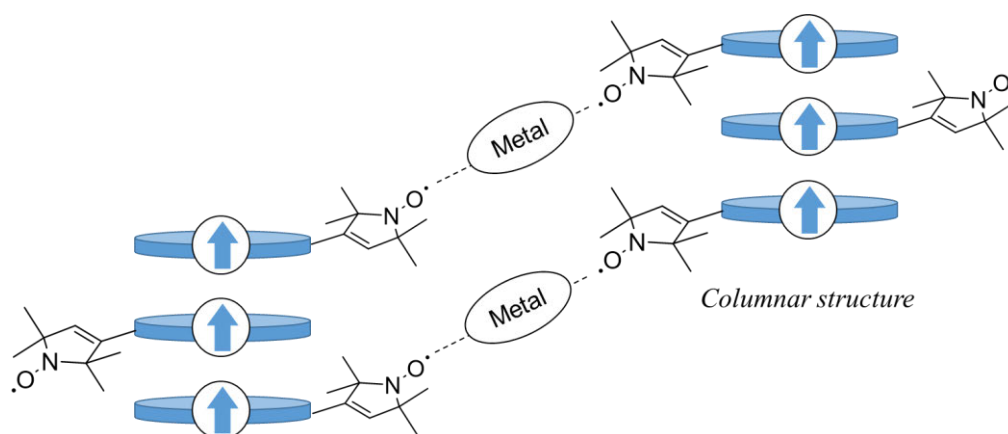


Figure 6-1. Schematic illustration for construction of molecule-based ferromagnet.

Chapter 7: Details of Synthetic Procedures

7.1. General Information

Acetonitrile and dichloromethane were distilled from calcium hydride. The chemicals were purchased from Wako, TCI Chemicals, Junsei Chemical and Sigma-Aldrich and used as received. The ^1H and ^{13}C NMR spectra were recorded by JEOL JNM-LA 300 and ECS-400 spectrometers using tetramethylsilane as internal reference. The chemical shifts and coupling constants were expressed in ppm and Hz, respectively. The mass spectroscopy was carried out using a Bruker Ultraflex II (MALDI-TOF, sinapic acid was used as the matrix) and JEOL GC-mate (EI). The IR spectra were recorded using a JASCO FT/IR-4100. The elemental analyses were carried out at the Central Laboratory of the Faculty of Science and Technology, Keio University. The crystal data were collected using a Bruker D8 Venture with $\text{MoK}\alpha$ (0.71073 Å) radiation. The structures were solved by the direct method or Intrinsic Phasing method using *SHELXT* and refined by F^2 full matrix least squares using *SHELXL* in the Bruker APEX-II and APEX-III program package. The magnetic susceptibility measurements were performed using a Quantum Design MPMP-XL SQUID magnetometer in the temperature range of 1.8-300 K. The diamagnetic contribution from the sample holder and samples estimated using the Pacault method were corrected. The X-band EPR spectra were recorded using a Bruker E500 spectrometer. The signal positions were calibrated with a Bruker ER035M teslameter. The samples were degassed by the freeze-pump-thaw method. DFT calculations were carried out by Gaussian program package. Unless otherwise noted, the SOMO and spin density distributions were shown in isovalues of 0.02 and 0.0004 for the SOMO and spin density, respectively.

7.2. Synthesis in Chapter 2

7.2.1. Synthesis of 3-*tert*-Butyl Benzotriazinyl Radicals Using C-N Coupling

(a) Synthesis of 3-*tert*-butyl-1,4-dihydro-1-phenyl-1,2,4-benzotriazin-4-yl (1)

The mixture of 2-iodoaniline (219 mg, 1.00 mmol), *N*'-phenyl-*N*-pivaloylhydrazine (250 mg, 1.30 mmol), K₂CO₃ (276 mg, 2.00 mmol) and CuI (19 mg, 0.100 mmol) in dry DMSO (2.5 mL) was heated at 90 °C for 24 h. The reaction mixture was diluted with EtOAc. The organic layer was washed with water and dried over Na₂SO₄ and the solvent was evaporated. The residue was dissolved in AcOH (16 mL) and heated to 100 °C for 10 min. The mixture was cooled to r.t., then aqueous 2 M NaOH was added to basify and extracted with CH₂Cl₂ (10mL). The organic layer was washed with aqueous 2 M NaOH, and then the organic layer was separated. To the CH₂Cl₂ solution was added aqueous 2 M NaOH (10 mL) and the mixture was stirred for 16 h. The organic layer was separated, washed with water, and dried over Na₂SO₄ and the solvent was evaporated. The residue was purified by column chromatography on neutral alumina (CH₂Cl₂/*n*-hexane = 1/6 as eluent) and recrystallized from *n*-hexane to give reddish-black crystals. Yield: 91 mg, 34%; LRMS(MALDI-TOF): $m/z = 264$ [M + H]⁺; mp: 106 – 108 °C; IR (KBr pellet, cm⁻¹): 2957, 2862, 1592, 1580; Elem. Anal.: calcd for C₁₇H₁₈N₃: C, 77.24; H, 6.86; N, 15.90. Found: C, 76.98; H, 6.82; N, 15.96.

(b) Synthesis of 3-*tert*-butyl-7-trifluoromethyl-1,4-dihydro-1-phenyl-1,2,4-benzotriazin-4-yl (7CF3)

The mixture of 2-iodo-4-trifluoromethylaniline (1.91 g, 6.65 mmol), *N*'-phenyl-*N*-pivaloylhydrazine (1.66 g, 8.65 mmol), K₂CO₃ (1.84 g, 13.3 mmol) and CuI (127 mg, 0.665 mmol) in dry DMSO (16 mL) was heated at 90 °C for 24 h. The reaction mixture was diluted with EtOAc. The organic layer was washed with water and dried over Na₂SO₄ and the solvent was evaporated. The residue was dissolved in AcOH (16mL) and heated to 100 °C for 10 min. The mixture was cooled to

r.t., then aqueous 2 M NaOH was added to make it basic and extracted with CH₂Cl₂ (60 mL). The organic layer was washed with aqueous 2M NaOH, and then the organic layer was separated. To the CH₂Cl₂ solution, aqueous 2 M NaOH (60 mL) was added, and the mixture was stirred for 16 h. The organic layer was separated, washed with water, and dried over Na₂SO₄ and the solvent was evaporated. The residue was purified by column chromatography on neutral alumina (CH₂Cl₂/ n-hexane = 1/6 as eluent) and recrystallized from CH₃OH to give reddish-black crystals. Yield: 584 mg, 26%; LRMS (MALDI- TOF): $m/z = 333 [M + H]^+$; mp: 86–88 °C; IR (KBr pellet, cm⁻¹): 2973, 2868, 1593, 1270; Elem. Anal. calcd for C₁₈H₁₇F₃N₃: C, 65.05; H, 5.16; F, 17.15; N, 12.64. Found: C, 65.04; H, 5.12; F, 17.1; N, 12.53

7.2.2. Synthesis of 3-*tert*-Butyl Benzotriazinyl Radicals Using Pd/C Catalyzed Cyclization Method

(a) Synthesis of *N*-phenylpivalohydrazonoyl chloride (4-*t*Bu)

To a solution of *N'*-phenyl-*N*-pivaloylhydrazine (231 mg, 1.20 mmol) and triphenylphosphine (393 mg, 1.25 mmol) in distilled CH₃CN (3.0 mL) was added carbon tetrachloride (0.096 mL, 1.25 mmol) under a nitrogen atmosphere and stirred for 16 h at room temperature. The solvent was evaporated under reduced pressure and the residue was purified by column chromatography on SiO₂ (CH₂Cl₂ / *n*-hexane = 2 / 3 as eluent) to give a clear oil which turns brown in air. Yield: 227 mg, 90%; ¹H NMR(CDCl₃, 300 MHz) δ : 7.62(s, 1H), 7.26(t, 2H, $J = 7.2$ Hz), 7.04(d, 2H, $J = 7.8$ Hz), 6.87(t, 1H, 7.8 Hz); ¹³C NMR(CDCl₃, 75 MHz) δ : 144.13, 135.71, 129.24, 120.41, 113.04, 40.93, 28.33; HRMS(EI): Calcd. for C₁₁H₁₅ClN₂[M]⁺: $m/z = 210.0924$, Found 210.0914.

(b) Synthesis of *N, N'*-diphenylpivalohydrazonamide (5a)

A mixture of *N*-phenylpivalohydrazonoyl chloride (277 mg, 1.31 mmol), aniline (0.120 mL, 1.31

mmol) and triethylamine (0.201 mL, 1.44 mmol) in EtOH(2.0 mL) was stirred for 16 h at room temperature under a nitrogen atmosphere. The reaction mixture was extracted with CH₂Cl₂, washed with water, dried over Na₂SO₄ and evaporated under reduced pressure. The residue was purified by column chromatography on SiO₂ (CH₂Cl₂ / *n*-hexane = 2 / 3 as eluent) to afford a white solid. Yield: 287 mg, 82%; mp: 76-78 °C; ¹H NMR(CDCl₃, 300 MHz) δ: 7.25-7.16(m, 4H), 6.96-6.94(m, 3H), 6.88(t, 1H, *J* = 7.2 Hz), 6.77(t, 1H, *J* = 7.2 Hz) 6.62(d, 2H, *J* = 7.8 Hz), 5.34(s, 1H), 1.26(s, 9H); ¹³C NMR(CDCl₃, 75 MHz) δ: 145.57, 143.14, 141.12, 129.20, 129.00, 120.33, 119.14, 115.67, 112.70, 37.90, 27.77; HRMS(EI): Calcd. for C₁₇H₂₁N₃[M]⁺: *m/z* = 267.1735, Found 267.1735; IR(KBr pellet, cm⁻¹): 3378, 3338, 3050, 2966, 1598.

(c) Synthesis of 3-*tert*-butyl-1,4-dihydro-1-phenyl-1,2,4-benzotriazin-4-yl (1)

To a solution of *N,N'*-diphenylpivalohydrazonamide (325 mg, 1.22 mmol) and catalytic amount of 10% Pd/C in CH₂Cl₂(4.5 mL) was added DBU (0.182 mL, 1.22 mmol) and stirred for 16 h at room temperature. The reaction mixture was concentrated and the residue was purified by column chromatography on neutral alumina (CH₂Cl₂ / *n*-hexane = 1 / 3 as eluent) and recrystallized from *n*-hexane to afford a reddish-black crystal. Yield: 280 mg, 87%; mp: 107-109 °C, identical to an authentic sample described in chapter 7.2.1.(a).

(d) Synthesis of *N*-(4-cyanophenyl)-*N'*-phenylpivalohydrazonamide (5b)

A mixture of *N*-phenylpivalohydrazonoyl chloride (297 mg, 1.41 mmol), 4-aminobenzonitrile (167 mg, 1.41 mmol) and triethylamine (0.216 mL, 1.55 mmol) in EtOH (2.0 mL) was stirred for 1 d at room temperature under a nitrogen atmosphere. The reaction mixture was extracted with CH₂Cl₂, washed with water, dried over Na₂SO₄ and evaporated under reduced pressure. The residue was purified by column chromatography on SiO₂ (CH₂Cl₂ / *n*-hexane = 2 / 1 as eluent) to afford an orange

solid. Yield: 158 mg, 38%; mp: 54-57 °C; ¹H NMR(CDCl₃, 300 MHz) δ: 7.50(d, 2H, *J* = 8.7 Hz), 7.22(t, 2H, *J* = 7.8 Hz) 6.97(d, 2H, *J* = 7.8 Hz), 6.93(s, 1H), 6.83(t, 1H, *J* = 7.5 Hz), 6.61(d, 2H, *J* = 8.7 Hz), 1.25(s, 9H); ¹³C NMR(CDCl₃, 75 MHz) δ: 145.22, 145.00, 141.31, 133.67, 129.16, 120.00, 119.47, 115.25, 112.95, 102.67, 38.11, 27.67; HRMS(EI): Calcd. for C₁₈H₂₀N₄[M]⁺: *m/z* = 292.1688, Found 292.1686; IR(KBr pellet, cm⁻¹): 3330, 2966, 2363, 2219, 1601.

(e) Synthesis of 3-*tert*-butyl-7-cyano-1,4-dihydro-1-phenyl-1,2,4-benzotriazin-4-yl (7CN)

To a solution of *N*-(4-cyanophenyl)-*N'*-phenylpivalohydrazonamide (90 mg, 0.308 mmol) and catalytic amount of 10% Pd/C in CH₂Cl₂(2.0 mL) was added DBU (0.046 mL, 0.308 mmol) and stirred for 16 h at room temperature. The reaction mixture was concentrated and the residue was purified by column chromatography on neutral alumina (CH₂Cl₂ / *n*-hexane = 1 / 3 as eluent) and recrystallized from CH₂Cl₂ / *n*-hexane to afford a greenish-black crystal. Yield: 69 mg, 78%; mp: 117-119 °C; LRMS(MALDI): Calcd. for C₁₈H₁₇N₄[M]⁺: *m/z* = 289.2, Found: 289; IR(KBr pellet, cm⁻¹): 2956, 2222, 1581; Elem. Anal.: Calcd. for C₁₈H₁₇N₄: C 74.72, H 5.92, N 19.36, Found: C 74.87, H 5.95, N 18.98.

(f) Synthesis of *N*-(3-cyanophenyl)-*N'*-phenylpivalohydrazonamide (5c)

A mixture of *N*-phenylpivalohydrazonoyl chloride (526 mg, 2.50 mmol), 3-aminobenzonitrile (296 mg, 2.51 mmol) and triethylamine (0.383 mL, 2.75 mmol) in EtOH (2.5 mL) was stirred for 1 d at room temperature under a nitrogen atmosphere. The reaction mixture was extracted with CH₂Cl₂, washed with water, dried over Na₂SO₄ and evaporated under reduced pressure. The residue was purified by column chromatography on SiO₂ (EtOAc / *n*-hexane = 1 / 4 as eluent) to afford a yellow solid which turn orange oil in air. Yield: 446 mg, 61%; ¹H NMR(CDCl₃, 300 MHz) δ: 7.30(t, 1H, *J* = 7.8 Hz), 7.24-7.14(m, 3H), 6.97(d, 2H, *J* = 8.1 Hz), 6.90(m, 2H), 6.83(t, 1H, *J* = 7.3 Hz), 6.75(dd, 1H, *J* = 8.1 Hz, 2.7 Hz), 5.49(s, 1H), 1.26(s, 9H); ¹³C NMR(CDCl₃, 75 MHz) δ: 145.27, 142.18, 141.84,

130.050, 129.09, 123.69, 119.84, 119.64, 118.87, 118.36, 113.01, 112.93, 38.00, 27.66; HRMS(EI): Calcd. for $C_{18}H_{20}N_4[M]^+$: $m/z = 292.1688$, Found 292.1672; IR (KBr pellet, cm^{-1}): 3350, 2965, 2229, 1600.

(g) Synthesis of 3-*tert*-butyl-6-cyano-1,4-dihydro-1-phenyl-1,2,4-benzotriazin-4-yl (6CN)

To a solution of *N*-(4-cyanophenyl)-*N'*-phenylpivalohydrazonamide (393 mg, 1.34 mmol) and catalytic amount of 10% Pd/C in CH_2Cl_2 (5.0 mL) was added DBU (0.250 mL, 1.37 mmol) and stirred for 23 h at room temperature. The reaction mixture was concentrated and the residue was purified by column chromatography on SiO_2 (EtOAc / *n*-hexane = 1 / 10 as eluent) and recrystallized from CH_2Cl_2 / *n*-hexane to afford a black crystal. Yield: 57 mg, 15%; mp: 180-181 °C; LRMS(MALDI): Calcd. for $C_{18}H_{17}N_4[M]^+$: $m/z = 289.2$, Found: 289; IR (KBr pellet, cm^{-1}): 2958, 2217, 1590; Elem. Anal.: Calcd. for $C_{18}H_{17}N_4$: C 74.72, H 5.92, N 19.36, Found: C 74.65, H 5.89, N 19.05.

7.3. Synthesis in Chapter 3

7.3.1. Synthesis of *N'*-phenyl-*N*-(1,1,3,3-tetramethyl-2-oxo-isoindolin-5-yl)benzenecarbohydrazonamide (9-Ph)

To a solution of 5-amino-1,1,3,3-tetramethylisoindolin-2-ylloxyl (205 mg, 1.00 mmol) and *N*-phenyl-benzenecarbohydrazonoyl chloride (254 mg, 1.10 mmol) in EtOH(3.0 mL) was added triethylamine (0.139 mL, 1.00 mmol) under a nitrogen atmosphere and stirred for 16 h at room temperature. The reaction mixture was extracted with CH_2Cl_2 , washed with water, dried over Na_2SO_4 and evaporated under reduced pressure. The residue was purified by column chromatography on SiO_2 (EtOAc / *n*-hexane = 1 / 3 as eluent) to give a yellow solid. Yield: 282 mg, 71%; mp: 154-156 °C; HRMS(EI): Calcd. for $C_{25}H_{27}N_4O[M]^+$: $m/z = 399.2185$, Found 399.2193; IR(KBr pellet, cm^{-1}): 3321, 3052, 2975, 2927, 1601.

7.3.2. Synthesis of 1,3-diphenyl-1,4,6,8-tetrahydro-6,6,8,8-tetramethyl-pyrrolo[4,5-g]-1,2,4-benzotriazin-4-yl-7-oxyl (3PPO)

To a solution of *N*'-phenyl-*N*-(1,1,3,3-tetramethyl-2-oxo-isoindolin-5-yl)benzenecarbohydrazonamide (282 mg, 0.706 mmol) and catalytic amount of 10% Pd/C in CH₂Cl₂ (12.0 mL) was added DBU (0.105 mL, 0.706 mmol) and stirred for 16 h at room temperature. The reaction mixture was concentrated and the residue was purified by column chromatography on SiO₂ (EtOAc / *n*-hexane = 1 / 3 as eluent) to give a brown solid. Recrystallization from CH₂Cl₂ / *n*-hexane gave a black crystal. Yield: 174 mg, 62%; mp: 210-211 °C; LRMS(MALDI): Calcd. for C₂₅H₂₄N₄O[M]⁺: *m/z* = 396.2, Found: 396; IR(KBr pellet, cm⁻¹): 3070, 2968, 2926, 1592; Elem. Anal.: Calcd. for C₂₅H₂₄N₄O: C 75.73, H 6.10, N 14.13, Found: C 75.71, H 6.14, N 13.79.

7.3.3. Synthesis of *N*'-phenyl-*N*-(1,1,3,3-tetramethyl-2-oxo-isoindolin-5-yl)pivalohydrazonamide (9-*t*Bu)

To a solution of 5-amino-1,1,3,3-tetramethylisoindolin-2-yloxyl (146 mg, 0.711 mmol) and *N*-phenylpivalohydrazonoyl chloride (171 mg, 0.812 mmol) in EtOH (3.0 mL) was added triethylamine (0.099 mL, 0.771 mmol) under a nitrogen atmosphere and stirred for 16 h at room temperature. The reaction mixture was extracted with CH₂Cl₂, washed with water, dried over Na₂SO₄ and evaporated under reduced pressure. The residue was purified by column chromatography on SiO₂ (EtOAc / *n*-hexane = 1 / 4 as eluent) to give a yellow solid. Yield: 178 mg, 66%; mp: 71-73 °C; HRMS(EI): Calcd. for C₂₃H₃₁N₄O[M]⁺: *m/z* = 379.2498, Found 379.2523; IR(KBr pellet, cm⁻¹): 3348, 3050, 2973, 2928, 2868, 1602.

7.3.4. Synthesis of 3-*tert*-butyl-1-phenyl-1,4,6,8-tetrahydro-6,6,8,8-tetramethyl-pyrrolo[4,5-g]-1,2,4-benzotriazin-4-yl-7-oxyl (3BPO)

To a solution of *N*'-phenyl-*N*-(1,1,3,3-tetramethyl-2-oxo-isoindolin-5-yl)pivalohydrazoneamide (198 mg, 0.522 mmol) and catalytic amount of 10% Pd/C in CH₂Cl₂(5.0 mL) was added DBU (0.079 mL, 0.706 mmol) and stirred for 16 h at room temperature. The reaction mixture was concentrated and the residue was purified by column chromatography on SiO₂ (EtOAc / *n*-hexane = 1 / 5 as eluent) to give a reddish-brown solid. Recrystallization from CH₂Cl₂ / *n*-hexane gave a reddish-black crystal. Yield: 107 mg, 54%; mp: 168-170 °C; LRMS(MALDI): Calcd. for C₂₃H₂₈N₄O[M]⁺: *m/z* = 376.2, Found: 376; IR(KBr pellet, cm⁻¹): 2974, 2954, 2926, 1592; Elem. Anal.: Calcd. for C₂₃H₂₈N₄O: C 73.37, H 7.50, N 14.88, Found: C 73.49, H 7.57, N 14.49.

7.4. Synthesis in Chapter 4

7.4.1. Synthesis of 1,5-diisopropyl-3-(2,5-dihydro-2,2,5,5-tetramethyl-1*H*-pyrrol-3-yl)-1,2,4,5-tetrazane 6-oxide (14)

To a solution of 2,2-5,5-tetramethyl-3-pyrroline-3-carboxaldehyde (215 mg, 1.40 mmol) and NaOAc (230 mg, 2.80 mmol, 2.0 eq) in EtOH (3.0 mL) was added 2,4-diisopropylcarbohydrazide bishydrochloride (346 mg, 1.40 mmol, 1.0 eq) and stirred at room temperature overnight. After addition of EtOAc, organic layer was washed with aqueous Na₂CO₃ and dried over Na₂SO₄, then the solvent was evaporated. To the residue was added *n*-hexane and white precipitate was collected. Yield: 155 mg, 36%; ¹H NMR(CDCl₃, 400 MHz) δ: 5.67 (s, 1H), 4.66 (septet, *J* = 6.4 Hz, 2H), 3.86 (t, *J* = 12.4 Hz, 1H) 3.54 (d, *J* = 12.4 Hz, 2H), 1.37 (s, 6H), 1.27 (s, 6H), 1.11 (d, *J* = 6.4 Hz, 6H), 1.08 (d, *J* = 6.4 Hz, 6H); ¹³C NMR(CDCl₃, 100 MHz) δ: 153.3, 142.3, 133.8, 66.8, 66.6, 63.3, 47.3, 30.4, 29.9, 19.2, 18.1; LRMS(MALDI-TOF): Calcd. for C₁₆H₃₂N₅O[M+H]⁺: *m/z* = 310.3, Found 310; IR (KBr pellet, cm⁻¹): 3257, 2966, 2925, 2870, 1610; Elem. Anal.: Calcd for C₁₆H₃₁N₅O: C 62.10, H 10.10, N 22.63, Found: C 61.74, H 10.07, N 22.41.

7.4.2. Synthesis of 1,5-diisopropyl-3- (2,5-dihydro-2,2,5,5-tetramethyl-1H-pyrrol-3-yl)-6-oxoverdazyl (15)

To a solution of 1,5-diisopropyl-3- (2,5-dihydro-2,2,5,5-tetramethyl-1H-pyrrol-3-yl)-1,2,4,5-tetrazane 6-oxide (117 mg, 0.378 mmol) in toluene (3.0 mL) was added DDQ (86 mg, 0.378 mmol, 1.0 eq) and stirred at room temperature for 1h. After addition of water and EtOAc, organic layer was washed with aqueous Na₂CO₃ and dried over Na₂SO₄, then the solvent was evaporated. The residue was purified using column chromatography on SiO₂ (EtOAc as eluent) to afford reddish orange crystalline solid. Yield: 84 mg, 72%; mp: 105-107 °C; LRMS(MALDI): Calcd. for C₁₅H₂₉N₅O[M+H]⁺: *m/z* = 307.2, Found: 307; IR(KBr pellet, cm⁻¹): 2968, 2927, 2870, 1680; Elem. Anal.: Calcd. for C₁₆H₂₈N₅O: C 62.71, H 9.21, N 22.85, Found: C 62.69, H 9.20, N 22.73.

7.4.3. Synthesis of 1,5-diisopropyl-3- (1-oxyl-2,5-dihydro-2,2,5,5-tetramethyl-1H-pyrrol-3-yl)-6-oxoverdazyl (POVZ)

To a solution of 1,5-diisopropyl-3- (2,5-dihydro-2,2,5,5-tetramethyl-1H-pyrrol-3-yl)-6-oxoverdazyl (50 mg, 0.163 mmol) in CH₂Cl₂ (5.0 mL) was added a solution of CH₂Cl₂ (*ca.* 1 mL) of *m*-CPBA (44 mg, 0.179 mmol 1.1 eq) at 0 °C and stirred for 1 h then allowed to warm to room temperature and stirring was continued for 1 h. After addition of aqueous Na₂CO₃, organic layer was washed with water and dried over Na₂SO₄, then the solvent was evaporated. The residue was purified using column chromatography (SiO₂, EtOAc/*n*-hexane = 1/3) to afford orange solid. Slow evaporation from the mixed solvent of CH₂Cl₂/MeOH gave orange crystal. Yield: 84 mg, 72%; mp: 163 °C (decomp.); LRMS(MALDI): Calcd. for C₁₆H₂₇N₅O₂[M]⁺: *m/z* = 321.2, Found: 321; IR (KBr pellet, cm⁻¹): 2979, 2933, 2873, 1680; Elem. Anal.: Calcd. for C₁₅H₂₇N₅O₂: C 59.79, H 8.47, N 21.79, Found: C 59.80, H 8.47, N 21.80.

7.4.4. Synthesis of 2-(1-oxyl-2,5-dihydro-2,2,5,5-tetramethyl-1*H*-pyrrol-3-yl)-4,4,5,5-tetramethyl-4,5-dihydro-1*H*-imidazol-1-yloxy 3-oxide (PONN)

To a solution of 4,4,5,5-tetramethyl-2-(2,5-dihydro-2,2,5,5-tetramethyl-1*H*-pyrrol-3-yl)-4,5-dihydro-1*H*-imidazol-1-yloxy 3-oxide (129 mg, 0.460 mmol) in CH₂Cl₂ (5.0 mL) was added a solution of *m*-CPBA (147 mg, 0.598 mmol) in CH₂Cl₂ (2.0 mL) at 0 °C and stirred for 4 h at room temperature. The resulting mixture was neutralized with aqueous Na₂CO₃ then the organic layer was separated. The aqueous layer was extracted with CH₂Cl₂ and organic layer was dried over Na₂SO₄. The residue was purified using column chromatography on neutral alumina (CH₂Cl₂/*n*-hexane = 2/1 as eleuent) to afford blue solid and recrystallization from MeOH to give greenish-black crystal. Yield: 43 mg, 54%; mp: 170-171 °C; LRMS(MALDI): Calcd. for C₁₅H₂₈N₃O[M-2O+3H]⁺: *m/z* = 266.2, Found: 266; IR(KBr pellet, cm⁻¹): 2978, 2931, 2871; Elem. Anal.: Calcd. for C₁₅H₂₃N₃O₃: C 60.99, H 8.53, N, 14.23, found C 61.15, H 8.55, N 14.27.

Publication List

1. Articles Related to Thesis

- (1) Yusuke Takahashi, Youhei Miura, Naoki Yoshioka, "Introduction of Three Aryl Groups to Benzotriazinyl Radical by Suzuki-Miyaura Cross-coupling Reaction", *Chemistry Letters*, **2014**, *43*, 1236-1238.
- (2) Yusuke Takahashi, Youhei Miura, Naoki Yoshioka, "Synthesis and properties of the 3-*tert*-butyl-7-trifluoromethyl-1,4-dihydro-1-phenyl-1,2,4-benzotriazin-4-yl radical", *New Journal of Chemistry*, **2015**, *39*, 4783-4789.
- (3) Yusuke Takahashi, Youhei Miura, Naoki Yoshioka, "Magnetic Interaction Observed in Hetero Biradical Derivatives Containing a 2,2,5,5-Tetramethylpyrrolin-1-yloxy Unit as a Localized Spin Center", *ChemPhysChem*, **2018**, *19*, 175-179.

2. Presentations at International Conference

- (1) Yusuke Takahashi, Youhei Miura, Naoki Yoshioka, "Modification and Properties of Benzotriazinyl Radicals by Suzuki-Miyaura Cross-Coupling Reaction", 14th International Conference on Molecule-Based Magnets (ICMM2014), Saint Petersburg, Russia, July 2014.
- (2) Yusuke Takahashi, Youhei Miura, Naoki Yoshioka, "Crystal Structure and Properties of Aryl-Substituted Benzotriazinyl Radical Derivatives", 11th International Workshop on Crystal Growth of Organic Materials (CGOM11), Nara, Japan, June 2014.
- (3) Yusuke Takahashi, Youhei Miura, Naoki Yoshioka, "Magneto-Structural Correlation of 3-*tert*-Butyl Benzotriazinyl Radical Derivatives", The 22nd International Conference on the Chemistry of the Organic Solid State (ICCOSS XXII), Niigata, Japan, July 2015.
- (4) Yusuke Takahashi, Youhei Miura, Naoki Yoshioka, "Crystal Structures of Benzotriazinyl Radicals and Their Physicochemical Properties", The 9th Japanese-Russian Workshop on Open Shell

Compounds and Molecular Spin Devices, Awajishima, Japan, November 2015.

- (5) Yusuke Takahashi, Youhei Miura, Naoki Yoshioka, “Synthesis of Chemically-Modified 3-*tert*-Butyl Benzotriazinyl Radicals and Their Magneto-Structural Correlation”, The 2015 International Chemical Congress of Pacific Basin Societies (Pacifichem), Honolulu, U.S.A., December 2015.
- (6) Yusuke Takahashi, Youhei Miura, Naoki Yoshioka, “Synthesis and Properties of Benzotriazinyl-Nitroxyl Hetero Biradical”, The 15th International Conference on Molecule-Based Magnets (ICMM2016), Sendai, Japan, September 2016.
- (7) Yusuke Takahashi, Youhei Miura, Naoki Yoshioka, “Evaluation of Magnetic Exchange Interaction through Non-Conjugated System: Molecular Design of Organic Biradicals Having Ground Triplet State”, The 4th International Conference on Computation for Science and Technology (ICCST 2016), Langkawi, Malaysia, November 2016.
- (8) Yusuke Takahashi, Yusuke Narumi, Ryo Matsuhashi, Youhei Miura, Naoki Yoshioka, “Synthesis of Hetero Diradical Derivatives Containing a Pyrroline Nitroxide Unit and Their Magnetic Interaction”, The 8th Conference on Nitroxide Radicals (SPIN-2017), Padova, Italy, September 2017.

Acknowledgement

The present thesis is the collection of the scientific research results which have been studied under the supervision of Prof. Dr. Naoki Yoshioka at Yoshioka laboratory, Keio University during 2015-2018.

The author would like to express his gratitude to Prof. Dr. Naoki Yoshioka for his invaluable discussion, suggestion and continuous encouragement through the scientific work. Thanks to him, I have spent fruitful research life at the laboratory and have studied continuously since undergraduate course.

The author wishes to show his appreciation to Prof. Dr. Satoshi Yabushita, Prof. Dr. Hiroshi Kondoh and Assoc. Prof. Dr. Yuya Oaki for their suggestion and constructive discussion to revise the manuscript.

The author appreciates to Assistant Prof. Dr. Youhei Miura for beneficial comments and thanks to Dr. Kenji Yoza (Bruker Japan) for the discussion about crystallographic analysis.

The author thanks to the collaborators, Dr. Ryota Suzuki, Mr. Naoya Tsuchiya, Mr. Yusuke Narumi, Mr. Yuki Shimizu, Mr. Ryo Matsuhashi, Mr. Ryo Tsuchiya, Mr. Rei Ito, Mr. Yutaro Suzuki and group members of Yoshioka laboratory for useful discussion and helpful comments.

This work was partly supported by the Research Associate (fixed term/research incentive) System of the graduate school of Keio University and the JSPS Grant-in-Aid for JSPS Research Fellow.

At last but not least, the author expresses the deepest his gratitude for his parents, Mr. Kazuaki Takahashi and Mrs. Eiko Takahashi.

February 2018

Yusuke Takahashi